Cardiac macrophages are critical for myocardial function and contractility in human heart failure

DISSERTATION ZUR ERLANGUNG DES DOKTORGRADES DER NATURWISSENSCHAFTEN (DR. RER. NAT.)

DER FAKULTÄT FÜR BIOLOGIE UND VORKLINISCHE MEDIZIN DER UNIVERSITÄT REGENSBURG

vorgelegt von

Laura Stengel

aus

Lörrach

im Jahr

2025

Cardiac macrophages are critical for myocardial function and contractility in human heart failure

DISSERTATION ZUR ERLANGUNG DES DOKTORGRADES DER NATURWISSENSCHAFTEN (DR. RER. NAT.)

DER FAKULTÄT FÜR BIOLOGIE UND VORKLINISCHE MEDIZIN DER UNIVERSITÄT REGENSBURG

vorgelegt von

Laura Stengel

aus

Lörrach

im Jahr

2025

Das Promotionsgesuch wurde eingereicht am:

04.12.25

Betreuung durch:

Prof. Dr. med. Lars Maier

Prof. Dr. rer. nat. Kathrin Renner

Unterschrift:

Table of contents

List of Abbreviations

%	Percent
°C	Degree Celsius
× g	Relative centrifugal force
µg	Microgram
µl	Microliter
µM	Micromolar
ADP	Adenosine diphosphate
AF	Atrial fibrillation
ARNi	Angiotensin receptor-neprilysin inhibitors
ATP	Adenosine triphosphate
AV	Atrioventricular
bpm	Beats per minute
Ca^{2+}	Calcium
CaMKII	Calcium/calmodulin-dependent kinase II
CCR2	C Motif Chemokine Receptor 2
Cfs1R	Colony stimulating factor 1 Receptor
DAMP	Danger-associated molecular patterns
DCM	Dilated cardiomyopathy
EC	Excitation-contraction
EF	Ejection fraction
ETS	Electron transfer system
FFR	Force-frequency-relationship
FOV	Field of view
g	Gram
HF	Heart failure
HFrEF	Heart failure with reduced ejection fraction
HFpEF	heart failure with preserved ejection fraction
H_2O_2	Hydrogen peroxide
ICM	Ischemic cardiomyopathy
IPTO	Individualized patient tumor organoid
iPSC-CM	Induced pluripotent stem cell cardiomyocytes

K^+	Potassium
LTCC	L-type calcium channel
LV	Left ventricle
LVSD	Left ventricular systolic dysfunction
mg	Milligram
ml	Milliliter
MDa	Megadalton
mM	Millimolar
MRA	Mineralocorticoid receptor antagonists
Na^{2+}	Sodium
ng	Nanogram
nM	Nanomolar
NCX	Na^+/Ca^{2+} exchanger
OXPHOS	Oxidative phosphorylation
Pen/Strep	Penicillin/streptomycin
pH	Potentia hydrogenii
PP1/2	Protein phosphatase 1/2
PRP	Post-rest-potentiation
rpm	Revolutions per minute
PKA	Protein kinase A
ROS	Reactive oxygen species
ROX	Residual oxygen consumption
RT	Relaxation time
RyR2	Ryanodine receptor type 2
SAN	Sinoatrial node
SERCA	Sarco/endoplasmic reticulum Ca^{2+}-ATPase
SR	Sarcoplasmatic reticulum
V	Volt
TTP	Time to peak

List of figures

List of tables

Abstract

Heart failure (HF) remains a major global health burden despite available therapies, underscoring the need for novel treatment approaches. Cardiac macrophages play a critical role in maintaining myocardial homeostasis and they are increasingly recognized as promising targets for cardiac immunotherapy. This thesis investigated the causal role of cardiac macrophages in living, long-term cultured human heart tissue obtained from patients with heart failure with reduced ejection fraction (HFrEF).

Left ventricular (LV) myocardium samples were collected from 12 patients with end-stage HFrEF undergoing heart transplantation with a mean left ventricular ejection fraction of 20.8 ± 1.8%. Long-term cultured human LV tissue slices were treated with a colony-stimulating factor 1 receptor inhibitor (Csf1Ri) to deplete macrophages. Depletion was confirmed by CD68 immunohistochemistry.

Macrophage depletion led to a significant decline in contractility of human HFrEF myocardium displayed by a 35.04 ± 6.94% reduction in systolic force amplitude after 10 days of Csf1Ri treatment. Functional analyses of excitation–contraction coupling using post-rest potentiation suggested impaired sarcoplasmic reticulum (SR) calcium (Ca^{2+}) handling in macrophage-depleted HFrEF tissue. Ca^{2+} imaging using epifluorescence microscopy in isolated cardiomyocytes from human HFrEF tissue slices showed decreased Ca^{2+} transient amplitudes in Csf1Ri treated tissue, while caffeine measurements confirmed impaired SR Ca^{2+} handling. Mechanistic studies further indicated that macrophage depletion increased oxidative stress and cardiomyocyte apoptosis. High-resolution respirometry demonstrated that macrophage depletion in human HFrEF myocardium caused an impaired mitochondrial respiration across all respiratory chain complexes. Transmission electron microscopy revealed a greater proportion of structurally damaged mitochondria and compromised mitochondrial integrity in macrophage-depleted human HFrEF tissue slices.

In summary, macrophage depletion in human HFrEF myocardium results in a significant loss of contractile force, likely driven by altered Ca^{2+} homeostasis, enhanced cardiomyocyte apoptosis and mitochondrial dysfunction. These findings provide direct

functional evidence that cardiac macrophages are crucial regulators of myocardial performance in human HF.

Zusammenfassung

Die Herzinsuffizienz (HI) stellt trotz verfügbarer Therapien nach wie vor eine große globale Gesundheitsbelastung dar, was die Notwendigkeit neuer Behandlungsansätze unterstreicht. Kardiale Makrophagen spielen eine entscheidende Rolle bei der Aufrechterhaltung der myokardialen Homöostase und werden zunehmend als vielversprechende Ziele für die kardiale Immuntherapie anerkannt. In dieser Arbeit wurde die kausale Rolle von Herzmakrophagen in lebendigem, langzeitkultiviertem menschlichem Herzgewebe untersucht, das von Patienten mit Herzinsuffizienz mit reduzierter Ejektionsfraktion (HFrEF) gewonnen wurde.

Linksventrikuläre (LV) Myokardproben wurden von 12 Patienten mit Herzinsuffizienz mit reduzierter Ejektionsfraktion (HFrEF) im Endstadium entnommen, die sich einer Herztransplantation unterzogen und eine mittlere linksventrikuläre Ejektionsfraktion von 20,8 ± 1,8% aufwiesen. Langzeitkultivierte menschliche LV-Gewebeschnitte wurden mit einem Kolonie-stimulierenden Faktor-1-Rezeptor-Inhibitor (Csf1Ri) behandelt, um Makrophagen zu entfernen. Die Depletion wurde anschließend durch CD68-Immunhistochemie bestätigt.

Die Makrophagen-Depletion führte zu einer starken Reduktion der Kontraktilität im HFrEF Gewebe, die sich in einer Verringerung der systolischen Kraftamplitude um 35,04 ± 6,94 % nach 10 Tagen Csf1Ri-Behandlung zeigte. Funktionsanalysen der Elektromechanischen Kopplung unter Verwendung der Post-Rest-Potenzierung deuteten auf eine beeinträchtigte Ca^{2+}-Verarbeitung des sarkoplasmatischen Retikulum (SR) in Makrophagen-depletiertem Gewebe hin. Ca^{2+}-Bildgebung unter Verwendung von Epifluoreszenzmikroskopie in isolierten Kardiomyozyten aus menschlichen HFrEF Gewebeschnitten zeigte verringerte Ca^{2+}-Transientenamplituden in Csf1Ri-behandeltem Gewebe, während Koffeinmessungen eine beeinträchtigte SR-Ca^{2+}-Verarbeitung bestätigten. Mechanistische Studien zeigten zudem, dass eine Makrophagen-Depletion den oxidativen Stress und die Apoptose der Kardiomyozyten erhöhte. Hochauflösende Respirometrie zeigte, dass die Makrophagenverarmung im

menschlichen HFrEF-Myokard eine beeinträchtigte mitochondriale Atmung über alle Atmungskettenkomplexe hinweg verursachte. Transmissionselektronenmikroskopie offenbarte einen höheren Anteil strukturell geschädigter Mitochondrien und eine beeinträchtigte mitochondriale Integrität in Makrophagen-depletiertem menschlichen HFrEF Gewebeschnitten.

Zusammenfassend lässt sich sagen, dass die Makrophagen-Depletion im menschlichen HFrEF-Myokard zu einem signifikanten Verlust der Kontraktionskraft führt, der wahrscheinlich durch eine veränderte Ca^{2+}-homöostase, eine verstärkte Apoptose der Kardiomyozyten und eine mitochondriale Dysfunktion verursacht wird. Diese Ergebnisse liefern einen direkten funktionellen Beweis dafür, dass kardiale Makrophagen entscheidende Regulatoren der Myokardleistung bei menschlicher HI sind.

1 Introduction

1.1 The human myocardium

1.1.1 Myocardial structure and function

The myocardium, the muscular tissue of the heart, is placed between the endocardium (inner layer of the heart) and the epicardium (outer layer of the heart). Oxygen and nutrients essential for the maintenance of the myocardium are delivered through the coronary arteries located on the epicardial surface of the heart. The myocardial tissue is composed of several layers of contractile muscle cells known as cardiomyocytes, which represent a special form of the striated muscle. Unlike skeletal muscle cells, which typically have multiple peripheral nuclei, cardiomyocytes are generally found centrally with one or occasionally more cell nuclei [1]. Cardiomyocytes are interconnected in a network-like manner, forming a functional syncytium. Cells are thereby structurally connected to each other by intercalated discs (disci intercalares) containing gap junctions. These junctions enable electrical coupling, allowing depolarization waves to pass from cell to cell, leading to coordinated, uniform contractions [2]. In addition to gap junctions, intercalated discs also contain adhesion contacts and desmosomes, which provide additional stability to the cell structure and facilitate mechanical force transmission between cells [3]. Depending on its strain, the myocardium is thinner in the area of the left and right atrium than in the ventricles, while the left ventricle is stronger than the right ventricle [4].

The cell membrane of cardiomyocytes, known as the sarcolemma, features an extensive network of highly branched invaginated structures called transverse tubules (T-tubules), which run perpendicular to the muscle fiber axis. These T-tubules are rich in ion channels that are crucial for key cellular processes such as excitation-contraction (EC) coupling, action potential initiation and signal transduction [5]. By extending deep into the interior of the cell, T-tubulues come into close contact with the terminal cisternae of the sarcoplasmatic reticulum (SR), forming specialized structures known as diads. Located at the level of the intercalated discs, these diads play a central role in EC coupling by positioning voltage-gated L-type calcium channels (LTCCs) in close

proximity to the junctional membrane of the SR, thereby juxtaposing an inlet for the action potential near a source of calcium (Ca^{2+}) ions [6].

The SR is a membrane-bound organelle structurally similar to the smooth endoplasmatic reticulum in other cell types. In cardiomyocytes, it forms a segmented network of tubules around the myofibrils. The primary function of the SR is the storage and regulated cycling of Ca^{2+} ions, which are predominantly bound to calsequestrin, a specialized Ca^{2+}-binding protein that greatly enhances the storage capacity of the SR [7]. During EC coupling in the heart, the SR serves as the main source of cytosolic Ca^{2+} increase. Released Ca^{2+} ions then bind to troponin C, initiating the contraction of muscle fibers. Myofibrils, the structural and functional unit of the striated muscle, are composed of repeating sarcomeres built from the myofilaments actin and myosin. During contraction, these filaments slide past one another, leading to the shortening of sarcomeres and thus the entire myofibril, producing mechanical force [8].

1.1.2 Cardiac excitation-contraction coupling

For cardiac muscle contraction an electric excitation is converted into a mechanical contraction. As mentioned above, this process is described as EC coupling. This process starts with a cardiac action potential that increases the membrane potential of cardiomyocytes. In the heart, this electrical activation originates from pacemaker cells located in the sinoatrial node, which generate spontaneous depolarizations and thus function autonomously. The electrical impulses are forwarded over the atrioventricular (AV) node to the His bundle, which divides into left and right bundle branches ultimately reaching the Purkinje fibers, which ensure a rapid and coordinated ventricular activation [9].

Depolarization causes the membrane potential to rise from its resting potential, typically between -60 and -80 mV, toward more positive values. This leads to the opening of voltage-gated sodium (Na^+) channels, causing a rapid influx of Na^+ ions that drives the membrane potential quickly towards the Na^+ equilibrium potential of approximately +70 mV. The cardiac action potential thereby follows the all-or-none principle, meaning that the initial stimulus needs to reach a threshold to activate rapid Na^+ channels and trigger the action potential. Following this initial depolarization, a

brief efflux of potassium (K^+) causes a small repolarization which subsequently opens voltage-gated LTCC, allowing Ca^{2+} ions to enter the cell. At this stage, the inward flow of Ca^{2+} is balanced by outward K^+ currents, forming a characteristic plateau phase during which the membrane potential remains relatively stable. As the activity of delayed rectifier K^+ channels (both slow and rapid types) increases, repolarization begins, and the membrane potential gradually returns to its resting state (Figure 1) [8].

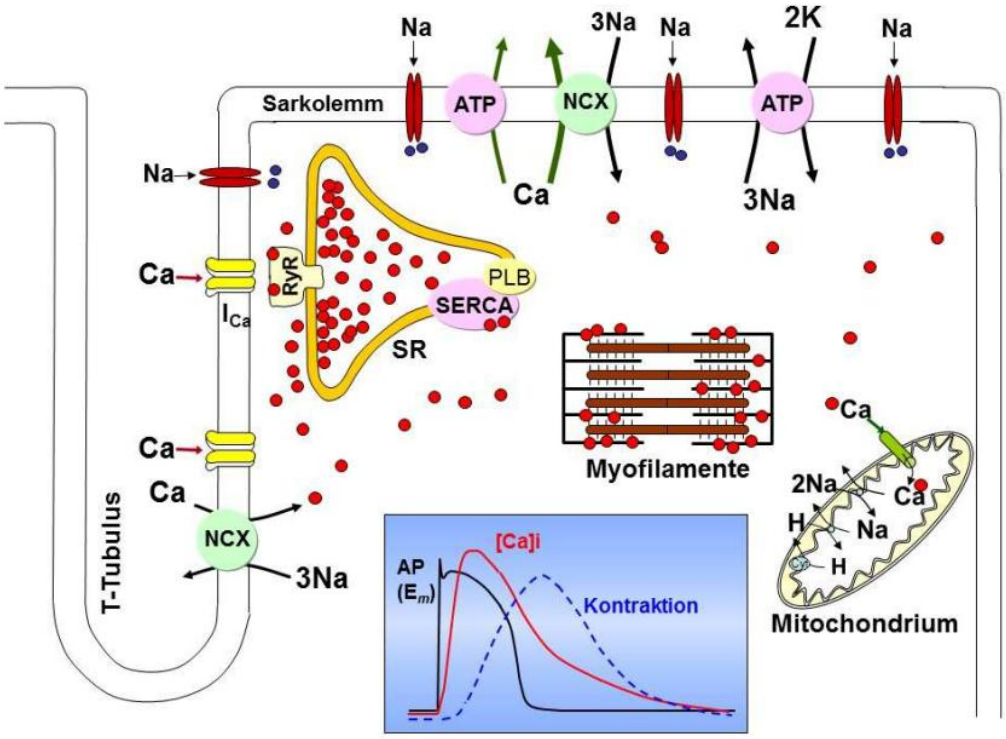

Figure 1. Electromechanical coupling of the myocardium. This schematic illustrates the membrane of a cardiomyocyte. The area in blue shows the progression of the action potential over time, alongside changes in Ca^{2+} levels and muscle contraction. In the process of electromechanical coupling, electrical stimulation results in Na^+ influx via voltage-dependent Na^+ channels. Subsequent depolarization permits Ca^{2+} entry through L-type calcium channels (LTCC), starting contraction. During diastole, Ca^{2+} is removed either by reuptake into the sarcoplasmic reticulum via the sarco/endoplasmic reticulum Ca^{2+}-ATPase (SERCA) or by extrusion from the cell through the Na^+/Ca^{2+} exchanger (NCX), thereby facilitating relaxation. This description was modified from [8].

The opening of voltage-gated L-type Ca^{2+} channels during the plateau phase of the action potential leads to an increase in intracellular Ca^{2+} concentration. Ca^{2+} ions thereby bind to cardiac ryanodine receptors type 2 (RyR2) located on the SR, triggering their opening and causing a further release of Ca^{2+} from the SR, a process known as Ca^{2+} induced Ca^{2+} release. This increase in cytosolic Ca^{2+} initiates the conversion of the chemical signal into mechanical contraction due to binding of cytosolic Ca^{2+} to

troponin C, inducing a conformational change in the troponin-tropomyosin complex. This uncovers the actin-myosin binding site and allows the myosin head to bind to the actin filament. Myosin heads then attach to actin filaments and consequently, through adenosine triphosphate (ATP) hydrolysis, pull the actin filament toward the center of the sarcomere, resulting in cardiac muscle contraction [10, 11]. The amount of Ca^{2+} that is released into the cytosol proportionally determines the magnitude of the contraction.

Cardiomyocyte relaxation, marking the onset of diastole, is regulated by several transport proteins, responsible to catalyze a decrease of the cytosolic Ca^{2+} concentration. The sarco/endoplasmic reticulum Ca^{2+}-ATPase (SERCA) plays a central role by actively transporting Ca^{2+} back into the SR, under energy consumption and against its electrochemical gradient. The reuptake leads to a decrease in cytosolic Ca^{2+} levels, causing a dissociation of Ca^{2+} from troponin C and thereby initiating muscle relaxation [12]. Another key mechanism regulating diastole is the Na^{+}/Ca^{2+} exchanger (NCX), which extrudes 1 Ca^{2+} ion from the cytosol in exchange for 3 Na^{+}, thereby contributing substantially to the final reduction of intracellular Ca^{2+} levels [13]. The extent of the decline in cytosolic Ca^{2+} determines the diastolic stiffness.

1.1.2.1 Calcium/calmodulin-dependent kinase II and its role in EC coupling

Calcium/calmodulin-dependent kinase II (CaMKII) is a serine/threonine kinase that is ubiquitously expressed and participates in diverse signaling pathways. In cardiomyocytes, it is activated by Ca^{2+} ions, thereby playing an important role in EC coupling processes such as the maintenance of Ca^{2+} homeostasis and facilitating Ca^{2+} reuptake [14]. Structurally, CaMKII consists of two stacked hexameric rings, with each subunit comprising an N-terminal domain responsible for kinase activity as well as a C-terminal association domain mediating oligomerization. An auto-regulatory region, which contains the Ca^{2+}/CaM-binding site, governs the enzyme activation through Ca^{2+}/CaM-binding as well as by auto-phosphorylation [15]. In the basal state, the regulatory domain sterically inhibits the catalytic domain, suppressing kinase activity. Upon Ca^{2+}/CaM binding, a conformational change occurs that relieves this auto-inhibitory effect and activates the enzyme [16, 17]. Previous studies have identified

additional Ca^{2+}/CaM-independent mechanisms of CaMKII activation involving post-translational modifications within the regulatory domain [18-20]. In particular, oxidation of two methionine residues (MET281/282) by reactive oxygen species induces a conformational change that renders CaMKII activity in a Ca^{2+}-autonomous manner under pro-oxidant conditions [18]. The resulting dysregulated and excessive CaMKII signaling profoundly disrupts Ca^{2+} handling and EC coupling properties. This was confirmed in mouse models where cardiac-specific CaMKII overactivation led to cardiomyopathy combined with frequent arrhythmia while CaMKII inhibition reduced susceptibility to ventricular arrhythmia [18, 21]. These findings underscore the important role of CaMKII in maintaining proper EC coupling while highlighting its contribution to the pathophysiology in heart diseases due to cardiac remodeling.

1.1.2.2 Ryanodine-receptor 2 and its role in EC coupling

The ryanodine receptor 2 (RyR2) is a ligand-gated Ca^{2+} channel predominantly expressed in cardiac muscle, where it plays a central role in EC coupling processes due to the triggering of Ca^{2+} induced Ca^{2+} release. With a molecular weight of approximately 2.2 MDa, RyR2 is the largest ion channel structure identified to date [22]. As described in chapter 1.1.2, RyR2 mediates the release of Ca^{2+} stored in the SR in response to cytosolic Ca^{2+} binding, thereby increasing its open probability and triggering Ca^{2+} release.

RyR2 function is modulated by a variety of interacting proteins and is tightly regulated at the post-translational level through phosphorylation due to interaction with the cellular kinases protein kinase A (PKA) and CaMKII. The phosphorylation of all four RyR2 subunits by CaMKII enhances Ca^{2+} release from the SR, while PKA-dependent phosphorylation similarly elevates the open probability in response to β-adrenergic stimulation. This kinase-driven activation is counterbalanced by dephosphorylation via protein phosphatase 1 (PP1) and protein phosphatase 2a (PP2a), establishing a dynamic equilibrium that allows precise control of RyR2 channel activity [23, 24].

Dysregulated RyR2 function due to hyperphosphorylation, often caused by increased CaMKII activation under pro-oxidant conditions, is often characterized by “leaky” RyR2 channels and consequent impaired intracellular Ca^{2+} homeostasis. Hereby, reduction

of Ca^{2+} ions in the SR due to the RyR2 induced Ca^{2+} leak leads to a diminished systolic Ca^{2+} release, limiting contractile function. The concurrent elevation of diastolic Ca^{2+} can trigger an NCX-mediated inward current depolarizing the cardiomyocyte membrane, as well as bind to myofilaments consequently increasing diastolic tension [25]. Dysregulated RyR2 function is therefore a major contributor to cardiac pathologies such as heart failure, as Ca^{2+} imbalances not only weaken contractile function but also promote arrhythmogenic events [26, 27]. Precise RyR2 regulation is therefore essential for maintaining cardiac performance.

1.1.3 Force-Frequency-Relationship

The human myocardium possesses several intrinsic mechanisms that support the rapid adjustment of cardiac contractile function in response to sudden changes in physiological demands, e.g. during physical exertion or stress. One important mechanism is the force-frequency relationship (FFR), which describes the ability of the heart to enhance myocardial contractility and isometric force proportionally with increasing heart rates. This is especially relevant as elevated heart rates shorten the diastolic filling time, leading to reduced stroke volume and consequently to decreased cardiac output. An increase in contractility therefore ensures adequate perfusion.

In the healthy human heart, this compensatory mechanism displays in a positive force-frequency relationship [28]. While the cellular mechanisms underlying the frequency-dependent modulation of contractility remains incompletely understood, evidence suggests that higher stimulation frequencies concomitantly enhance action potential frequencies, leading to increased cytosolic Ca^{2+} concentrations. This, in turn, promotes Ca^{2+}-induced Ca^{2+} release from the SR, resulting in greater $[Ca^{2+}]_i$ transients and thereby amplifying contractile force [29-31].

In contrast to the non-failing heart, a frequency-dependent potentiation of contractile force is typically absent in failing human hearts [32]. Instead, increasing stimulation frequencies often lead to a progressive decline in isometric tension development, indicating a negative force-frequency relationship. This impairment is primarily attributed to abnormal Ca^{2+} handling and consequent disrupted EC coupling at the level of the SR, particularly involving a reduction in SERCA activity and expression [28, 33].

The decreased SERCA levels in failing myocardium are thought to result from transcriptional downregulation, post-translational modifications, and chronic neurohumoral activation, which collectively reduce the protein's abundance and functional capacity to sequester Ca^{2+} into the SR, thereby impairing relaxation and systolic Ca^{2+} availability [34, 35].

Overall, the FFR serves as a valuable experimental parameter for evaluating contractile properties of cardiac tissue under varying stimulation frequencies and provides insights into the functional integrity of myocardial Ca^{2+} cycling.

1.1.4 Post-Rest-Potentiation

The post-rest contractile behavior of human myocardium provides valuable insights into the basic cellular mechanisms regulating cardiac muscle contraction. It reflects key processes such as transmembrane Ca^{2+} influx and Na^{+}/Ca^{2+} exchange and allows for the indirect assessment of the SR capacity to store and release Ca^{2+} [36]. The phenomenon of post-rest potentiation (PRP) occurs from the accumulation of Ca^{2+} within the SR during a pause in stimulation, which is driven by altered NCX dynamics that reduce Ca^{2+} extrusion while SERCA-dependent SR loading is enhanced [37]. Upon stimulation resumption, the accumulated Ca^{2+} results in a stronger contractile response with greater force amplitudes in human myocardium.

Previous studies demonstrated that SR Ca^{2+} accumulation and release capacity are impaired in failing hearts, leading to disrupted post-rest behavior and diminished contractile force [28, 38]. Hereby, a diminished SR Ca^{2+} uptake, likely due to decreased SERCA expression often found in HF, correlated with impaired PRP since less Ca^{2+} could be sequestered during rest intervals [33, 38, 39]. Given the central role of the SR in EC coupling, PRP serves as a valuable functional parameter to evaluate SR Ca^{2+} handling and its contribution to contractile dysfunction.

1.2 Pathophysiology of Heart Failure

1.2.1 Definition and classification of heart failure

Heart failure (HF) is a clinical syndrome defined as the inability of the heart to sufficiently supply blood to meet the metabolic demands of the body. It occurs as the final common pathway of various structural or functional cardiac disorders and still is associated with high morbidity and mortality rates. HF manifests with a variety of symptoms that reflect systemic and pulmonary congestion as well as impaired tissue perfusion, including dyspnea, edema and fatigue [40, 41].

Since HF is mainly characterized by impaired ventricular filling or ejection of blood, its classification is based on left ventricular ejection fraction (LVEF) into three categories: HF with reduced ejection fraction (HFrEF, LVEF <40%), HF with preserved ejection fraction (HFpEF, LVEF ≥50%) and HF with mildly reduced ejection fraction (HFmrEF, LVEF 40-49%) [41].

The diagnosis of HF is based on a combination of clinical evaluation, imaging, and biomarkers. Hereby, echocardiography is used to assess cardiac structure and function, consequently classifying the stage of HF based on the LVEF, while measurements of natriuretic peptides (e.g. NT-pro-BNP) and the assessment of symptoms in patients provide additional diagnostic information [41].

1.2.2 Current therapeutic approaches and remaining challenges

The treatment of heart failure is multifaceted and mainly aims to alleviate symptoms, prolong survival and improve the quality of life. Treatment strategies thereby orientate on the type and severity of HF. In patients with HFrEF, guideline-directed therapies involve medical intervention based on angiotensin receptor-neprilysin inhibitors (ARNi), beta-blockers, mineralocorticoid receptor antagonists (MRA) as well as sodium-glucose cotransporter-2 inhibitors (SGLT2i), which improved mortality [42]. In advanced cases, additional device therapy or even heart transplantation needs to be considered.

While current therapies are mainly directed toward neurohormonal modulation and hemodynamic support to enhance heart function, many patients continue to experience disease progression [43]. This highlights the need for a deeper understanding of the molecular and cellular mechanisms underlying the pathophysiology of HF, which is essential for the development of more effective and targeted therapies. Recent studies increasingly recognized the role of inflammation and immune cells in the pathophysiology of HFrEF, encouraging research into cardio-immunotherapies as potential novel therapeutic options [44-46]. However, despite the growing interest in immunomodulation, experimental interventions targeting immune cells in living human heart tissue have not been feasible yet as long-term culture of human myocardium in suitable in vitro systems is technically challenging. Therefore, further comprehensive research is essential to overcome this limitation.

1.3 Mitochondria

1.3.1 Mitochondrial function and oxidative phosphorylation

Since cardiomyocytes are highly specialized cells with very limited turnover capacity, they are particularly reliant on stable intracellular homeostasis and energy production to meet the heart's intense metabolic and mechanical demands and sustain contractile performance [47, 48]. Mitochondria are the primary source of energy in cardiomyocytes and occupy roughly one-third of the cellular volume [49, 50]. They generate ATP by harnessing energy released by oxidation of glucose and other substrates. Beyond their role in energy production, mitochondria further play essential roles in diverse cellular processes, including Ca^{2+} signaling, regulation of electrolyte homeostasis and apoptosis [51, 52].

Mitochondria are originally thought to have evolved over a billion years ago from symbiotic eubacterial ancestors that invaded early eukaryotic cells, and as a remnant, they kept their own genome (mtDNA) which still exhibits clear bacterial features [53, 54]. Structurally, mitochondria comprise an inner and outer phospholipid membrane, which define and separate two aqueous compartments: the intermembrane space and the mitochondrial matrix. While the outer mitochondrial membrane forms a boundary between the organelle and the cytosol, the inner membrane folds inward into cristae

that extend into and define the mitochondrial matrix. The inner mitochondrial membrane thereby contains the five enzyme complexes of the oxidative phosphorylation system (Figure 2), which catalyze sequential redox reactions that drive proton translocation across the membrane, consequently generating the electrochemical gradient required for ATP production [55, 56].

The process of oxidative phosphorylation starts with carbon substrates that enter the tricarboxylic acid cycle located in the mitochondrial matrix, where their oxidation produces NADH and $FADH_2$. These reducing equivalents provide electrons into the respiratory chain through Complex I (NADH dehydrogenase) and Complex II (succinate dehydrogenase), respectively. Electrons then converge at the naturally occurring coenzyme ubiquinone, continue through Complex III (ubiquinol-cytochrome c reductase) and are transferred by cytochrome c to Complex IV (cytochrome c oxidase), where oxygen is reduced to water. During this electron transfer, Complexes I, III and IV translocate protons into the intermembrane space via coupled redox reactions, thereby establishing an electrochemical gradient. In a last step, Complex V (ATP synthase) uses the proton-motion force generated by the gradient to drive the phosphorylation of adenosine diphosphate (ADP) to ATP [51, 57].

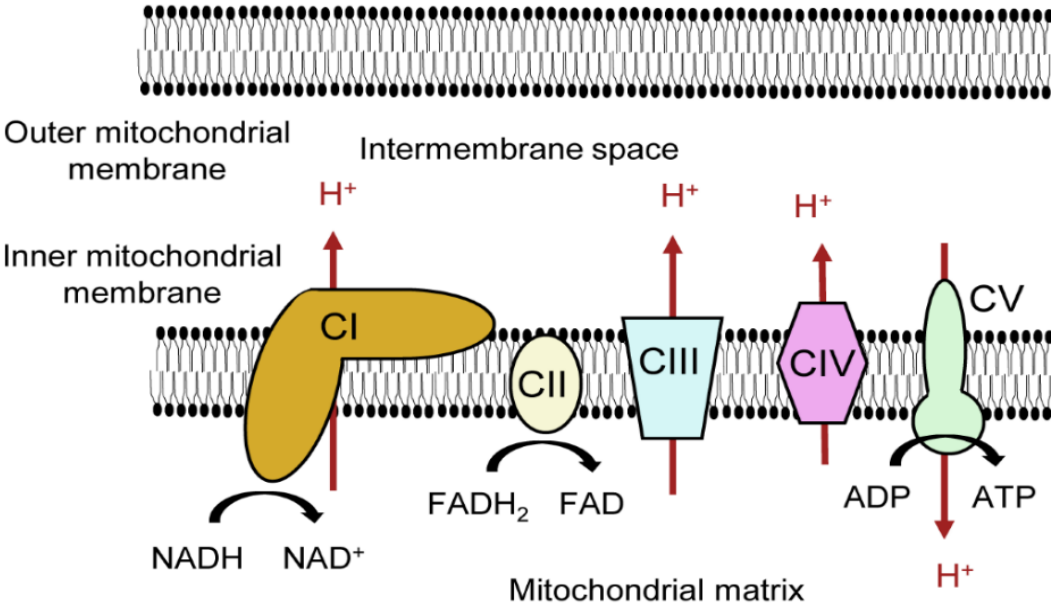

Figure 2. Mitochondrial electron transport chain and oxidative phosphorylation. Depicted are the five respiratory chain complexes located in the inner mitochondrial membrane. These complexes comprise complex I (NADH dehydrogenase; CI), complex II (succinate dehydrogenase; CII), complex III (ubiquinol-cytochrome c reductase; CIII), complex IV (cytochrome c oxidase; CIV) and complex V (ATP synthase; CV). Electron transfer from NADH and $FADH_2$ to molecular oxygen is mediated by complexes I-IV, a process coupled to proton translocation from the matrix to the intermembrane space. The resulting proton gradient drives ATP synthesis by CV. Modified from [58].

1.3.2 Mitochondrial quality control

The mitochondrial respiratory chain is crucial for the cellular homeostasis. It furthermore is the primary site of oxygen free radical generation, serving as both a source and a target of oxidative stress-induced damage, positioning mitochondria as essential contributors in cardiomyocyte health and disease [59, 60]. Robust mitochondrial quality control systems are therefore essential for maintaining stability and integrity of mitochondrial structure and function.

One important quality control mechanism involves the selective elimination of unrepairable damaged mtDNA by mitophagy pathways. Hereby, damaged mtDNA is segregated into mitochondria with low membrane potential during fission processes. These mitochondria are consequently recognized by mitophagy-related proteins (PINK1/Parkin pathway), selectively sequestered into autophagosomes and ultimately delivered to lysosomes for degradation [61, 62]. This process occurs under baseline conditions and is further activated in response to cellular stress [63-65]. Several studies reported that the impairment of these mechanisms results in adverse effects that can lead to contractile dysfunction [63, 66, 67].

Mitochondrial quality control mechanisms are essential in the heart. Thus, the maintenance of robust mitochondrial quality control is important for preserving cardiomyocyte function and overall cardiac health.

1.3.3 Mitochondrial dysfunction and ROS generation in heart failure

When mitochondrial quality control mechanisms fail, dysfunctional mitochondria accumulate within cardiomyocytes, resulting in impaired bioenergetics such as decreased oxygen availability, substrate oxidation and mitochondrial ATP production. This energy deficit does not only compromise contractile efficiency but also promotes adverse cardiac remodeling and cell death, contributing to the pathogenesis of heart failure [68].

Oxidative stress is considered a key factor driving cardiac remodeling in response to stress, as accumulated dysfunctional mitochondria are more susceptible to oxidative injury. While ROS signaling under physiological conditions regulates heart

development and cardiomyocyte maturation, pathological conditions lead to excessive ROS generation, which can directly damage mitochondrial proteins, aggravate mitochondrial dysfunction and further amplify myocardial impairment [68, 69]. The generation of ROS in the context of HF has been associated with persistent neurohormonal activation as well as increased myocardial stress due to pressure overload or hypoxic conditions [70, 71]. Furthermore, as mentioned in chapter 1.1.2.1, ROS can alter the Ca^{2+} homeostasis of cardiomyocytes due to activated CaMKII and hyperphosphorylation of RyR2 leading to SR Ca^{2+} leak, reinforcing contractile dysfunction in HF [18, 72].

The adverse effects of excessive ROS production in the context of HF highlight the importance of maintaining intracellular redox homeostasis and mitochondrial health to allow physiological ROS signaling while preventing the activation of pathological ROS signaling pathways.

1.4 Immune cells in cardiac health and disease

1.4.1 Cardiac immune cell populations

The healthy human heart consists of a heterogeneous population of cells, also containing a wide range of non-myocyte cells that far surpass cardiomyocytes in abundance. About 10% of non-myocytes are immune cells, with all leukocyte classes, including monocytes, lymphocytes (such as B- and T-cells) and granulocytes (neutrophils, eosinophils and basophils) present in frequencies that outweigh those in skeletal muscle [73, 74]. Cardiac immune cells are hereby commonly categorized based on their tissue residency or their recruitment during inflammatory responses and vary based on specific functions and expression profiles [75].

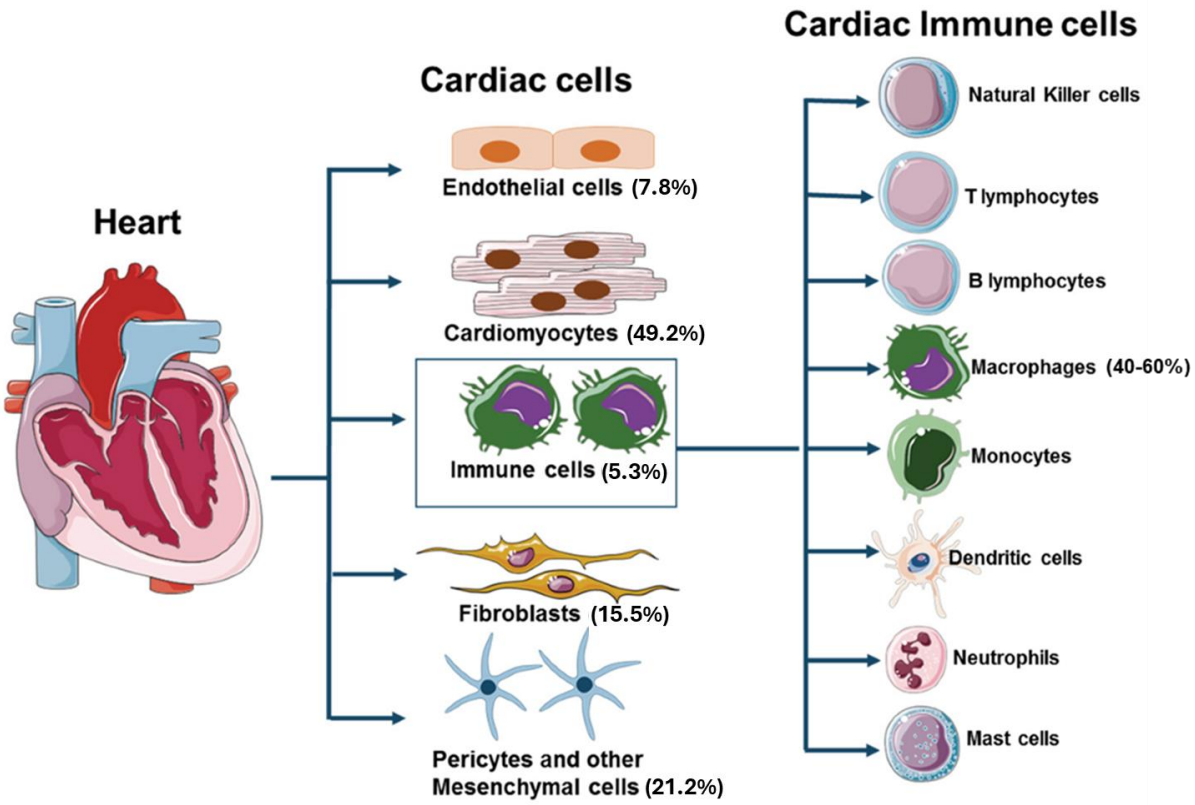

Figure 3. Cellular composition of the human heart and diversity of cardiac immune cells. Schematic illustration of the cellular composition of the LV in the healthy heart. Cardiomyocytes (≈49.2%) represent the major population, followed by pericytes and other mesenchymal cells (≈21.2%), fibroblasts (≈15.5%), endothelial cells (≈7.8%) and immune cells (≈6%). Cardiac macrophages hereby represent the predominant population of cardiac immune cells, making up approximately half of the total immune cells. Modified from [76, 77].

In the healthy heart, cardiac immune cells contribute to immunosurveillance by safeguarding against pathogens, toxic insults, hypoxic stress, and other forms of injury. However, immune cells in the heart fulfill a wide range of functions also beyond immune regulation. A key role is their participation in tissue repair and regeneration. This reparative capacity is especially prominent during heart development with neonatal hearts being able to fully regenerate, a function that is lost after the first few weeks of live [78, 79]. Further homeostatic roles are described in chapter 1.5.2. During myocardial aging, the composition and function of immune cell populations change significantly, and emerging evidence shows that autoimmune mechanisms may underscore these age-related shifts [73].

Cardiac immune cells do not only play important roles in the healthy heart but are also increasingly recognized as an essential contributor to disease state. Hereby, it has

been identified that cardiac immune cells dynamically change in transcriptional profile and physiological functions, thereby affecting disease progression [75, 80].

1.4.2 Expansion and activation of immune cells in heart failure

Immune cells play a complex and multifaceted role in HF and increasing evidence suggests that immunoinflammatory activation due to hemodynamic impairment can have an active part in disease progression [81, 82]. Initially, resident and infiltrating cardiac immune cells elicit an acute immune response by activating inflammatory and reparative pathways in order to counteract the hemodynamic stress and restore tissue function [83]. While immune cells are essential key players of cardiac healing, dysregulated or unresolved immune responses can aggravate tissue damage and trigger maladaptive remodeling [84]. In chronic HF, while limited inflammation may support short-term repair, it ultimately evolves into a persistent state that drives chronic inflammation and contributes to the progression of HF [85].

During pathological processes such as HF, danger-associated molecular patterns (DAMPs) are released and act as a key trigger for immune cell infiltration and activation. Consequently, innate immune cells like neutrophils, monocytes and macrophages not only proliferate locally but are also recruited from circulation due to elevated cytokine (such as TNF-α, IL-1 and IL-6) and chemokine levels [86, 87]. During this process, immune cells were demonstrated to undergo metabolic and phenotypic reprogramming toward pro-inflammatory states, also changing their distribution, polarization, and subtypes in the heart [88, 89]. Adaptive immune cells, such as $CD4^+$ and $CD8^+$ T lymphocytes, also expand and become activated, perpetuating the inflammatory response by secretion of cytokines and thereby sustaining disease progression [90].

Current clinical approaches targeting inflammation in cardiac disease have shown limited efficacy so far [91]. Since extensive anti-inflammatory interventions may entail adverse effects, future therapeutic approaches should focus on adjusting the balance between pro-inflammatory and reparative immune cell subsets to support effective healing.

1.5 Cardiac Macrophages

The predominant population of cardiac leukocytes is represented by macrophages (40-60%), which possess distinct ontogenies and a wide range of functions [92, 93]. While resident macrophages contribute to cardiac homeostasis, including electrical conduction and tissue repair, non-resident, monocyte-derived macrophages are primarily linked to inflammation, fibrosis and maladaptive remodeling of the heart [94-96]. Cardiac macrophages are widely distributed throughout the myocardium, where they form a dense and highly interconnected network. In the human heart, they account for 5% of all non-cardiomyocyte cells, with approximately five macrophages closely interacting with each individual cardiomyocyte [97, 98]. The crosstalk of macrophages and cardiomyocytes is thereby facilitated by direct membrane contacts and gap junctions, as well as by the exchange of signaling molecules such as cytokines [99-101].

1.5.1 Developmental origin and subtypes of cardiac macrophages

Cardiac macrophages consist of subtypes with distinct developmental origins. Resident macrophages originate from embryonic yolk sac hematopoiesis, seed the heart during embryonic development and are maintained locally by self-replication [102, 103]. In contrast to resident macrophages, monocyte-derived macrophages arise from definitive hematopoietic stem cells in the bone marrow and spleen and are recruited to the heart during injury or stress via classical monocyte intermediates [96].

The classification of cardiac macrophages into different subsets is mainly determined by their cell-surface expression. While all macrophages universally express CD45, CD68, CD11b, CD64, and MERTK, they mainly differ in terms of their expression of C-C Motif Chemokine Receptor 2 (CCR2). Cardiac resident macrophages can typically be identified by a shared set of surface markers including TIMD4, LYVE1, and FOLR2, while lacking the cell surface expression of CCR2 ($CCR2^{-}$). In contrast, classical monocytes and most monocyte-derived macrophages are generally marked by the expression of CCR2 ($CCR2^{+}$), while lacking TIMD4, LYVE1, and FOLR2 [75, 94, 96, 103].

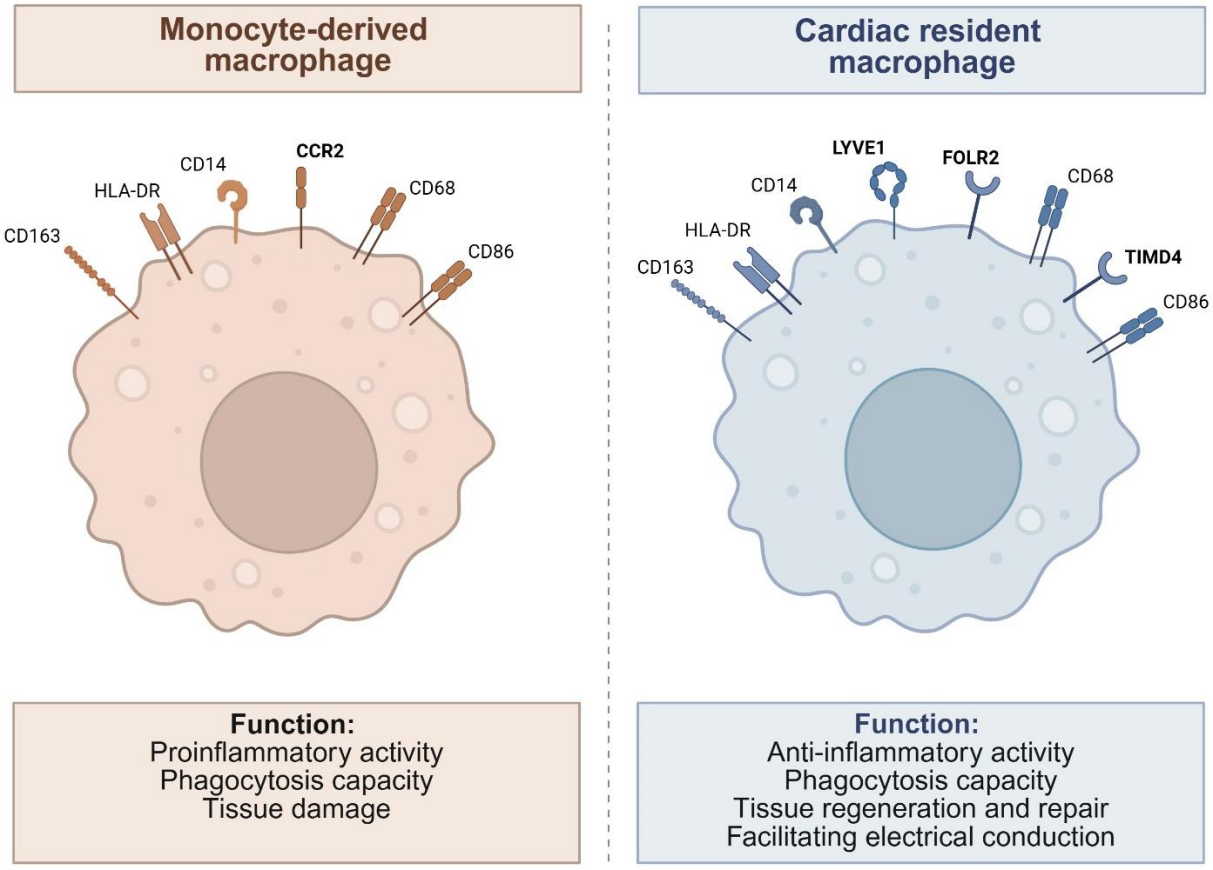

Figure 4. Distinct phenotypes and functions of monocyte-derived vs. resident macrophages. Schematic illustration of cardiac resident and monocyte-derived (recruited) macrophages and their distinct surface marker profiles and different functions. Markers shown in bold represent those that differ between the two macrophage subtypes. Not all known markers are depicted. Resident macrophages (right) are characterized by anti-inflammatory and tissue-reparative properties, while monocyte-derived macrophages (left) display proinflammatory and tissue-damaging functions. Created in https://BioRender.com.

Macrophage characterization studies have revealed that the neonatal heart is predominantly populated by embryonically derived cardiac macrophages, displaying a remarkable ability to recover cardiac function while eliciting minimal inflammation [78, 104]. During aging, the proportion of embryonically derived resident macrophages declines, while monocyte-derived macrophages accumulate. This process occurs likely due to increased low-grade inflammation and tissue stress, which is consequently accompanied by alterations in surface marker expression such as CCR2 levels, reflecting a more pro-inflammatory phenotype [105-107]. As a result, the aged myocardium contains a higher density of recruited macrophages, which may contribute

to impaired tissue homeostasis and increased susceptibility to maladaptive remodeling and HF [108, 109].

1.5.2 Homeostatic roles of cardiac macrophages

Recent findings underscore the critical function of cardiac resident macrophages in maintaining myocardial health, not only by mediating immune responses but also by navigating cardiac homeostasis through various mechanisms [99, 100, 110, 111].

A key function of cardiac macrophages is their role in tissue repair in neonatal hearts, which they facilitate by promoting cardiomyocyte proliferation and angiogenesis via secretion of growth factors such as IGF-1 and VEGF [79]. This process is primarily orchestrated by resident $CCR2^-$ macrophages, although recruited $CCR2^+$ macrophages can undergo phenotypic shifts from pro-inflammatory to reparative states that help limit tissue damage and support regeneration [76, 112]. In adult hearts, while proliferation of cardiomyocytes is extremely limited, cardiac resident macrophages still contribute to tissue repair by modulating inflammation, promoting angiogenesis and clearing cell debris via phagocytosis [79, 113]. They were furthermore shown to regulate fibroblast activation and extracellular matrix remodeling to ensure balanced scar formation and mitigate the risk of pathological fibrosis [114].

It has furthermore been demonstrated that cardiac resident macrophages facilitate electrical conduction via direct electrical connections with cardiomyocytes in the distal AV node, utilizing Cx43-containing gap junctions. Electronic coupling between cardiomyocytes and macrophages depolarizes resting cardiomyocytes and shortens their action potentials, permitting faster conduction rates. A macrophage-specific knockout of Cx43 in mice resulted in impaired AV node conduction, underscoring the critical role of macrophages in maintaining proper cardiac conduction [99].

Several studies have also demonstrated that cardiac macrophages enhance cardiomyocyte contractility, whereas a loss of macrophages led to structural alterations and impaired mechanical performance [113, 115, 116]. In an iPSC-derived human engineered cardiac tissue model, the presence of resident macrophages significantly increased active force generation and overall contractile function compared to

macrophage-depleted tissues, likely through stimulation of the β-adrenergic signaling pathway [116].

Only recently, a novel function of cardiac macrophages was discovered. It involves the clearance of damaged mitochondria from cardiomyocytes via subcellular vesicles into the extracellular space, where resident macrophages subsequently uptake and degrade them through phagocytosis [101, 117]. This mitochondrial clearance mechanism provides new insight into mitochondrial quality control, which was previously considered to depend mainly on intracellular pathways [118, 119]. The significance of this mechanism is demonstrated by murine studies indicating that cardiac macrophage depletion leads to the accumulation of dysfunctional mitochondria, activation of inflammasomes, disruption of autophagy, and subsequent metabolic impairment [101, 120].

All these findings provide an enhanced perspective on cardiac resident macrophages as vital regulators of cardiac homeostasis, extending their function beyond traditional immune surveillance. Given that disruptions in these interactions can drive maladaptive remodeling, it furthermore highlights their role as mediators in cardiac health and disease.

1.5.3 Pathological roles of cardiac macrophages in heart failure

During cardiac diseases such as HF, macrophages undergo several alterations that can contribute to disease progression. Under pathological stress, macrophage frequencies expand, and resident macrophage populations are supplemented and gradually replaced with infiltrated monocyte-derived macrophages. This expansion in macrophage population may promote a shift from anti-inflammatory, reparative macrophages to pro-inflammatory subsets, creating a sustained inflammatory milieu and driving maladaptive tissue remodeling [94, 95, 121].

Recent studies demonstrated that HFrEF enhances bone marrow myelopoiesis, thereby expanding the systemic pool of innate immune cells [121]. Moreover, recruited monocyte-derived $CCR2^{+}$ macrophages have been identified as key regulators of myocardial inflammation and contributors to HF progression [94, 113, 121]. In advanced HF patients, higher $CCR2^{+}$ macrophage abundance thereby correlated with

more severe adverse remodeling [94]. In contrast, depletion of anti-inflammatory resident CCR2^{-} macrophages, cells that are commonly replaced by infiltrating monocyte-derived macrophages in HF pathology, accelerated mortality and disrupted ventricular remodeling, undermining the adaptive structural responses needed to maintain cardiac output as contractile function declines, thereby exacerbating HF [113].

Cardiac fibrosis commonly arises as a consequence of chronic myocardial injury and is defined by the accumulation of extracellular matrix (ECM) proteins within the cardiac interstitium to replace necrotic cells. Hereby, the extent of fibrotic remodeling is closely related to adverse outcomes [122, 123]. Macrophages and fibroblasts communicate via intercellular mediators, mutually influencing each other's quantity, distribution, phenotype and function. During cardiac repair, recruited macrophages secrete pro-fibrotic mediators such as TGF-β, IL-1β and PDGF which directly trigger fibroblast activation, proliferation, and their differentiation to myofibroblasts [124]. This process contributes to increased wall thickness, impairs both systolic and diastolic function, and ultimately compromises overall cardiac performance.

Together, these maladaptive processes establish a vicious cycle of inflammation, fibrosis and contractile dysfunction while highlighting the important role of cardiac macrophages in the progression of HF.

1.5.4 Cardiac macrophages as immunotherapeutic targets

The pivotal role of macrophages in cardiac physiology and pathology establishes them as a potential target for cardiac immunotherapy [46]. Specifically in HF, modulating immune-cardiomyocyte interactions may offer a novel therapeutic approach to enhance myocardial function [94, 101]. However, targeting cardiac macrophages faces several important challenges. A major limitation is the vast heterogeneity of macrophage subsets in the heart, possessing distinct and even opposing functions [94, 121]. During the progression of chronic HF, macrophage phenotypes may even become more variable, as some recruited macrophages can alter their transcriptional characteristics and function over time [96, 125]. Although macrophages are often viewed primarily as pro-inflammatory targets in therapeutic interventions, broad

suppression of their activity without considering their essential physiological and homeostatic roles could negatively affect important functions, including debris clearance, angiogenesis and electrical conduction [99, 101].

Another major challenge in targeting cardiac macrophages for immunotherapeutic interventions involves the translation of insights from preclinical models to human application. So far, macrophage interventions have been investigated predominantly in animal models. However, given the substantial interspecies differences in cardiac macrophage ontogeny, subset composition and kinetics, it is essential to validate macrophage interventions also in living human models, which has not been possible yet.

Together, these challenges underscore the need for the establishment of translational relevant models to test macrophage interventions in living human heart tissue.

1.5.5 CSF1R inhibition as a tool for macrophage depletion

One common strategy to investigate the function of cardiac macrophages is their targeted depletion. The selective deletion thereby allows to assess how the absence of macrophages affects cardiac homeostasis, providing valuable insights into their specific functions. To achieve macrophage depletion, the Colony-stimulating factor 1 receptor (Csf1R) is often used as a target. The working mechanism is based on inhibition of kinase activity of the Csf1R, a receptor tyrosine kinase expressed by monocytes, macrophages and microglia. This prevents autophosphorylation of the receptor and consequently the activation of different signal cascades. Since Csf1R regulates the proliferation, differentiation and activity of macrophages, the absence of signal cascades due to Csf1R inhibition leads to missing differentiation signals and apoptosis of cells [126, 127].

In several studies, the Csf1R inhibitor (Csf1Ri) PLX-5622 has been effectively used across various species to deplete microglia and macrophages, providing critical insights into their functional role [128-130]. Even though it was predominantly used in mice, PLX-5622 also showed significant effects in a human in vitro model (individualized patient tumor organoid (IPTO)) with Csf1R activity nearly completely blocked by PLX-5622 [131, 132]. The broad pre-clinical use makes macrophage

depletion via Csf1R inhibition a reliable and validated approach, as dosing regiments and potential off-side effects are already established.

1.6 Translational aspects of studying human myocardium

Cell-based in vitro assays are widely used for examining molecular mechanisms in the heart. However, analyzing long-term effects in human myocardium remains challenging, as human cells typically do not maintain functional stability beyond 24–48 hours after isolation. Additionally, the reliability of these experimental models and their ability to represent cell behavior in native tissue is uncertain, given that isolated cells lack the environmental context and structural organization found in tissues, which are important for various cellular processes [133]. Stem-cell derived engineered heart tissue is often used to replace single cell models, however, they have not yet reached comparable maturity and physiological properties of human myocardium [134]. Therefore, better models are needed to improve translatability of preclinical findings.

A major advancement in this field was achieved with the introduction of the MyoDish-1 tissue culture system (InVitroSys GmbH, Gräfelfing), which enables long-term culturing of human atrial and ventricular tissue [135]. Hereby, precision-cut myocardial slices are positioned within culture chambers attached with a force transducer, subjected to electrical stimulation, and subsequently evaluated for contractile performance and kinetics, including beta-adrenergic response and refractory period assessment. Additional functional tests, such as FFR and PRP measurements, allow assessment of contractile performance across varying stimulation frequencies and provide insights into the functional integrity of myocardial Ca^{2+} cycling. After long-term culture (weeks up to months), cardiac tissue can be isolated into single cells and analyzed for electrophysiological properties such as Ca^{2+} signaling and gene expression profiles. This new method of myocardial tissue culture allows for the study of long-term effects and structural functions in human myocardium by preserving not only cardiomyocytes but also all other cardiac resident cells, preventing the rapid degradation observed in isolated adult cardiomyocytes. Accordingly, this multicellular three-dimensional *in vitro* model was also examined as part of this thesis.

2 Objective

Cardiovascular diseases such as HFrEF, despite modern medical advances, remain the leading cause of mortality worldwide. While current therapies primarily target neurohormonal pathways to improve heart function, many patients still experience ongoing disease progression. This highlights the need to explore new pathways. Growing evidence underscores the importance of inflammation and immune cells, especially of cardiac macrophages, in the pathophysiology of HFrEF, prompting cardio-immunotherapies as potential new therapeutic approaches. However, despite increasing interest in cardiac immunomodulation, direct experimental interventions targeting immune cells in living human heart tissue have not yet been possible.

The objective of this thesis was to investigate the functional role of cardiac macrophages in human heart failure by using long-term cultured living and beating human heart tissue from patients with HFrEF. Specifically, this study aimed to determine the effects of macrophage depletion in human heart tissue on contractile performance, excitation-contraction coupling, oxidative stress, apoptosis and mitochondrial function in order to provide mechanistic insights into the contribution of cardiac macrophages to myocardial function in heart failure.

3 Material and Methods

3.1 MyoDish-1 tissue culture system

3.1.1 Construction of the system

The MyoDish-1 tissue culture system (InVitroSys GmbH, Gräfelfing) comprises a baseplate housing a main circuit board with eight slots for culture chambers, each equipped with an external sensor circuit board. The main circuit board is mounted on a movable bearing and driven by a stepper motor, enabling a controlled rocking motion. The resulting motion generates medium circulation within the chambers, thereby enhancing oxygenation and facilitating the delivery of nutrients to the cultured tissue. Furthermore, motion aids in the removal of metabolic waste products from the tissue into the surrounding medium, an essential step for the maintenance of viable cardiac tissue cultures. The sensor circuit boards, mounted externally to the culture chambers without direct contact with the tissue or medium, are equipped with insertion connectors for electrodes. These electrodes interface with the main circuit board, transmitting sensor data to the controller unit, which serves as an interface to the computer while also ensuring the voltage supply and control of the system (Figure 5) [135].

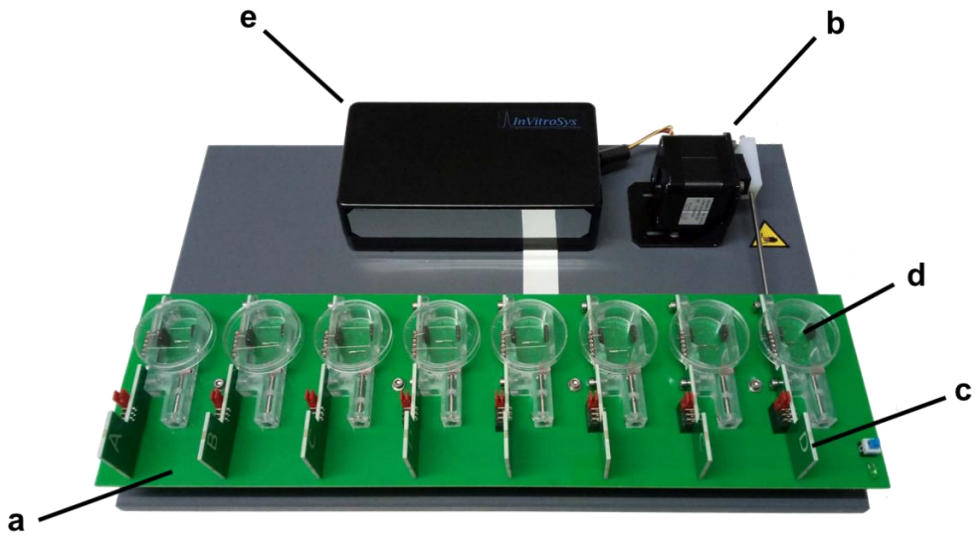

Figure 5. MyoDish-1 tissue culture system. The MyoDish-1 tissue culture system includes a baseplate with the main circuit board (a), which is mounted on a movable bearing operated by a stepper motor (b). Sensor circuit boards (c) with eight fixed culture chambers (d) are connected to the main circuit board to relay sensor data to the controller (e). Source: http://www.invitrosys.com/.

3.1.2 Design of culture chambers

Each of the eight culture chambers mounted on the circuit board was constructed from polystyrene and contained an adjusting wire (grade 1.441, 0.4 -mm diameter), a spring wire (grade 1.4401, 18 mm long) with magnet (NdFeB, 1 mm length, 0.5-mm diameter, HKCM engineering, Germany) as well as an adjusting bolt. The adjustment and spring wires served to secure the tissue slices within the chamber, which were suspended using plastic triangles affixed to the tissue. The spring wire additionally functioned as the force transducer for contractility measurements. Tissue preload was regulated by adjusting the position of the adjustment bolt. The design and volume of the culture chambers allowed for the containment of up to 2.5 mL of culture medium without spillage during stepper motor-induced rocking motion. To facilitate gas exchange while minimizing the risk of contamination, all chambers were loosely covered with a shared 35 mm-diameter Petri dish lid (Sarstedt, Germany), which did not form an airtight seal. Electrical stimulation was delivered via two graphite electrodes (6 × 8 mm^2, CG1290, CGC Klein, Germany), which were placed at 20 mm distance at both sides of the tissue and were linked to the sensor boards using steel wires (grade 1.4401, 0.4-mm diameter) (Figure 6).

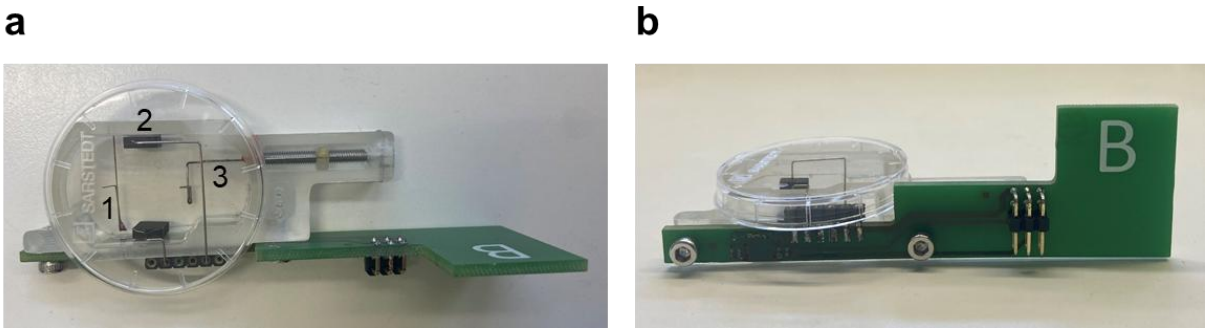

Figure 6. Design of biomimetic culture chambers. (a) Representation of a cultivation chamber containing the spring wire with magnetic tip (1), graphite electrodes (2) and adjusting wire (3), covered by a Petri dish lid (b) Graphite electrodes are connected to the main circuit board via connection pins.

3.1.3 Stimulus generation and force monitoring

Bipolar electrical stimulation pulses were generated by an adjustable current source (LT1970, Linear Technology, USA) and delivered in series through the culture chamber electrodes. Impulse intensity was controlled by the output current and stimulation

parameters could be adjusted individually for each culture chamber. All stimulation parameters, including stimulus sequence, rate, pulse duration and current, were defined via commands and freely programmable protocols transmitted from the MyoDish software to the controller. Within each stimulation sequence, the exact time points of individual pulses were specified and repeated after a pre-defined stimulation interval. Stimulation timing for each individual chamber within the stimulation period could also be individually defined by the user. Contraction force of cultivated myocardial tissue was measured using patented technology (EP3176252A1, InVitroSys GmbH, Gräfelfing) integrated into the culture chambers and sensor boards. Data were continuously transmitted to the controller unit and recorded by the MyoDish software on a USB-connected computer. Real-time contractility data were visualized with a custom-written program based on the free library “Oscilloscope_DLL” (M. Bernstein, https://www.oscilloscope-lib.com). Recorded data were imported and analyzed using LabChart Reader (AD Instruments, Australia) [135].

3.2 Patients

Collection and use of patient tissue were authorized by the local ethics committee of the University of Regensburg (20-1776-101), the Ruhr University Bochum (13/2009) and the University of Gießen (AZ 184/24). All experiments were conducted in compliance with the ethical principles outlined in the Declaration of Helsinki.

Myocardial tissue was collected from 12 patients with end-stage heart failure (HF) undergoing heart transplantation, through a collaboration with the Clinic of Thoracic and Cardiovascular Surgery at the Heart and Diabetes Center Bad Oeynhausen and the University Hospital Regensburg, Germany. Left ventricular myocardial tissue was immediately immersed in cooled cardioplegic solution (Custodiol, 2204511, Dr. Franz Köhler Chemie GmbH, Germany) supplemented with 2 g of 2,3-butanedione monoxime (BDM) (10223744, Alfa Aesar, USA) and transported to the laboratory at 4°C.

3.3 Preparation of myocardial tissue specimens for tissue culture

Immediately upon arrival, tissue samples were freed from connective tissue and intramuscular fat and subsequently trimmed to a block with a ~10 × 10 mm^2 cross-sectional area. The tissue block was embedded in 4% low-melt agarose (Roth, Germany, dissolved in glucose-free slicing buffer at 80 °C, applied at 37 °C), mounted on the cooled (4°C) stage of a vibratome (VT1200S, Leica Biosystems, Germany) and consequently sectioned in the epicardium-tangential plane (2.4 mm vibration amplitude, 0.08 mm/s feed rate, razor blade “Gillette Silver Blue”) while kept in ice-cold slicing buffer (Table 1). Resulting slices of 300 µm thickness were affixed with Histoacryl (B.Braun Melsungen AG, Germany) to plastic triangles cut from 0.1-mm-thick polyester copier clear film (MGW5504, MGW Office Supplies, Germany), ensuring a ~5 × 5 mm^2 muscle section was aligned with longitudinal fiber orientation between fixation points. Slices were then transferred into biomimetic culture chambers containing 2.4 mL pre-warmed (37 °C) culture medium (Table 2), preload on the elastic and fixed holding wire was set to 1 mN and electrical stimulation (50 mA, 1 ms, 0.5 Hz) was initiated [135]. Preload was again set to 1 mN after 24 hours of cultivation and left unchanged during the rest of the culture period. Measurements were performed following an equilibration period of approximately 7-10 days (Figure 7) [135].

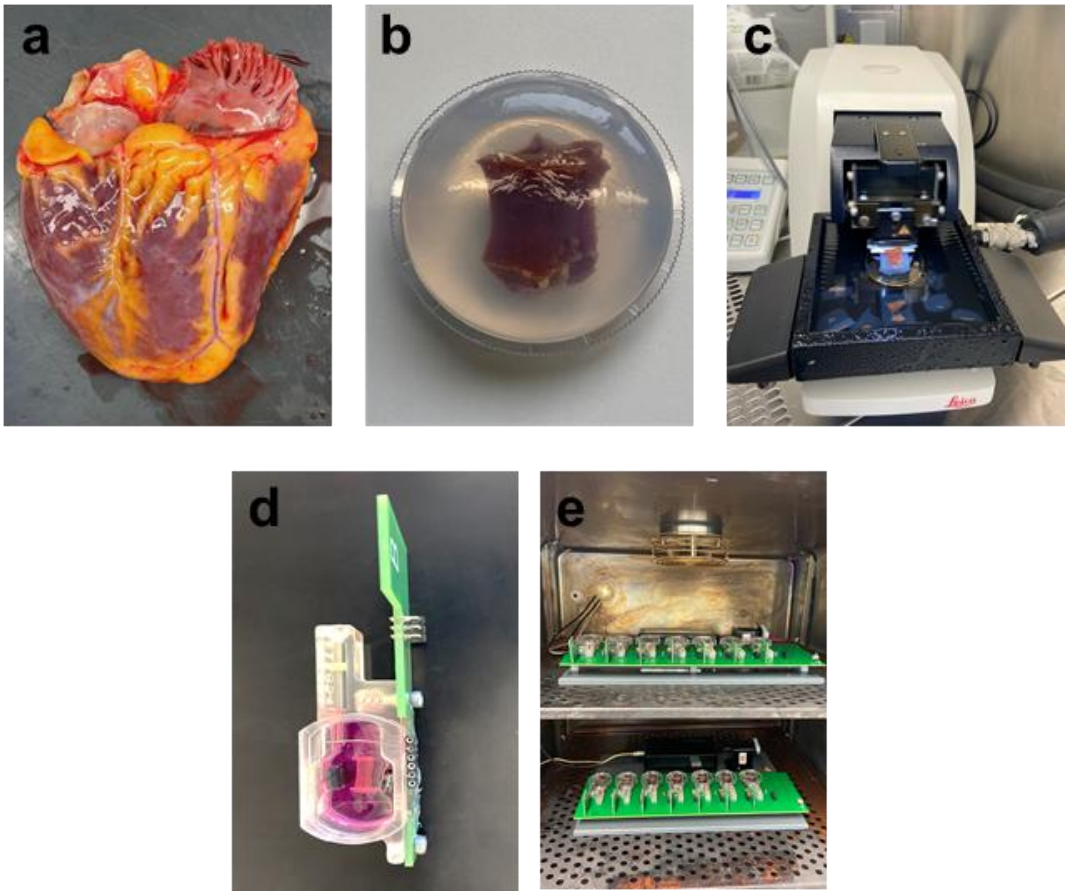

Figure 7. Preparation of human cardiac tissue and consequent cultivation. (a) Explant hearts from patients with HFrEF were collected and transported to the laboratory. (b) Human myocardial LV tissue was cut into 10 x 10 mm^2 pieces and embedded in 4% low-melt agarose. (c) Tissue blocks embedded in agarose were cut with a vibratome into 300 µm thick slices. (d) Freshly cut tissue slices were fixed with aligned longitudinal fiber orientation into culture chambers containing culture medium. (e) Culture chambers were put onto a circuit board located in a standard incubator and stimulation was initiated via the MyoDish-1 tissue culture system.

Table 1. Composition of slicing buffer

Substance	g/l	Concentration (mM)
NaCl	8	136
KCl	0.4	5.4
$MgCl_2$*6 H_2O	0.2	1
NaH_2PO_4* 2 H_2O	0.05	0.33
Glucose	1.8	10
BDM	3	30
HEPES	1.2	5
$CaCl_2$-Lösung (1M)	900 µl	0.9
Diluted in dH_2O, pH= 7.4		

Table 2. Composition of tissue culture medium

Substance	Volume	Manufacturer
Medium199	500 ml	Gibco, 31150-022
Insulin-Transferrin-Selenium-Ethanolamin (ITS-X) (100x)	5 ml	Gibco, 5150056
Penicillin-Streptomycin (100x)	5 ml	Sigma, P0781-100ML
Medium 199 + P/S + ITS	50 ml	
β-Mercaptoethanol	1,8 µl	Applichem, A1108,100
Dexamethason	5 µl	Merck, 265005-100MG
Amphotericin B	100 µl	Gibco, 15290018

3.4 Maintenance of tissue culture

Culture platforms comprising eight individual chambers were placed in a standard incubator (37 °C, 5% CO_2, 20% O_2, 100% humidity) and continuously subjected to rocking motion (60 rpm, 15° tilt angle, Hi/ Lo-Rocker, IBI Scientific, USA, equipped with brushless motor BLH230KC-30, Orientalmotor, Germany). During equilibration, tissue slices were paced at 0.5 Hz (30 bpm) with bipolar 50 mA pulses (1 ms charging and discharging, separated by 3 ms). This low, non-physiological rate was applied to minimize oxygen and nutrient demand to allow a better adjustment of tissue slices. Stimulation was switched to 1 Hz (60 bpm) one day prior to the experiment. Slices were maintained in Medium 199 supplemented with 1% penicillin/streptomycin, insulin/transferrin/selenite, dexamethasone (20 nM) and 2-mercaptoethanol (50 µM). Partial medium exchange (1.6 mL of 2.4 mL per chamber) was performed every 2-3 days.

3.5 Pacing protocols

After reaching a steady-state in relation to the contraction force of the different slices, pre-defined stimulation protocols were applied daily to assess the systolic force amplitude, the post rest potentiation (PRP) and the force-frequency relationship (FFR) of the myocardium (described in chapter 1.1.3 and 1.1.4). During all pacing protocols,

the rocking motion of the culture platform was intermittently paused to record multiple consecutive contractions, thereby minimizing artifacts caused by medium movement and ensuring reliable contractility measurements. These artifacts originate from inertial and gravitational forces acting on the spring wire, leading to motion-induced low-frequency noise in the recorded contraction signals. Only contractions recorded during rocking-free periods were considered. Effective stimulation and consistent capture of tissue slices were continuously controlled throughout all pacing protocols.

3.5.1 Long-term cultivation and macrophage depletion in human heart tissue

After an equilibration period of 7-10 days, cultivated human LV tissue slices were treated with 25 µM Colony-stimulating factor 1 receptor (Csf1R) inhibitor PLX-5622 (HY-114153, MedChemExpress) for 10 days. A 25 µM concentration of PLX-5622 has previously been used in patient-derived tumor explants and was confirmed to effectively deplete macrophages [132]. Contractility was assessed every 24 hours throughout the whole treatment period. Medium was changed every 2-3 days and collected medium was frozen and stored at – 80°C for further experiments.

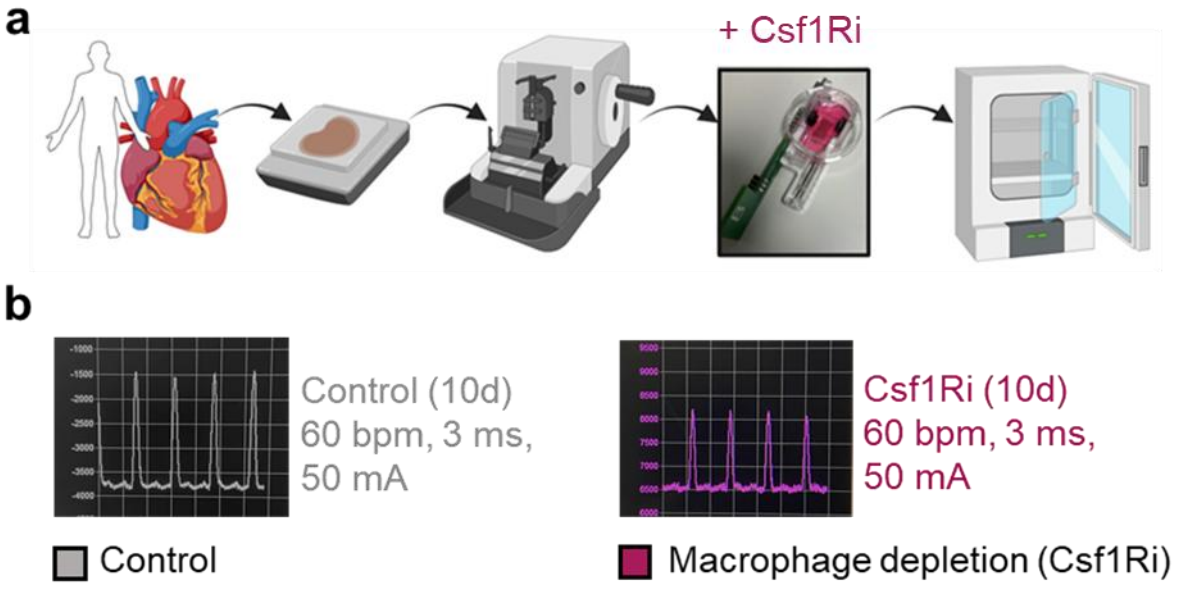

Figure 8. Long-term cultivation and experimental set-up. (a) LV tissue from explanted hearts from HFrEF patients was embedded in agarose, sliced with a vibratome, placed into cultivation chambers and subsequently long-term cultured in a standard incubator. (b) Stimulation was set to 60 beats-per minute (bpm), 3 ms and 50 mA for both groups. After an equilibration phase of approximately 7-10 days, Csf1Ri was added to the experimental group for 10 days and contractility was measured throughout.

3.5.2 Force-frequency-relationship

To assess the force-frequency-relationship (FFR) of HF slices treated with Csf1Ri compared to vehicle controls, FFR was measured on days 0, 5 and 10. A pacing protocol was applied at increasing stimulation frequencies of 0.5, 1, and 2 Hz with one minute stimulation time, respectively. To quantify the FFR, the mean value of 10 contractions at each frequency were normalized to baseline values obtained at 0.5 Hz prior to frequency escalation.

3.5.3 Post-rest-potentiation

To investigate post-rest behavior in HF slices treated with Csf1Ri compared to vehicle controls, measurements were obtained on days 0, 5 and 10, with a baseline frequency of 1 Hz. Following one minute of steady-state pacing, electrical stimulation was paused under stable conditions for progressively increasing rest intervals of 10 and 30 seconds. Subsequently, 1 Hz stimulation was resumed to assess post-rest potentiation of contractile force. After each rest interval, 1 minute of normal pacing was applied to ensure complete mechanical stabilization of the myocardial slices, before the next rest interval was imposed. Post-rest behavior was quantified by calculating the ratio of the contractile force of the first twitch following each rest interval to that of the final twitch immediately preceding the pause.

3.6 Isolation of cardiomyocytes from human tissue slices

For cardiomyocyte Ca^{2+} imaging, cardiomyocytes were isolated after 5 days of Csf1Ri-treatment (Figure 9). Human myocardial tissue slices were individually treated with 30 mM BDM, freed from the plastic triangles, placed into dishes and washed in isolation solution (2 x 3 min) (Table 3). Throughout the whole digestion, dishes containing the tissue slices were placed on a shaker at 37°C and agitated at 65 rpm. Slices were then digested with proteinase bacterial type XXIV (Sigma, 1 mg/ml) for 10 min and consequently with collagenase type I (EMD Millipore Corp., 2 mg/ml) for 9 min, each diluted in isolation solution. Once individual myocytes became visible, enzymatic

digestion was stopped using a stop solution (Table 4). Tissue slices were gently dissociated with forceps and Ca^{2+} concentration was gradually increased from 5 µM to 1.5 mM (followed by 2 mM in the working solution). Cells were then plated onto laminin-coated chambers and allowed to settle for 30 min.

Figure 9. Isolated cardiomyocytes from cultivated human HFrEF tissue slices. Representative picture of isolated human cardiomyocytes obtained after 7 days of Csf1Ri treatment. Cardiomyocytes were isolated from myocardial tissue slices using sequential enzymatic digestion (proteinase XXIV, collagenase type I) followed by gradual Ca^{2+} increase.

Table 3. Composition of isolation solution

Substance	g/l	Concentration (mM)
Isolation solution		
KCl	1.491	20
$MgCl_2$	0.952	10
KH_2PO_4	1.560	10
Glutamic acid	10.299	70
Taurine	2.504	20
pH 7.3 with KOH (37°C)		
Glucose	0.18	10
BSA	0.2	2 mg/ml

Table 4. Composition of stop solution

Substance	g/l	Concentration (mM)
Stop solution		
KCl	1.491	20
$MgCl_2$	0.952	10
KH_2PO_4	1.560	10
Glutamic acid	10.299	70
Taurine	2.504	20
pH 7.3 with KOH (37°C)		
Glucose	0.18	10
BSA	1	10 mg/ml
$CaCl_2$ (10 mM)	50 µl	0.0005

3.7 Ca^{2+} Cycling measurements with epifluorescence microscopy

3.7.1 Basic principle of epifluorescence microscopy

Fluorescence is a process in which a material is excited by light of a specific wavelength and subsequently, after a time delay, emits light of a longer wavelength [136]. In fluorescence microscopy, this property is exploited by labeling samples with fluorescent dyes and stimulating them with excitation light. The resulting emission light can be separated from the excitation light using an optical filter, allowing detection of the signal. The so-called Stokes shift, the difference between excitation and emission wavelengths, is hereby essential for distinguishing fluorescence signals [137]. This spectral separation allows the specific detection of emission light. Fluorescent dyes can be categorized as ratiometric or non-ratiometric. Ratiometric dyes allow the derivation of unknown quantities from the ratio of two measured signals [137, 138]. An example of a ratiometric dye is Fura-2AM, which absorbs light at both 340 nm and 380 nm and emits at 510 nm [139]. The ratio of the two measured intensities remains unaffected by external factors such as bleaching or dye loss, as both are affected to the same extent [138]. This makes Fura-2AM particularly suitable for the (semi-) quantitative measurement of Ca^{2+} concentrations over longer periods.

To facilitate cellular uptake, Fura-2AM is esterified with an acetoxymethyl group (AM), allowing it to pass through the cell membrane [138]. Inside the cell, the AM group is

cleaved by cytosolic esterases, leading to the formation of the ion-binding salt form and thereby preventing leakage of the dye from the cell. When fura-2 binds Ca^{2+}, forming a chelate-complex, the absorption maximum shifts from 380 nm to 340 nm, but the emission maximum remains constant at 510 nm [138]. The Ca^{2+} concentration can be determined via the ratio of the fluorescence intensities at 340 nm and 380 nm (F340 nm/F380 nm). These values are semiquantitative and are always interpreted in comparison to a control group. During measurements with the epifluorescence microscope, the temporal change of the Ca^{2+} concentration in the cardiomyocytes is visualized and the released systolic Ca^{2+} transients are recorded.

3.7.2 The epifluorescence microscope

In this work, an inverted microscope (Nikon Eclipse TE2000-U) equipped with a 40x oil-immersion objective was used. The excitation light emitted from the lamp (Cairn Research, high-intensity arc lamp) is directed onto a galvanometric mirror that can switch between two excitation wavelengths. The beam then passes through a dichroic mirror, which reflects the short-wavelength excitation light and transmits the long-wavelength emission light. This directs the excitation light onto the examined sample, while the emission light is directed to the emission filter, which removes stray light. The filtered fluorescence is passed on to the photomultiplier (Ion Optix Fluorescence system Interface), which amplifies the light and converts it into electrical voltage. An analog-to-digital converter (Ion Optix Hiper Switch) translates the voltage into a digital signal, which is processed by the Ion Wizard software (Ion Optix, Ion Wizard 5.0). During the measurements, the examined cells are stimulated with the Myopacer (Ion Optix Myopacer Field Stimulator).

3.7.3 Measurement of Ca^{2+} transients and SR Ca^{2+} content

Isolated cells from human cultivated tissue slices were plated on laminin-coated chambers and mounted on an inverted microscope (Nikon Eclipse TE2000-U). Cardiomyocytes were loaded with Fura-2AM (Invitrogen, F1221) in the presence of 0.05% w/v Pluronic F-127 (Sigma-Aldrich) for 15 min followed by 15 min incubation in Tyrode`s solution (Table 5) to allow de-esterification of the dye. Fura-2 fluorescence

ratios were determined using alternating excitation at 340 and 380 nm, with emission collected at 510 nm. Ca^{2+} transients were recorded under steady-state conditions during continuous rhythmic field stimulation (30-60 bpm) at room temperature.

Table 5. Composition of Tyrode`s solution

Substance	Molar Mass (g/mol)	Concentration (mmol/l)
NaCl	58.44	140
KCl	74.55	4
Glucose	180.16	10
$MgCl_2$	95.22	1
HEPES	238.31	5
$CaCl_2$	1 M	2
Diluted in dH_2O, pH= 7.4		

Sarcoplasmic Ca^{2+} content was assessed by caffeine application (10 mmol/l; Table 6), which induces an opening of RyR2 channels in the SR, releasing all stored Ca^{2+} [140, 141]. Fractional Ca^{2+} release from the SR was calculated by comparing the preceding systolic Ca^{2+} transient with the caffeine-induced transient. SERCA2a (sarcoplasmic reticulum Ca^{2+} ATPase 2a) activity was assessed by calculating the difference between the decay kinetics of systolic and caffeine-induced Ca^{2+} transients (K_{sys}-K_{caff}). Ca^{2+} transients were analyzed using IonWizard software (IonOptix Corp.) [142].

Table 6. Composition of caffeine solution

Substance	Molar Mass (g/mol)	Concentration (mmol/l)
Caffeine	194.19	10
NaCl	58.44	140
KCl	74.55	4
Glucose	180.16	10
$MgCl_2$	95.22	1
HEPES	238.31	5
$CaCl_2$	1 M	2
Diluted in dH_2O, pH= 7.4		

3.8 Immunostaining

3.8.1 CD68 staining

After 10 days of Csf1Ri-treatment, human LV tissue slices were paraffin-embedded, sectioned at 4 µm and mounted on glass slides. After a drying period, sections were incubated at 70°C for 40 min to remove paraffin, followed by deparaffinization in xylene (2 x 10 min) and rehydration through a descending ethanol series (100%, 96%, 70%; 2 × 5 min each). Antigen retrieval was achieved by boiling slides at 121°C for 30 s in a combined citrate and T-EDTA buffer (HIER Citrate Buffer pH 6.0, HIER T-EDTA Buffer pH 9.0, Zytomed Systems) diluted in dH_2O. Subsequent steps were conducted at room temperature in a humid chamber, with PBS washes (2 x 5 min) between steps. Following antigen retrieval, slides were incubated in 0.1 M TRIS-Glycine buffer (pH 7.4) for 15 min and consequently blocked with 5% BSA in PBS containing 0.5% Triton X-100 and 0.1% Tween 20 for 60 min to prevent non-specific binding. Primary antibody rabbit anti-human CD68 (1:100, ThermoFisher) was diluted in 1% BSA PBS with 0.5% Triton X-100 and 0.1% Tween 20 and incubated overnight at 4 °C. Negative controls received antibody diluent only. The following day, slides were incubated with the secondary antibody Alexa Fluor 568 goat anti-rabbit IgG (1:500, Life Technologies) for 60 min. All following steps were performed in the dark to prevent photobleaching. Nuclei were counterstained with Hoechst 33342 (1:50000 in dH_2O) for 2 min and autofluorescence was reduced using the Vector TrueVIEW Autofluorescence Quenching Kit (Invitrogen, R37630). Lastly, slides were mounted with Roti Mount-FluorCare (Carl ROTH, HP19.1) and analyzed via fluorescence microscopy the next day.

Images were acquired with the fluorescence microscope Observer.Z1 (Carl Zeiss AG, Oberkochen) utilizing the AxioCam Software (Carl Zeiss AG, Oberkochen). Image analyzation including cell counting and quantitative analysis was performed with ImageJ. CD68 macrophages were identified based on their Alexa Fluor 568 signal in close association with Hoechst-stained nuclei. All evaluations were carried out in a blinded manner to avoid observer bias.

3.8.2 TUNEL staining

Apoptosis of cardiomyocytes was assessed by TUNEL staining using the DeadEnd™ Fluorometric TUNEL System kit (G3250, Promega). All incubation steps were completed at room temperature in a humid chamber unless otherwise indicated, with PBS washes (2 x 5 min) between steps. Sections were deparaffinized in xylene (2 × 10 min), rehydrated through a graded ethanol series (100% for 3 and 5 min, 96% for 2 × 3 min, 50% for 3 min) and incubated for 5 min each in 0.9% NaCl and 4% formaldehyde. Antigen retrieval was performed with Proteinase K (1:500 in PBS, Promega, V302A) for 15 min, followed by fixation in 4% formaldehyde for 5 min. Slides were then incubated with Equilibration Buffer (Promega, G327C) for 10 min, followed by incubation with Reaction Mix (45 µl Equilibration Buffer, 5 µl Nucleotide Mix, 1 µl Terminal Deoxynucleotidyl Transferase, Promega) at 37°C for 60 min. For the positive control, one section was pretreated with RDD buffer (Qiagen, 1010397) for 5 min, followed by 10 min DNase I treatment (10 µl DNase I, RNase-free + 70 µl RDD buffer, Qiagen). For the negative control, TdT enzyme was substituted with RNase-free water (Qiagen, 129112). Following a 15 min incubation in diluted 20x SSC buffer (1:10 in PBS, Promega, G329A), nuclei of tissue sections were counterstained with Hoechst 33342 (1:50000 in Millipore water, Molecular Probes) for 2 min. Slides were then mounted with Roti Mount-FluorCare (Carl Roth, HP19.1) and examined by fluorescence microscopy. Images were acquired with the fluorescence microscope Observer.Z1 (Carl Zeiss AG, Oberkochen) utilizing the AxioCam Software (Carl Zeiss AG, Oberkochen). Apoptosis rates were calculated as TUNEL positive nuclei/Hoechst-stained nuclei × 100%. To differentiate cardiomyocytes nuclei from those of other cell types, cardiomyocyte structure was simultaneously recorded in bright-field mode.

3.9 High-resolution respirometry

3.9.1 Principle of high-resolution respirometry

Oxidative phosphorylation is a crucial process in cellular bioenergetics and represents an important parameter when analyzing mitochondrial respiration in health and disease. Real-time oxidative phosphorylation (OXPHOS) analysis uses respirometry

as a central approach to study oxygen consumption, therefore representing a suitable method to evaluate mitochondrial function.

The measurement of OXPHOS with an Oroboros-O2k oxygraph relies on high-resolution respirometry in a closed chamber, where mitochondrial respiration is quantified by monitoring changes in oxygen concentration over time. To ensure an accurate assessment of the respiratory function, the system usually maintains oxygen levels above limiting concentrations, ensuring that respiration is not limited by oxygen availability (since oxygen concentration declines over time as a result of respiratory processes). By sequentially adding defined substrates, inhibitors and uncouplers to the sample, distinct respiratory states, such as OXPHOS capacity and electron transfer system (ETS) capacity can be characterized. Mitochondrial respiration is thereby calculated as the negative time derivative of the oxygen concentration recorded in the closed chamber over time [143, 144].

3.9.2 Oroboros Set-up

To assess mitochondrial respiration, high-resolution respirometry with an Oroboros-O2k oxygraph (Oroboros Instruments, Innsbruck, Austria) was used. The system consists of two chambers (each 2 mL) that allow parallel measurements under identical experimental conditions. The chambers are equipped with highly sensitive Clark-type oxygen sensors, which continuously monitor oxygen concentration and allow calculation of oxygen flux. To ensure homogeneous distribution of oxygen and added substances, constant stirring is applied within the chambers. The system uses a closed chamber design to minimize external disturbances as well as gas exchanges with the environment. DatLab software (Oroboros Instruments, Innsbruck, Austria) is used for data acquisition and analysis, enabling real-time calculation of the time derivative of oxygen concentration and correction for instrumental background oxygen flux.

3.9.3 Measurement of OXPHOS capacity in human HFrEF tissue slices and iPSC-CM

Human LV tissue slices were permeabilized and prepared for high-resolution respirometry measurements. Respiration was measured at 37 °C in the mitochondrial respiration medium MiR05 (Table 7), using chamber volumes of 2.0 mL. To evaluate oxidative phosphorylation (OXPHOS) capacity and electron transfer system (ETS) capacity, substrate-inhibitor titration (SUIT) protocols were applied [145, 146]. After a stabilization phase, complex I-linked oxidative phosphorylation activity (OXPHOS I) was determined by substitution of malate (2 mM), $MgCl_2$ (5 mM), pyruvate (5 mM), glutamate (10 mM), and ADP (5 mM). Subsequent addition of succinate (10 mM) allowed determination of the capacity of the oxidative phosphorylation system (OXPHOS I+II). To test the integrity of the outer mitochondrial membrane, cytochrome c was applied and consequently electron transport system (ETS) capacity was measured by stepwise uncoupling with FCCP (1.5 µM). Maximal complex II-driven capacity (CII ETS) was assessed in the uncoupled state following inhibition of complex I with rotenone (0.5 µM). Finally, residual oxygen consumption was determined after inhibition of complex III with myxothiazol (0.5 µM) and measured values were subtracted from all respiratory parameters. To prevent oxygen limitation, intermittent re-aerations were performed as required. Respiration rates were normalized to tissue wet weight and tissue slices showing a respiration increase above 10% after cytochrome c addition were considered as damaged and excluded from analysis.

Table 7. Composition of MiR05

Substance	Molar Mass (g/mol)	Concentration (mmol/l)
EGTA	380.35	0.5
$MgCl_2$	95.22	3
Lactobionic acid	358.29	60
Taurine	125.14	20
KH_2PO_4	136.09	10
HEPES	238.31	20
Sucrose	342.30	110
BSA (fatty acid free)	66.50	0.0015
pH= 7.1		

3.10 Transmission electron microscopy

3.10.1 Basic principle of transmission electron microscopy

The transmission electron microscope (TEM) operates on a principle similar to that of a light microscope, however, instead of light rays it uses a focused high-energy beam of electrons to generate an image of the specimen. Since electrons have much shorter wavelength than visible light (~0.005 nm), TEM achieves far higher resolving power, resulting in an approximately 1,000-fold greater resolution than a conventional light microscope [147]. This enables the TEM to reveal ultrastructural details and visualize internal cell structures at the nanometer scale [148]. Therefore, TEM is a suitable technique to obtain detailed morphological information about cell structures like mitochondria.

In practice, a focused beam of electrons is transmitted through an ultrathin (40-100 nm) specimen where electrons either pass through or are scattered by the sample. Electron transmission thereby takes place under high vacuum conditions and electromagnetic lenses are used to focus the electron beam. The resulting scattered electrons form a highly magnified image on a detector or fluorescent screen. Image contrast arises from variations in electron scattering within the specimen, which are often enhanced by staining with heavy metals [148, 149].

3.10.2 The transmission electron microscope

In this work, a LEO912AB electron microscope (Zeiss, Oberkochen, Germany) operated at 100 kV was used. The microscope is equipped with a LaB_6 (lanthanum hexaboride) cathode, providing a stable, high-brightness electron beam. Electron transmission was performed under high vacuum, with electromagnetic lenses used to focus the beam. Specimens were mounted on a motorized 4-axis goniometer, allowing precise tiling. Images were acquired with a 2k × 2k side-mounted camera, controlled by iTEM software (version 5.2, OSIS, Muenster, Germany).

3.10.3 Recordings of human LV samples

Long-term cultured human LV tissue slices, treated with or without Csf1Ri, were fixed overnight in 0.1 M cacodylate-buffered Karnovsky fixative containing 2.5% glutaraldehyde and 2% paraformaldehyde (Electron Microscopy Sciences, Hatfield, PA, USA) at room temperature. Samples were then post-fixed in 1% osmium tetroxide (Electron Microscopy Sciences) for 2 hours and subsequently dehydrated in graded ethanol (Sigma-Aldrich). After dehydration, samples were embedded in EMbed-812 epoxy resin (Electron Microscopy Sciences). Ultra-thin (80 nm) sections were prepared using a Leica Ultracut-S Microtome (Leica-Reichert, Wetzlar, Germany) and sequentially contrasted with 2% aqueous uranyl-acetate (Honeywell International Inc., Morristown, NJ, USA) and 2%-lead-citrate solutions (Leica) for 10 min each. Subsequently, transmission electron microscopy was performed.

Mitochondria were imaged on both sides of visible Z-lines in cardiomyocytes to ensure that all analyzed mitochondria originated from comparable subcellular regions. Mitochondrial parameters (mitochondria count, mean mitochondrial size/FOV (μm^2), defect mitochondria (%), cristae area/mito area (%) and relative electron density (Mean grey value)) were quantified using ImageJ (version 1.54p, National Institutes of Health, Bethesda, MD, USA). Mitochondria were manually outlined using the freehand selection tool and the area of each mitochondrion was measured in μm^2 (Figure 10a). Mitochondrial health was assessed by classifying mitochondria as healthy, hydropic, or otherwise defective (e.g. lamellar structures, loss of cristae with preserved matrix density) following established criteria [150, 151]. Cristae density was calculated as the ratio of cristae area to total mitochondrial area (%) (Figure 10b). To compare matrix electron density, the inverted mean grey value of mitochondria was analyzed. To account for potential variations in image contrast, the mean gray value of the sarcomeres in each image was quantified and normalized to a reference value. The mean gray value of mitochondria was measured and normalized to the reference value.

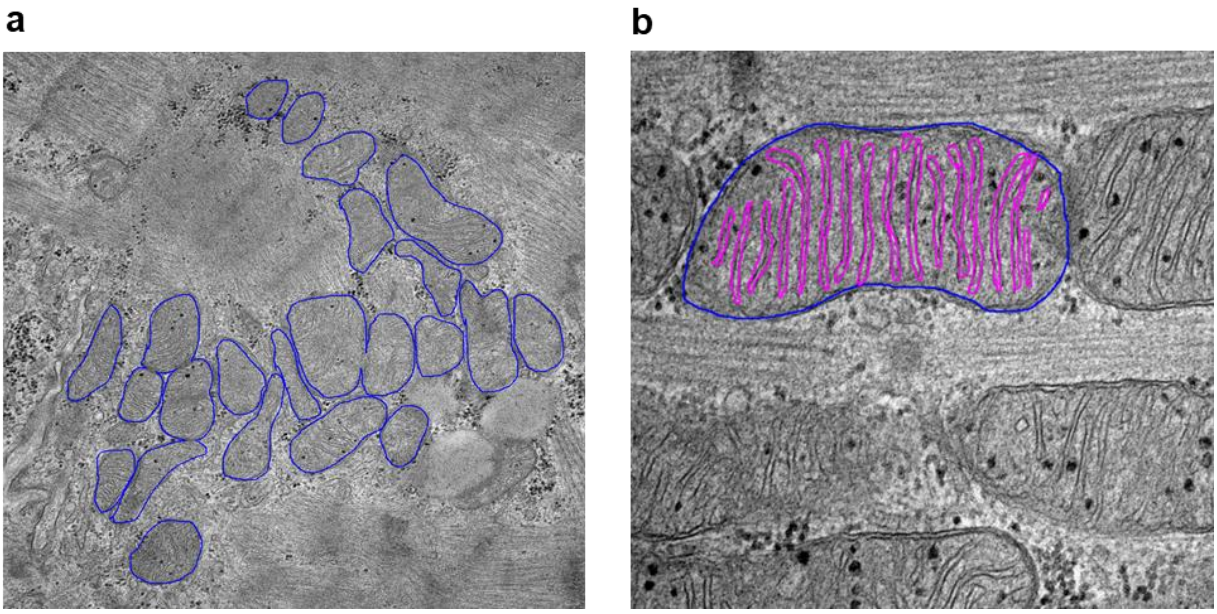

Figure 10. Analyzation of mitochondria in human HFrEF tissue slices. (a) Evaluation of mitochondrial count and mean mitochondrial size/FOV in µm^2 using the freehand selection tool from ImageJ. The perimeter of each mitochondrion is displayed in blue. (b) Analyzation of cristae density by using the ratio of cristae area (perimeter in blue) to total mitochondrial area (violet).

3.11 Determination of hydrogen peroxide production

Hydrogen peroxide production was measured in collected medium of cultured tissue slices after 10 days of Csf1Ri-treatment using the Hydrogen Peroxide/Peroxidase Assay Kit (Thermo Fisher Scientific, A22188) according to the manufacturer´s protocol.

50 µl of each medium sample was transferred to individual wells of a microplate. As a positive control, 50 µl of a 10 µM H_2O_2 working solution (diluted to in 1 x Reaction Buffer) was included. For the negative control, 50 µl of 1x Reaction Buffer was used. An Amplex® Red reagent/HRP working solution (100 µM Amplex® Red reagent and 0.2 U/mL HRP diluted in 1x Reaction Buffer) was prepared. 50 µL of the working solution was added to each microplate well containing the controls and the samples and consequently incubated for 30 minutes at room temperature. Absorption was then measured in a microplate reader at 560 nm and 590 nm wavelength. To correct for background fluorescence, values derived from the negative control were subtracted from measured values from medium samples.

3.12 Enzyme activity assays

To perform enzyme activity assays, cultivated human LV tissue slices were submerged in 400 µl of lysis buffer after 10 days of macrophage-depletion and consequently disrupted using lysing matrix tubes (1169250-CF, MP Biomedicals).

3.12.1 Caspase-3 activity assay

To measure apoptosis in Csf1Ri treated vs. untreated human cultured tissue slices, the Caspase-3 Assay Kit (ab39401, Abcam) was used. Caspases are cysteine proteases that regulate apoptosis. They are synthesized as inactive pro-enzymes and become activated by cleavage in response to apoptotic stimuli. Initiator caspases thereby trigger the apoptotic cascade, while executioner caspases, such as caspase-3, are mediating the proteolysis of cellular substrates, leading to cell death [152].

The Caspase-3 activity assay relies on spectrophotometric detection of the chromophore p-nitroaniline (p-NA), which is released upon cleavage of the labeled substrate DEVD-pNA. The absorbance of p-NA can be measured at 400 nm using a microplate reader. Caspase-3 activity is thereby determined by comparing p-NA absorbance in between a treated and untreated group to calculate the fold increase [153].

Lysed human tissue slices were re-suspended in 50 µL of chilled Lysis Buffer IV, incubated on ice for 10 min and subsequently centrifuged at 10,000 x g for 1 min. The supernatant was transferred to a fresh tube and immediately placed on ice. A BCA assay (Thermo Fisher, YJ374058) was conducted to evaluate the protein concentration of each sample and final concentrations were adjusted to 200 µg protein per 50 µL Lysis Buffer IV. For caspase-3 detection, 50 µL of each sample was placed into a microplate well. As a negative control, 50µL 2x Reaction Buffer I was used. In a next step, 50 µL of a Caspase Reaction Mix (2x Reaction Buffer I with DTT I, 1:100) was added to each sample, followed by the addition of 5 µL of 4 mM DEVD-pNA (200 µM final concentration). All reagents were carefully mixed and incubated for 100 min at 37°C. Caspase-3 activity was measured at 400 nm using a microplate reader.

3.12.2 Complex IV human enzyme activity assay

The mitochondrial respiratory chain consists of different complexes that facilitate oxidative phosphorylation, a process crucial for ATP synthesis in cardiomyocytes. Complex IV, also known as cytochrome c oxidase, represents a crucial component of the mitochondrial respiratory chain and its activity provides insights into cellular function following experimental intervention [154].

Mitochondrial enzyme activity of complex IV in treated versus untreated human cultured tissue slices was measured with the Complex IV Human Enzyme Activity Microplate Assay Kit (ab109909, Abcam), following the manufacturer's instructions. The principle of the assay relies on the colorimetric detection of CIV activity by monitoring the oxidation of reduced cytochrome c, measured as a decrease in absorbance at 550 nm.

Lysed human tissue slices were centrifuged at 10,000 x g for 1 min and supernatant was transferred to a clean tube. Sample protein concentration was determined by a BCA protein assay kit (Thermo Fisher, YJ374058) and adjusted to a final sample protein concentration of 5.0 mg/mL. 10X Detergent solution in a final dilution of 1/10 was added and incubated on ice for 30 min to allow solubilization. Subsequently, samples were centrifuged for 20 minutes at 4°C at 12,000 x g and supernatant was collected and transferred to a clean tube. For complex IV detection, 200 µl of each sample was added to an 8-well strip coated with an anti-Complex IV monoclonal antibody provided with the kit. As background control, 200 µl of the used diluent was added. In a next step, the samples were incubated for 3 hours at room temperature. Once the monoclonal antibody has captured the CIV enzymes in the well, substrate (Reagent C) was added, and enzymatic activity was assessed by measuring the change in absorbance over time in a microplate reader.

3.13 Human induced pluripotent stem cell cardiomyocytes (iPSC-CM)

3.13.1 Obtaining of human iPSC-CM

IPSC-CM were received through a collaboration with the working group Streckfuß-Bömeke from Würzburg that established the differentiation of human iPSCs into cardiomyocytes as described before [155]. IPSC-CM were obtained from healthy donors without known cardiovascular disease. Prior consent was obtained from all donors. Differentiated ventricular cardiomyocytes were sent to the University Hospital Regensburg and consequently placed in cell culture. Experiments with iPSC-CM began approximately 90 days after the start of differentiation.

3.13.2 Long-term cultivation and macrophage depletion in human iPSC-CM

Following differentiation, human ventricular iPSC-CMs were enzymatically dissociated using trypsin. The digestion was terminated by the addition of digestion medium (RPMI1640 (Gibco, 72400-021) supplemented with 2% B27 (Gibco, 17504-044), 20% FBS (Gibco, A3160802) and 0.13% Thiazovivin (Merck, 420220-10MG)), and the cell suspension was centrifuged at 200 × g for 5 minutes at room temperature. After centrifugation, the supernatant was carefully removed, and the cell pellet was resuspended in digestion medium. Viable cells were counted using a Neubauer hemocytometer and seeded at a density of 250,000 cells per well in Matrigel-coated 6-well plates. After 48 hours, digestion medium was replaced with culture medium (RPMI1640 (Gibco, 72400-021) supplemented with 2% B27 (Gibco, 17504-044)), which was subsequently refreshed every two days.

Following a 5-day resting period, iPSC-CM were treated with 25 µM Colony-stimulating factor 1 receptor (Csf1R) inhibitor PLX-5622 (HY-114153, MedChemExpress) for 10 days. Morphology of treated vs. untreated iPSC-CM was assessed objectively using a standard light microscope (Leica DM IL, Wetzlar). OXPHOS measurements were performed with the Oroboros system (Oroboros Instruments, Innsbruck, Austria) to detect potential functional differences in macrophage-deplete iPSCs compared to vehicle control.

3.14 Statistics

Statistical analysis of the data was conducted using GraphPad Prism version 10.4.1 (GraphPad Software, San Diego, CA, USA). All experimental data are presented as mean ± standard error of the mean (SEM). Normal distribution was tested with the Shapiro-Wilk test if appropriate. Comparisons between two groups were performed using paired or unpaired student t-tests for normally distributed data and paired or unpaired Mann-Whitney tests for non-normal distributed data. Datasets with two or more groups and/or time points were analyzed using 1 or 2-way ANOVA. Multiple comparisons were corrected by the Šídák method. The results were considered significant if P was < 0.05. Data were analyzed in a blinded manner whenever applicable.

4 Results

4.1 Patient characteristics

HF was caused by either dilated cardiomyopathy (DCM, 50%) or ischemic cardiomyopathy (ICM, 50%). Patients were 75% male, with a mean age of 52.3 ± 4.4 years, a mean echocardiographic ejection fraction (EF) of 20.8 ± 1.8%, and a mean heart rate of 75.6 ± 3.3 beats per minute (bpm). Detailed clinical characteristics are provided in Table 8.

Table 8. Characteristics of patients

Characteristics (n=12 patients)	
Male sex, %	75.0
Age, y (mean±SD)	52.3±4.4
White origin, %	100
DCM, %	50
Heart rate, bpm (mean±SD)	75.6±3.3
AF %	41.7
Diabetes, %	16.6
Coronary artery disease, %	50.0
Ejection fraction, % (mean±SD)	20.8±1.8
IVS, mm (mean±SD)	8.7±0.9
LVEDD, mm (mean±SD)	63.3±2.8
ACE inhibitor or ARB, %	66.7
β-blocker, %	66.7
Aldosterone antagonist, %	75.0
Diuretic, %	75.0
Statins, %	58.3

4.2 Macrophage depletion impairs myocardial contractile function

4.2.1 Csf1Ri treatment leads to reduction of CD68$^+$ macrophages

To assess macrophage depletion, long-term cultured human HFrEF tissue slices treated with or without Csf1Ri were paraffin-embedded and stained for CD68, a universal marker for macrophages (Figure 11). Following 10 days of treatment, an effective reduction of CD68$^+$ cells could be observed in Csf1Ri-treated tissue slices (4.85 ± 0.83 cells/FOV; n= 5 slices/3 hearts) compared to vehicle control (7.98 ± 0.44 cells/FOV; n= 5 slices/3 hearts), confirming the effectiveness of macrophage depletion via the Csf1Ri PLX-5622 (Figure 12).

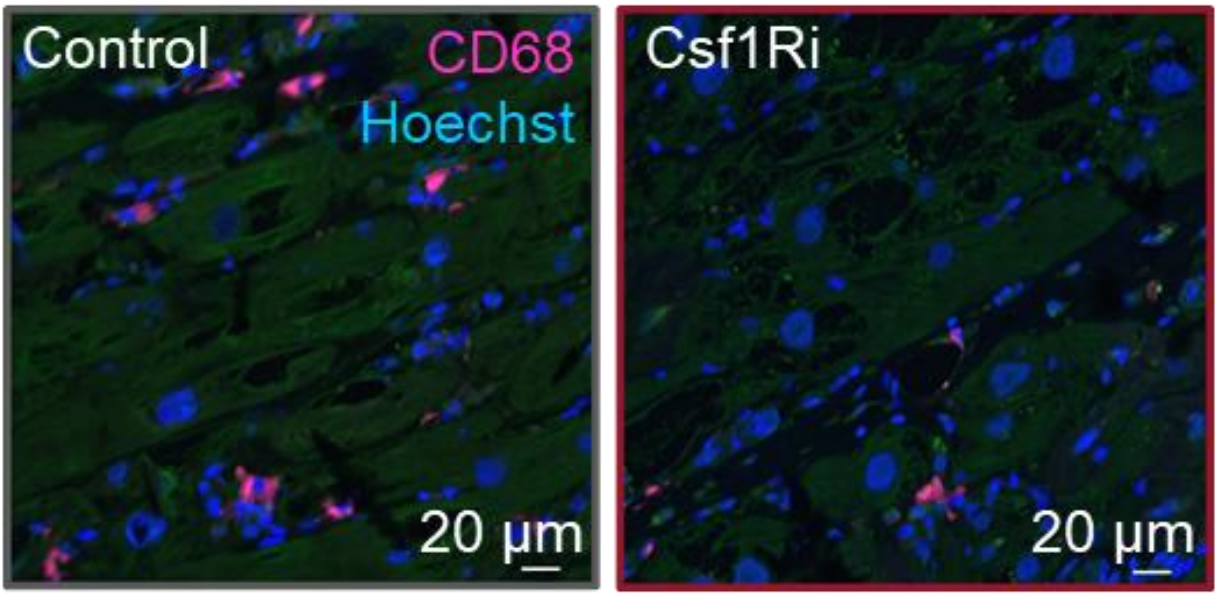

Figure 11. CD68-stained macrophages in human HFrEF tissue slices. Representative images of CD68-stained macrophages (magenta) and nuclei (blue) stained in human HFrEF tissue slices. Tissues were treated with vehicle (Control, left) or a CSF1R inhibitor (Csf1Ri, right). Scale bar: 20 µm.

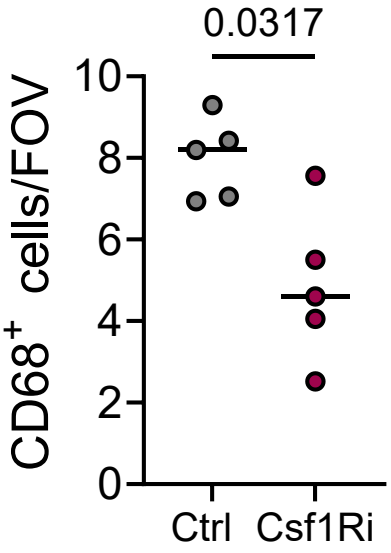

Figure 12. Evaluation of macrophage depletion via CD68 staining. Quantification of CD68-positive macrophages in human tissue slices after Csf1Ri-treatment (n= 5 slices/3 hearts) compared to vehicle control (n= 5 slices/3 hearts). Data represent the mean number of macrophages per field of view (10 FOVs/slice). Statistical significance was determined using the Mann-Whitney-U test.

4.2.2 Reduction of systolic force amplitude in macrophage-depleted human tissue slices

To investigate the effect of macrophage depletion in human HFrEF myocardium, cardiac tissue slices were long-term cultured in vitro and treated with the Csf1Ri PLX-5622 for 10 days. During Csf1Ri-treatment, contractility was assessed daily (Figure 13). All measured values were normalized to their respective baseline measurements obtained prior to macrophage depletion and normalized to paired vehicle control.

Contractile function analysis of human HFrEF myocardium demonstrated a significant decrease in systolic force in macrophage-depleted tissue slices (n= 34 slices/8 hearts) compared to vehicle control (n= 35 slices/8 hearts), with reductions of 40.0 ± 6.09% on day five and 35.04 ± 6.94% on day 10 of Csf1Ri treatment (Figure 14).

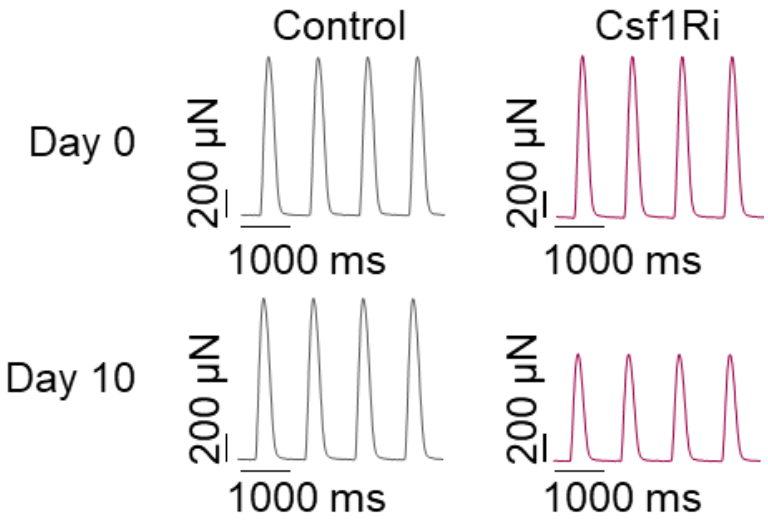

Figure 13. Original traces of contractile force in human HFrEF tissue slices. Original traces of contractile force of human HFrEF tissue slices on day 0 and day 10 of Csf1Ri treatment versus control.

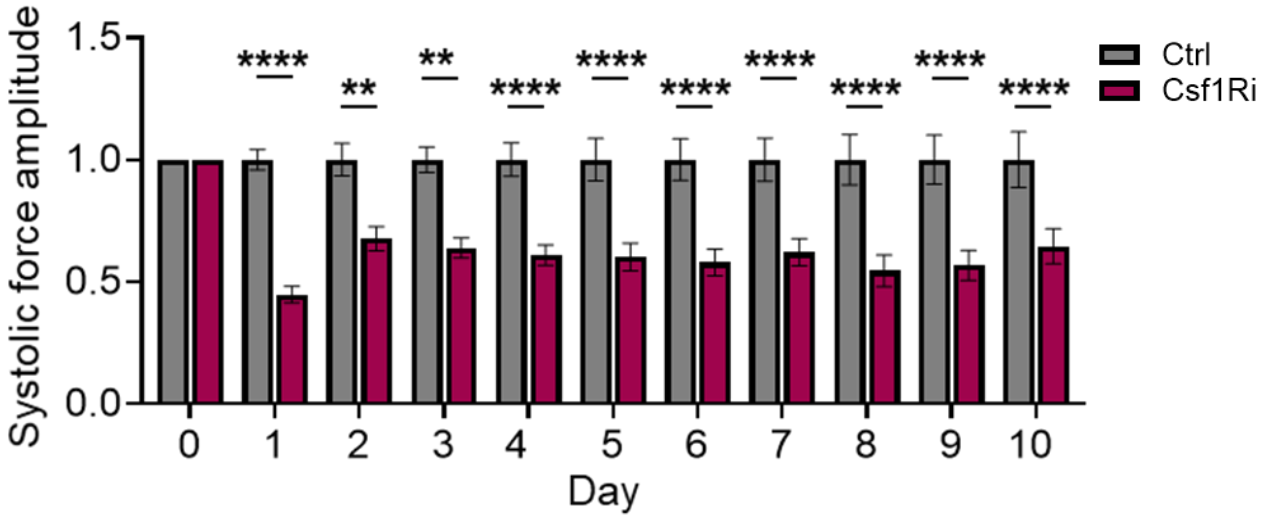

Figure 14. Contractility assessment of human HFrEF tissue slices treated with Csf1Ri. Cardiac contractility of human HFrEF tissue slices during long-term culturing with Csf1Ri treatment (n= 34 slices/8 hearts) compared to vehicle control (n= 35 slices/8 hearts). Data are represented as mean systolic force amplitude while error bars display the standard error of the mean (SEM). All measured values were normalized to their respective baseline measurements obtained prior to macrophage depletion and to the corresponding vehicle control. Statistical significance was evaluated using 2-way ANOVA. Not all time points could be obtained for every preparation.

4.2.3 Altered relaxation and contraction dynamics in macrophage-depleted human HFrEF tissue

Additional contractile parameters were analyzed to assess the effect of macrophage depletion in human HFrEF tissue slices. While baseline values, representing the diastolic tension of the heart, and RT80 values, describing the relaxation time at 80%, did not change between both groups (Figure 15-16), time to peak (TTP) values were significantly increased in macrophage-depleted tissue slices (n= 35 slices/8 hearts) on day one (42.4 ± 12.6%) and three (28.8 ± 13.3%) but not on day 10, making the relation to macrophage depletion less clear (Figure 17). Time to peak was defined as the interval from the onset of contraction to the maximum twitch amplitude and is determined by Ca^{2+}-induced Ca^{2+} release.

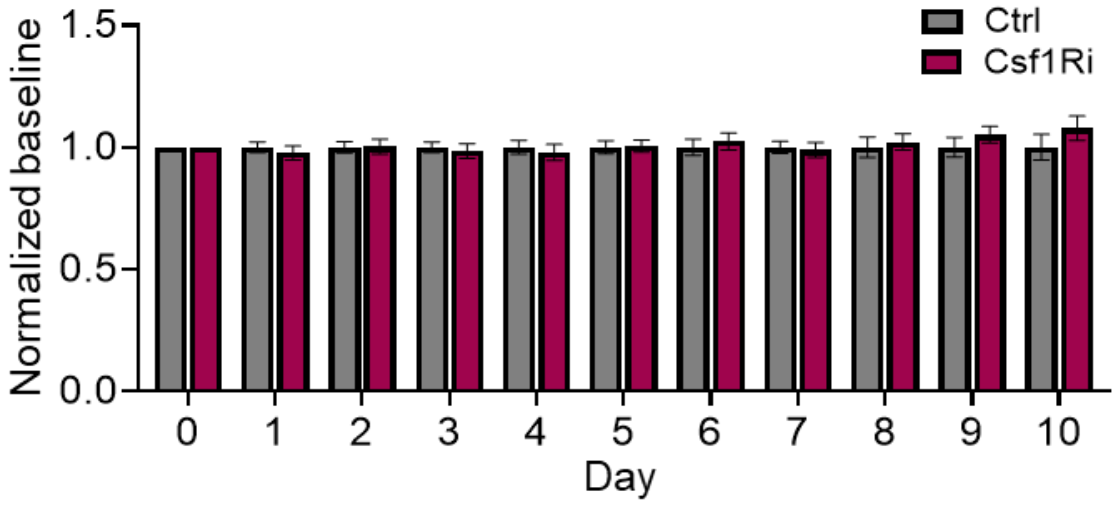

Figure 15. Diastolic tension of human HFrEF slices treated with Csf1Ri. Diastolic tension of tissue slices during long-term culturing with Csf1Ri treatment (n= 34 slices/8 hearts) compared to vehicle control (n= 35 slices/8 hearts). Data are represented as mean systolic force amplitude while error bars display the standard error of the mean (SEM). All measured values were normalized to their respective baseline measurements obtained prior to macrophage depletion and to the corresponding vehicle control. Statistical significance was evaluated using 2-way ANOVA. Not all time points could be obtained for every preparation.

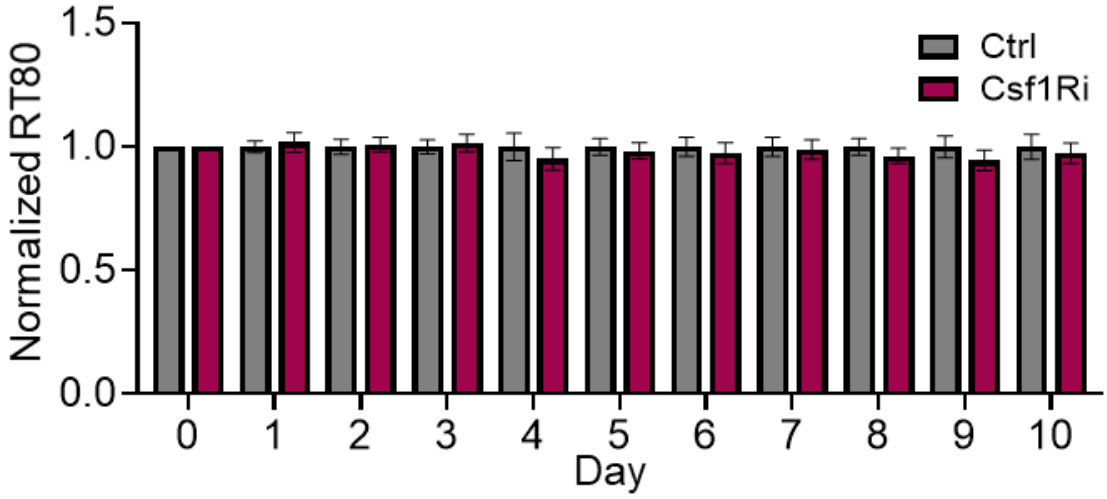

Figure 16. RT80 in human HFrEF tissue slices treated with Csf1Ri. Relaxation time at 80% (RT80) of tissue slices during long-term culturing with Csf1Ri treatment (n= 34 slices/8 hearts) compared to vehicle control (n= 35 slices/8 hearts). Data are represented as mean systolic force amplitude while error bars display the standard error of the mean (SEM). All measured values were normalized to their respective baseline measurements obtained prior to macrophage depletion and to the corresponding vehicle control. Statistical significance was evaluated using 2-way ANOVA. Not all time points could be obtained for every preparation.

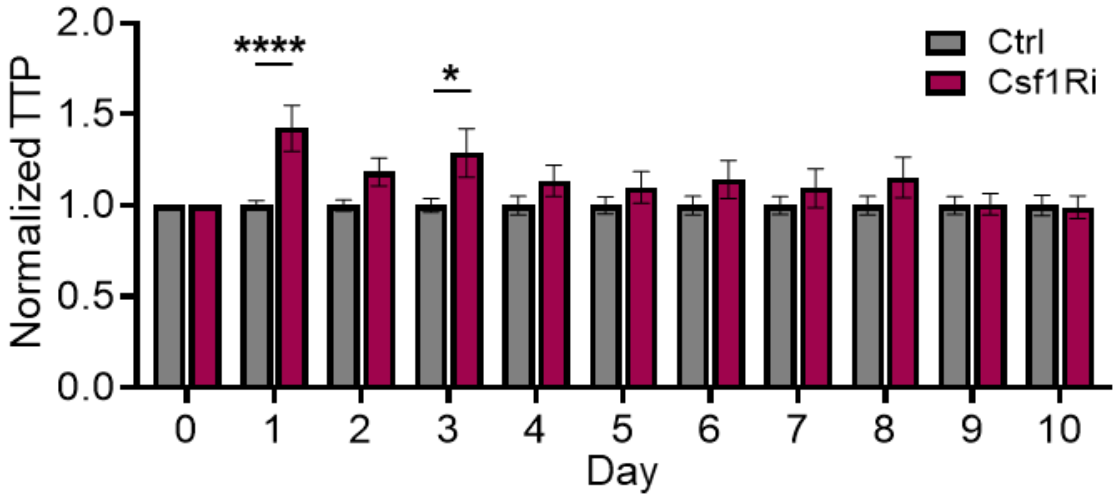

Figure 17. TTP in human HFrEF tissue slices treated with Csf1Ri. Time to peak (TTP) values of tissue slices during long-term culturing with Csf1Ri treatment (n= 34 slices/8 hearts) compared to vehicle control (n= 35 slices/8 hearts). Data are represented as mean systolic force amplitude while error bars display the standard error of the mean (SEM). All measured values were normalized to their respective baseline measurements obtained prior to macrophage depletion and to the corresponding vehicle control. Statistical significance was evaluated using 2-way ANOVA. Not all time points could be obtained for every preparation.

4.2.4 Force–frequency relationship after Csf1Ri treatment in human HFrEF tissue

The force-frequency relationship reflects the intrinsic ability of the heart to enhance myocardial contractility and isometric force in response to increasing heart rates. However, in failing hearts, this positive force-frequency response, characterized by frequency-dependent potentiation of contractile force, is absent [32].

To experimentally investigate if macrophage depletion in human HFrEF tissue slices leads to different force-frequency properties compared to vehicle control slices, a force-frequency-stimulation protocol was applied on day 0, 5 and 10 . While all human HFrEF tissue slices displayed the typical negative force-frequency relationship observed in failing hearts, no differences could be observed between Csf1Ri-treated slices (n= 21 slices/8 hearts) and vehicle control (n= 18 slices/8 hearts) (Figure 19).

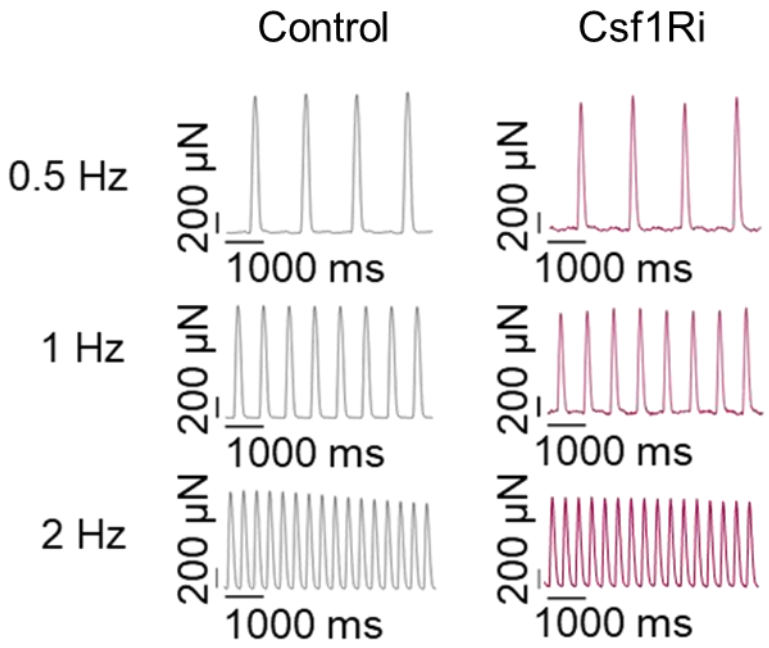

Figure 18. Original traces of FFR measurements in human HFrEF tissue slices. Original traces of human HFrEF tissue slices stimulated with increasing frequencies (0.5 Hz, 1 Hz and 2 Hz) on day 10 of Csf1Ri treatment.

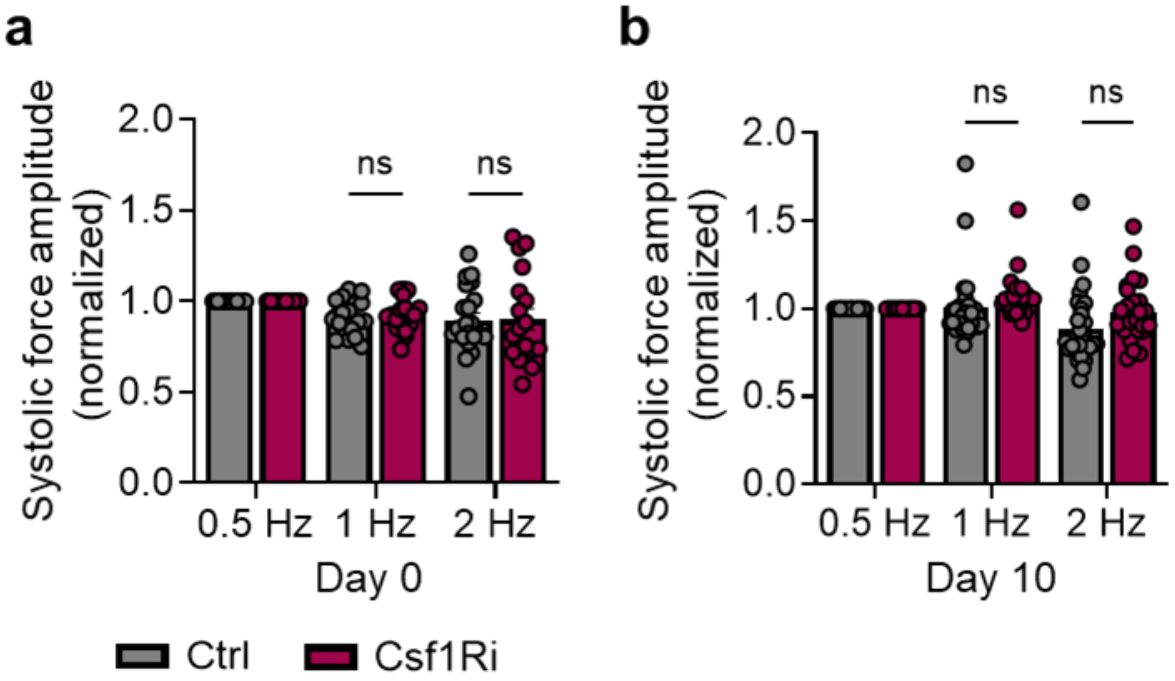

Figure 19. Force-frequency-relationship in Csf1Ri-treated human HFrEF tissue slices. Cardiac contractility of human HFrEF tissue slices during long-term culturing at stimulation frequencies of 0.5 Hz, 1 Hz and 2 Hz on (a) day 0 and (b) day 10 of Csf1Ri treatment (n= 21 slices/8 hearts) compared to vehicle control (n= 18 slices/8 hearts). Data are represented as mean systolic force amplitude while error bars display the standard error of the mean (SEM). Statistical significance was evaluated using 2-way ANOVA. Not all time points could be obtained for every preparation.

4.2.5 Impaired post-rest potentiation indicates reduced SR Ca^{2+} content after Csf1Ri treatment

Post-rest potentiation provides an indirect assessment of the SR capacity for Ca^{2+} storage and release, thereby reflecting the contractile properties of human myocardium. In healthy hearts, a rest period is followed by an enhanced force of contraction, while damaged hearts show impaired SR Ca^{2+} handling properties with disturbed post-rest responses and attenuated contractile force.

To investigate if macrophage depletion in human HFrEF tissue slices leads to different post-rest-potentiation properties compared to vehicle control slices, a post-rest-potentiation protocol was applied (Figure 20, original traces). To quantify the post-rest potentiation, the ratio of amplitudes of the first twitch after a 10- and 30-second rest interval to the last twitch before the rest interval was assessed. PRP after a 10-second stimulation pause as well as after a 30-second pause showed a diminished ratio of

amplitudes in macrophage-depleted human HFrEF tissue slices (n= 23 slices/8 hearts) at both day 5 (10 seconds: 10.6 ± 3.3%; 30 seconds: 22.2 ± 5.8%) and day 10 (10 seconds: 8.1 ± 2.2%; 30 seconds: 16.9 ± 4.2%) compared to vehicle control (n= 24 slices/8 hearts), suggesting diminished SR Ca^{2+} content in macrophage-depleted myocardium (Figure 21).

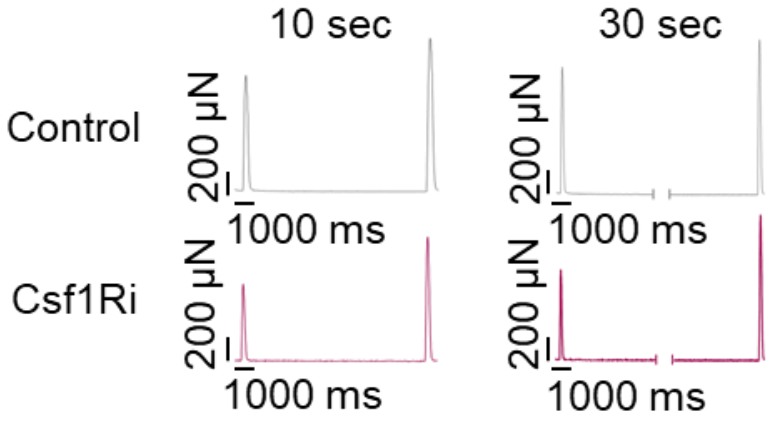

Figure 20. Original traces of PRP measurements in human HFrEF tissue slices. Original traces of human HFrEF tissue slices at 10- and 30-second post-rest conditions on day 10 of Csf1Ri treatment.

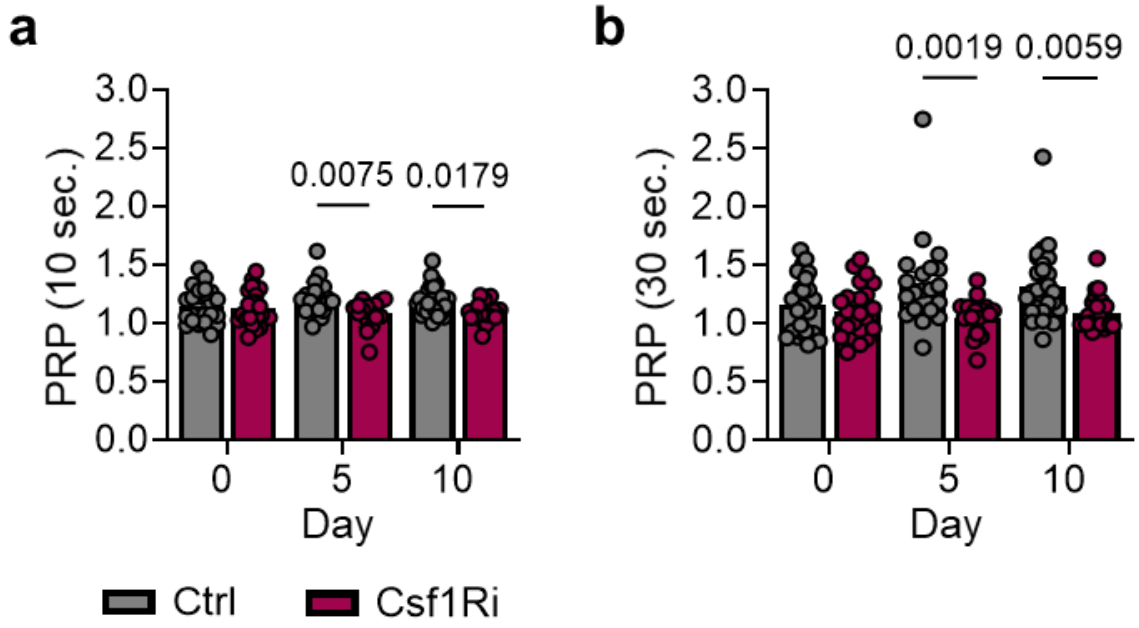

Figure 21. Post-rest potentiation in Csf1Ri-treated human HFrEF tissue slices. Cardiac contractility measured under PRP conditions with a (a) 10- and (b) 30-second stimulation pause on day 0, 5 and 10 of Csf1Ri treatment (n= 23 slices/8 hearts) compared to vehicle control (n= 24 slices/8 hearts). Data represent ratios of force amplitudes while error bars display the standard error of the mean (SEM). Statistical significance was evaluated using 2-way ANOVA. Not all time points could be obtained for every preparation.

4.2.6 Macrophage depletion leads to altered intracellular Ca^{2+} -cycling in isolated human cardiomyocytes

Impaired contractile function is often driven by dysfunctional Ca^{2+} handling within cardiomyocytes. Since diminished systolic force amplitude could be observed in Csf1Ri-treated human HFrEF tissue slices, dysfunctional Ca^{2+} handling could be an underlying cause for the observed contractile dysfunction.

To assess, if Ca^{2+} handling was altered due to macrophage depletion, human HFrEF tissue slices were isolated after 5 days of Csf1Ri treatment and consequently analyzed via epifluorescence microscopy (Figure 22, original traces). Of note, after 5 days of macrophage depletion impaired contractility was already present. Isolated cells of Csf1Ri-treated tissue slices (n= 74 cells/5 hearts; 0.053 ± 0.005 $F_{340/380}$) showed a significant reduction in Ca^{2+} transient amplitude compared to vehicle control (n= 58 cells/5 hearts; 0.091 ± 0.01 $F_{340/380}$) (Figure 23a). Other parameters, such as diastolic Ca^{2+}, time to peak at 80% (TTP80) and relaxation time at 80% (RT80) remained unchanged (Figure 23b-d).

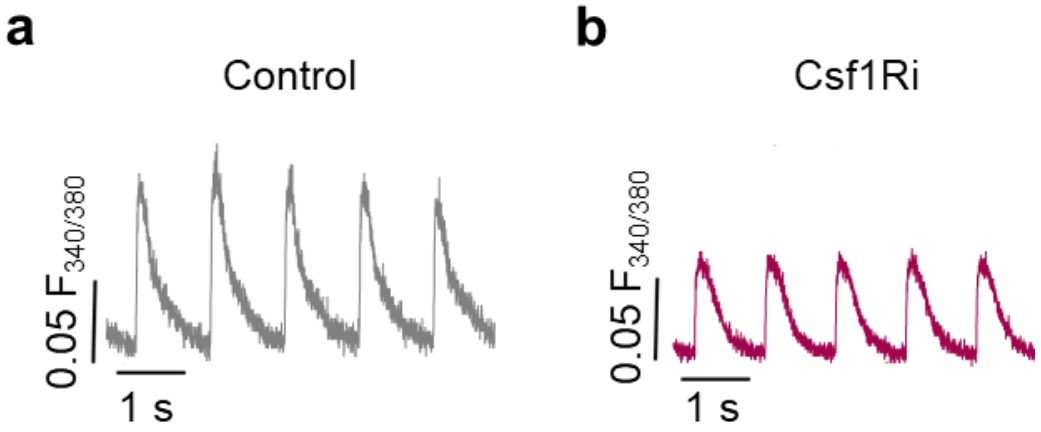

Figure 22. Original traces of intracellular Ca^{2+} measurements in isolated human HFrEF tissue slices. Long-term cultured HFrEF human tissue slices treated with or without Csf1Ri were isolated and consequently measured via epifluorescence microscopy (60 bpm, 20 V, 2 ms). Original traces of (a) control versus (b) Csf1Ri-treated group.

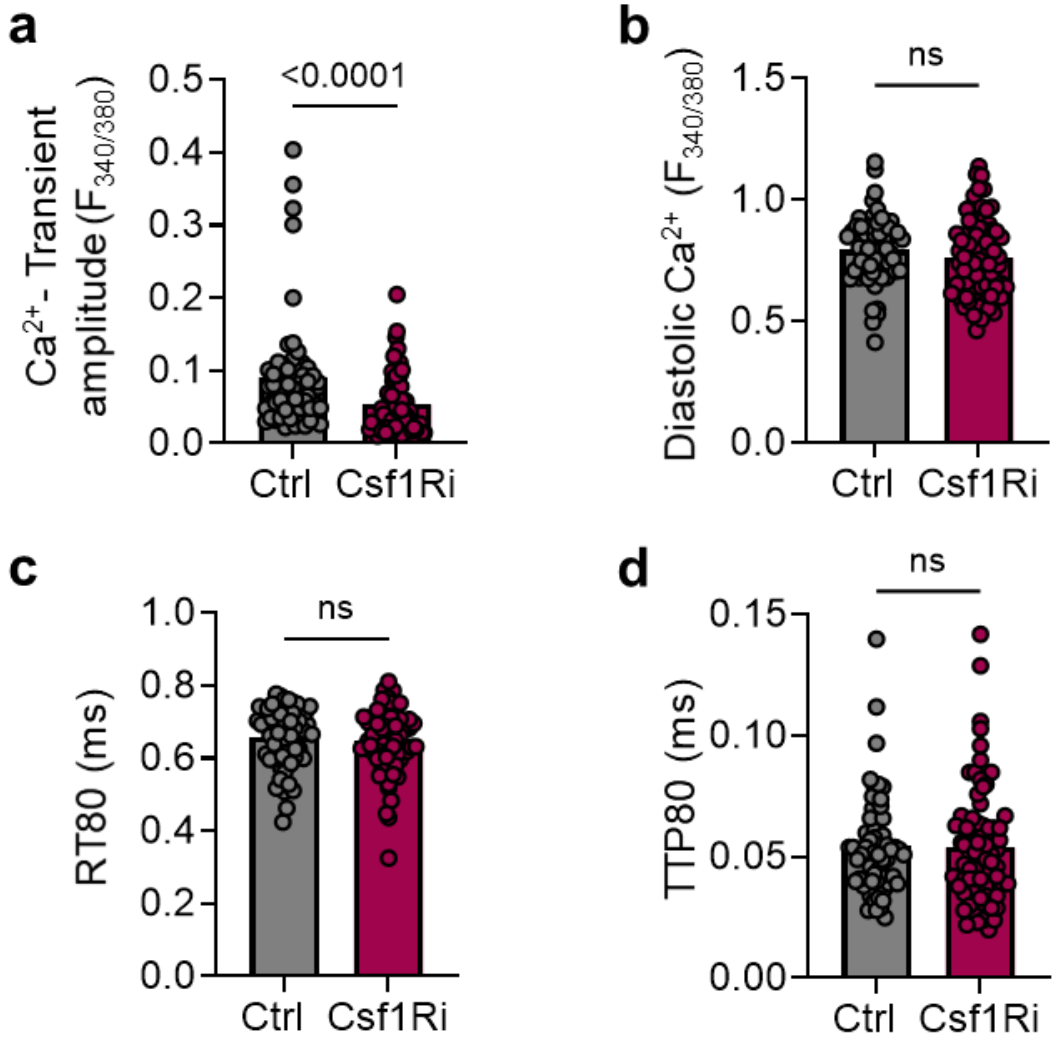

Figure 23. Ca^{2+} homeostasis in Csf1Ri-treated human HFrEF tissue slices. Epifluorescence measurements of isolated cells from long-term cultured human HFrEF tissue slices treated with Csf1Ri (n= 74 cells/5 hearts) compared to vehicle control (n= 58 cells/5 hearts). (a) Ca^{2+}-transient amplitude, (b) diastolic Ca^{2+}, (c) relaxation time at 80% (RT80) and (d) time to peak at 80% (TTP80) of both groups were assessed. Error bars display the standard error of the mean (SEM). Statistical significance was evaluated using the Mann-Whitney U test.

As PRP indicated SR Ca^{2+} content after macrophage depletion and Ca^{2+} transient amplitude was reduced in macrophage-depleted HFrEF myocardium, assessments of SR Ca^{2+} were conducted. To do so, caffeine-induced Ca^{2+} release was evaluated after caffeine application in macrophage-depleted human HFrEF tissue slices compared to vehicle controls (Figure 24, original traces). Macrophage depletion showed significantly reduced SR Ca^{2+} content (n=35 cells/4 hearts; 0.472 ± 0.061 $F_{340/380}$) compared to vehicle control (n=30 cells/4 hearts; 0.640 ± 0.043 $F_{340/380}$) (Figure 25a). The ratio of basal transient amplitudes to caffeine transient amplitudes also showed a

significant reduction in macrophage-depleted tissue slices (n=35 cells/4 hearts; 0.360 ± 0.054 $F_{340/380}$) compared to vehicle control (n=30 cells/4 hearts; 0.502 ± 0.051 $F_{340/380}$) (Figure 25b).

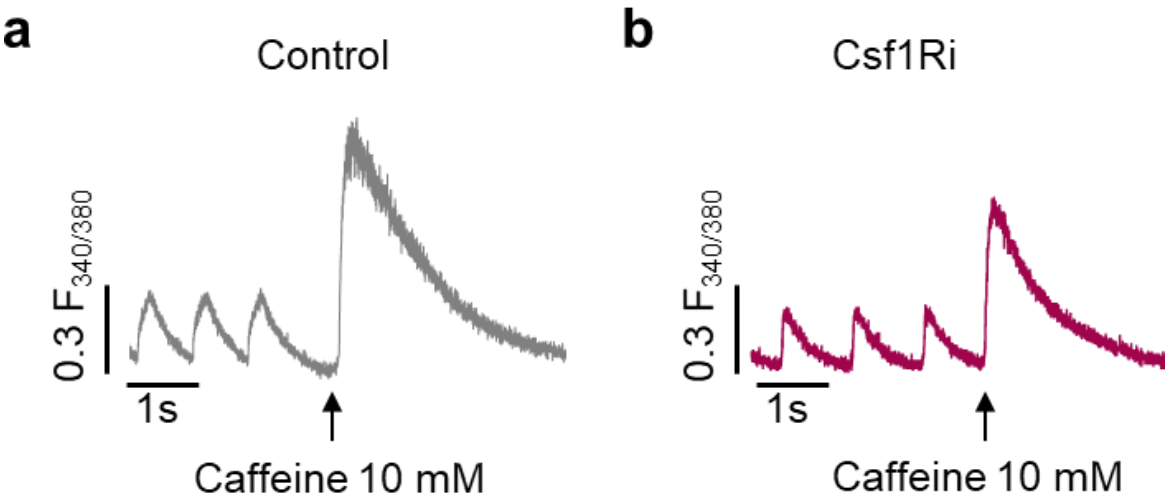

Figure 24. Original traces of caffeine-induced Ca^{2+} transients in isolated human HFrEF tissue slices. Caffeine-induced Ca^{2+} transient amplitudes (10 mM caffeine, epifluorescence measurements with Fura-2) from (a) vehicle control and (b) Csf1Ri-treated isolated human tissue slices on day 5 of Csf1Ri treatment.

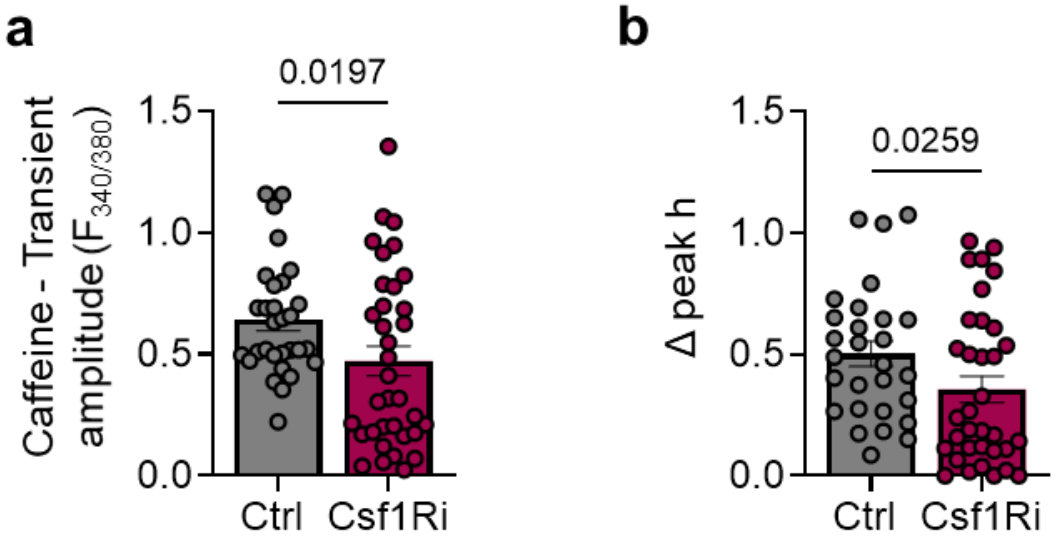

Figure 25. Caffeine-induced Ca^{2+} transients in Csf1Ri-treated human HFrEF tissue slices. Caffeine-induced Ca^{2+} transients (10 mM caffeine, Fura-2 epifluorescence microscopy) in Csf1Ri-treated human HFrEF tissue slices (n=35 cells/4 hearts) versus vehicle control (n=30 cells/4 hearts) after 5 days. Mean values of (a) caffeine transient amplitude (an indicator of SR Ca^{2+} load) and (b) peak high (ratio of basal transient amplitude and caffeine transient amplitude). Error bars display the standard error of the mean (SEM). Statistical significance was evaluated using two-sided unpaired t-tests.

4.3 Macrophage loss increases cardiomyocyte apoptosis and oxidative stress in macrophage-depleted human tissue

To further investigate the mechanisms underlying the observed contractile dysfunction, apoptosis and oxidative stress were analyzed, as both directly impact myocardial function and contractility.

Apoptosis was assessed using a caspase-3 activity assay, which revealed a significant increase of 38.2 ± 16.7% in total apoptotic cells in macrophage-depleted tissue slices (n= 9 slices/6 hearts) compared to vehicle control (n= 10 slices/6 hearts) (Figure 26).

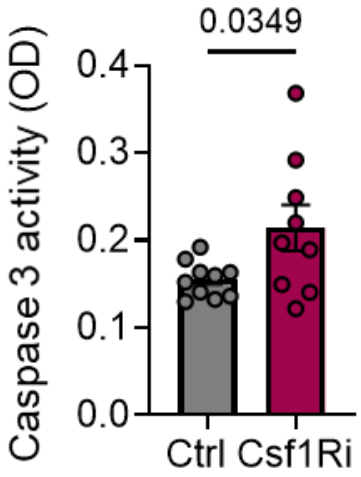

Figure 26. Apoptosis in macrophage-depleted human HFrEF tissue slices. Measurement of caspase-3 enzymatic activity as an indicator of apoptosis in cultured human HFrEF tissue slices treated with Csf1Ri (n= 9 slices/6 hearts) compared with vehicle controls (n= 10 slices/6 hearts) on day 10. Data are shown as mean ± SEM, with individual data points representing single tissue slices. Statistical significance was assessed by two-sided unpaired t-tests.

To specifically determine cardiomyocyte apoptosis, TUNEL staining was subsequently performed. Cardiomyocyte structure was simultaneously captured in bright-field mode to enable distinction of cardiomyocyte nuclei from other cell nuclei present (Figure 27). Hereby, a 2.4-fold increase in TUNEL^{+} cardiomyocytes was detected in Csf1Ri-treated human tissue slices (5 slices/4 hearts) compared to vehicle control (5 slices/4 hearts) (Figure 28).

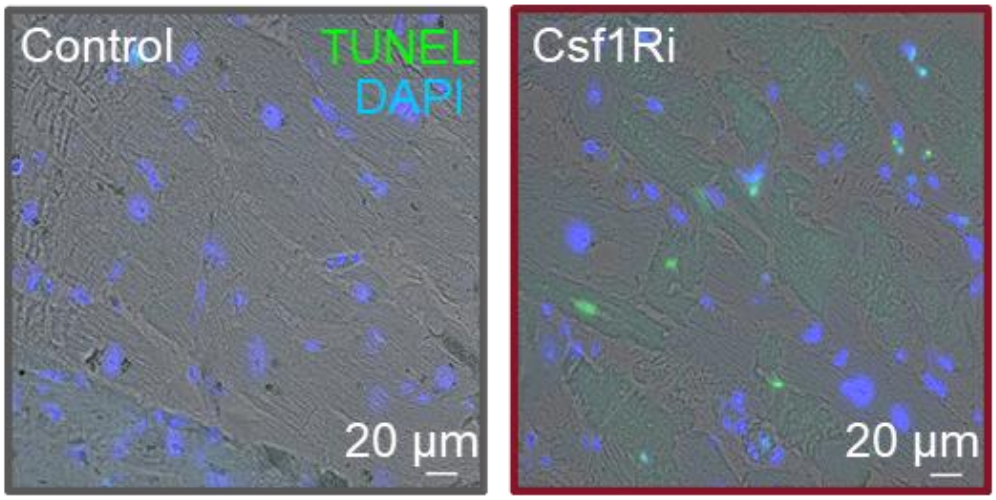

Figure 27. TUNEL staining in human HFrEF tissue slices. Representative TUNEL staining images of macrophage-depleted human HFrEF tissue slices and vehicle control on day 10. Tissues were treated with vehicle (Control, left) or a CSF1R inhibitor (Csf1Ri, right). Nuclei are stained in blue while TUNEL$^+$ cells are shown in green. Scale bar, 20 µm.

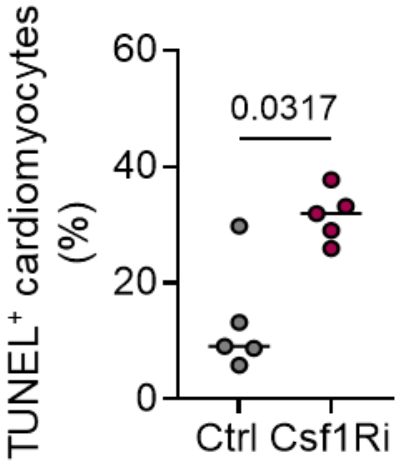

Figure 28. Apoptotic cardiomyocytes in human HFrEF tissue slices. Quantification of TUNEL-positive cardiomyocytes as an indicator of apoptosis in human HFrEF tissue slices treated with Csf1Ri (n= 5 slices/4 hearts) compared to vehicle control (n = 5 slices/4 hearts). For each slice, 10 FOVs were analyzed in the central region, with transmitted light used to distinguish cardiomyocyte nuclei from other cell types. Data are shown as mean ± SEM, with individual data points representing single tissue slices. Statistical significance was assessed using the Mann-Whitney U test.

Considering the increase in cardiomyocyte apoptosis in macrophage-depleted HFrEF tissue, oxidative stress was evaluated as a potential driver of cell death and contractile dysfunction. H_2O_2 levels in culture supernatants extracted on day 10 of culturing were evaluated with an AmplexRed Assay. Human HFrEF tissue slices treated with Csf1Ri

(n= 20 slices/10 hearts) showed significantly elevated H_2O_2 concentrations of 28.7 ± 12.8% compared to vehicle control (n= 21 slices/10 hearts) (Figure 29).

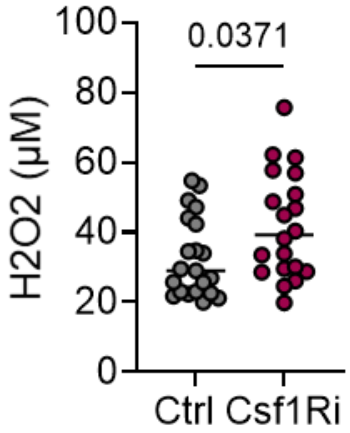

Figure 29. H2O2 concentrations in human HFrEF heart tissue slices. H_2O_2 levels in culture supernatants extracted on day 10 in Csf1Ri-treated human HFrEF tissue slices (n= 20 slices/10 hearts) compared to vehicle control (n= 21 slices/10 hearts). Data are shown as mean ± SEM, with individual data points representing single tissue slices. Statistical significance was assessed by two-sided unpaired t-tests.

4.4 Mitochondrial dysfunction in macrophage-depleted human tissue slices

4.4.1 Macrophage depletion leads to reduced bioenergetic capacity

Given their essential role in cardiomyocyte health, mitochondria were investigated as potential drivers of the observed contractile dysfunction, as well as contributors to apoptosis and excessive ROS production in macrophage-depleted human HFrEF tissue slices.

To evaluate mitochondrial respiratory function, high-resolution respirometry (Oroboros-O2k technology) was performed using substrate-inhibitor titration protocols to analyze respiratory chain complexes and oxidative phosphorylation (OXPHOS) capacity (Figure 30, original traces).

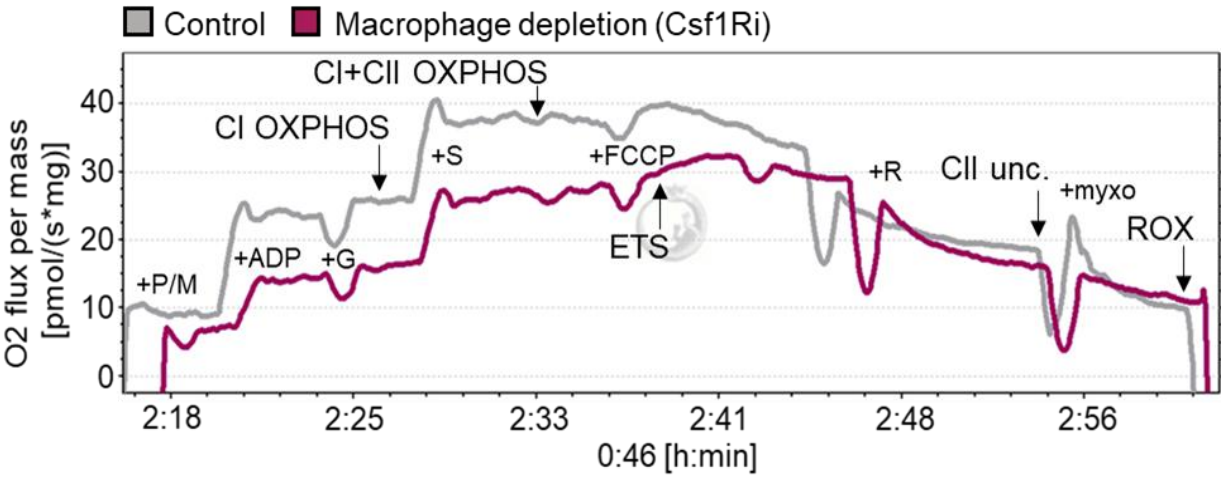

Figure 30. Original traces of OXPHOS measurements. Original OXPHOS traces of human HFrEF tissue slices treated with Csf1Ri compared to vehicle control are shown. The recorded respiratory states included: complex-I-linked oxidative phosphorylation capacity (CI OXPHOS; supported by malate (M), pyruvate (P), ADP and glutamate (G)), combined complex I+II oxidative phosphorylation capacity (CI+II OXPHOS; after addition of succinate (S)), maximal electron transport system capacity (ETS; following uncoupling with FCCP) and complex II-driven respiration (CII uncoupled (unc.), following inhibition of CI with rotenone (R)). Residual oxygen consumption (ROX) was determined after CIII inhibition with myxothiazol (myxo) and consequently subtracted from all respiratory parameters.

Macrophage-depleted human HFrEF tissue slices revealed impaired mitochondrial respiration, reflected in a 50.5 ± 22.5% decrease in complex I-driven oxidative phosphorylation (CI OXPHOS, Figure 31a) and a 43.9 ± 14.8% decrease in maximum oxidative phosphorylation capacity (CI+II OXPHOS, Figure 31b). Furthermore, even after uncoupling, reduced maximal respiratory activity remained detectable (49.2 ± 19.1% decrease), demonstrating a dysfunction of the entire electron transport system (ETS, Figure 31c). While maximum complex II-driven capacity (CII unc.) was only reduced by trend, it still showed a decrease of 46.9 ± 24.7% (Figure 31d).

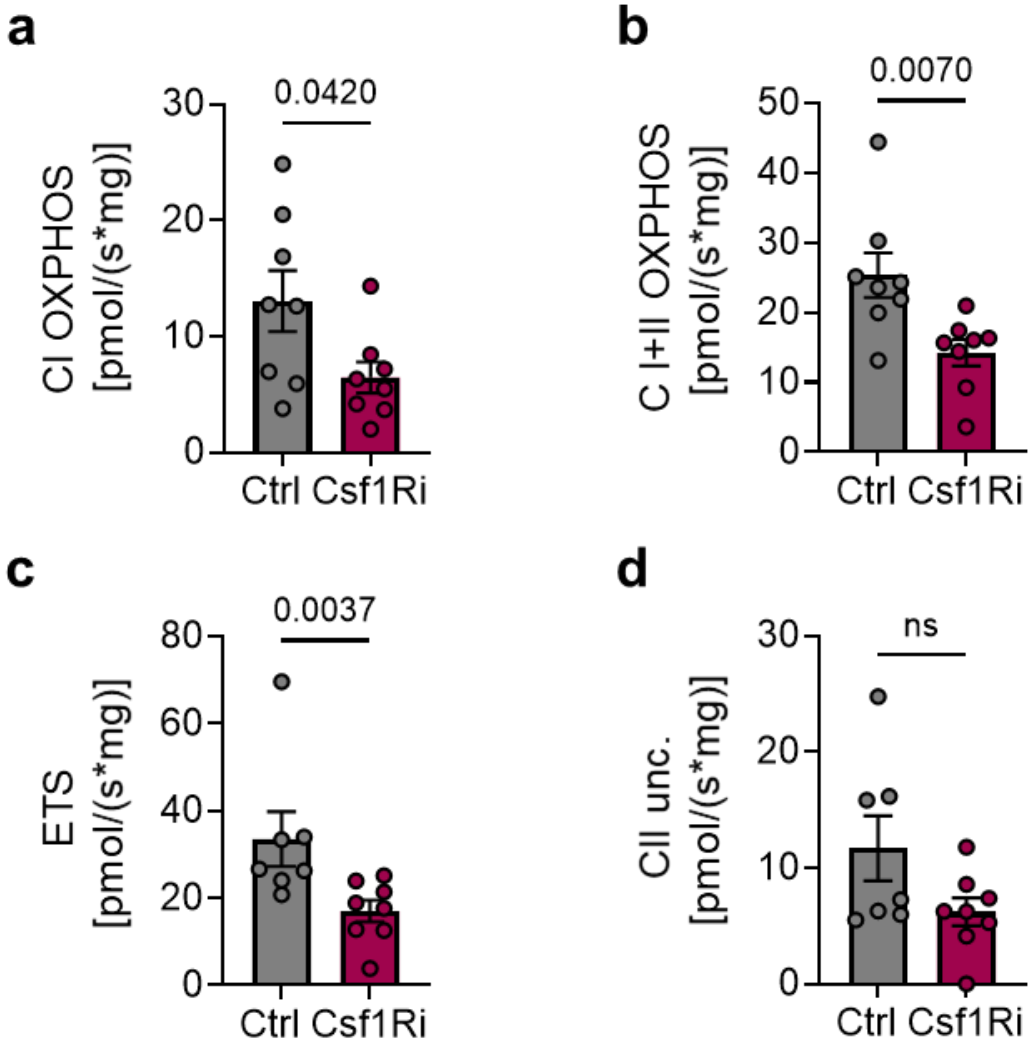

Figure 31. OXPHOS measurements in human HFrEF tissue slices. Mitochondrial respiration of Csf1Ri-treated human HFrEF tissue slices (a: Complex I-driven oxidative phosphorylation; b: maximum oxidative phosphorylation capacity; c: electron transport system; d: maximum complex II-driven capacity: n= 8 slices/5 hearts) versus vehicle control (Complex I-driven oxidative phosphorylation, maximum oxidative phosphorylation capacity: n= 8 slices/5 hearts; maximum complex II-driven capacity, electron transport system: n= 7 slices/5 hearts) using high-resolution respirometry. Respiration rates were normalized to tissue wet weight. Data are shown as mean ± SEM, with individual data points representing single tissue slices. Statistical significance was assessed using the Mann-Whitney U test.

4.4.2 Macrophage depletion leads to decreased complex IV activity in human tissue slices

Assessing complex IV in OXPHOS measurements is challenging, since its activity is not rate-limiting under physiological conditions and requires artificial substrates, which introduce background artefacts that reduce measurement precision [156]. Therefore, an isolated complex IV activity assay from lysed human HFrEF tissue slices after 10

days of Csf1Ri-treatment, was performed. Hereby, a significant decrease of 19.4 ± 8.6% in mitochondrial complex-IV-activity of macrophage-depleted human tissue slices (9 slices/4 hearts) compared to vehicle control (9 slices/4 hearts) could be observed (Figure 32).

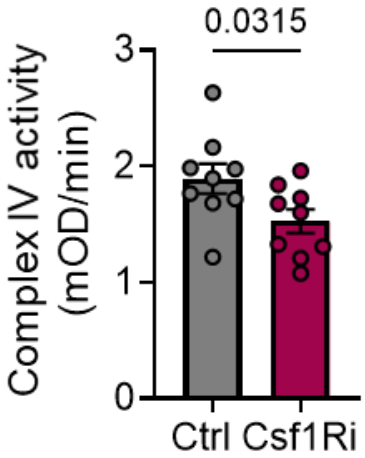

Figure 32. Complex IV activity in human HFrEF tissue slices. Mitochondrial complex IV enzyme activity in human HFrEF tissue slices treated with Csf1Ri (n= 9slices/4 hearts) compared to vehicle control (n= 9 slices/4 hearts). Data are shown as mean ± SEM, with individual data points representing single tissue slices. Statistical significance was assessed using two-sided unpaired t-tests.

4.4.3 TEM reveals increased mitochondrial size and morphological abnormalities

As OXPHOS measurements revealed mitochondrial dysfunction, ultrastructural analysis of human HFrEF tissue slices with and without Csf1Ri-treatment were performed on day 10 using transmission electron microscopy (TEM) (Figure 33). While no differences in total mitochondrial count could be detected between both groups (Figure 34a) mitochondrial size was significantly enlarged by 37.1 ± 5.8% in macrophage-depleted tissue slices (Figure 34b). Furthermore, 4-fold increase in the proportion of dysfunctional mitochondria was observed, characterized by abnormal morphology including hydropic swelling, lamellar membrane structures and loss of mitochondrial membrane integrity (Figure 34c).

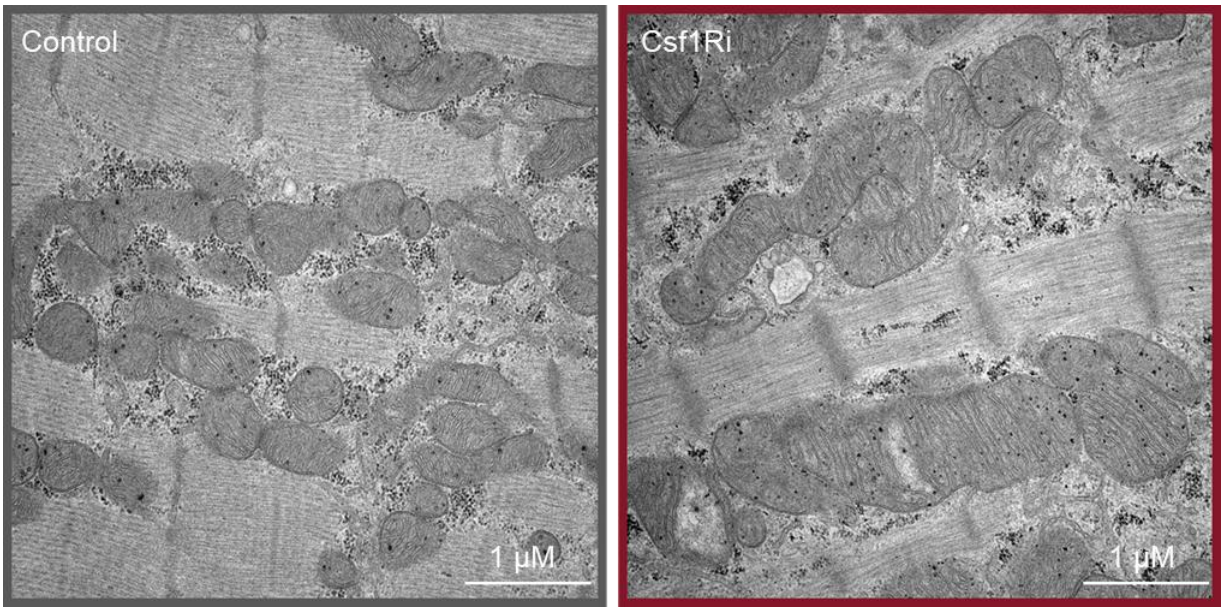

Figure 33. Ultrastructural analysis of mitochondria in human HFrEF tissue slices. Representative TEM images of human HFrEF tissue slices on day 10. Tissues were treated with vehicle (Control, left) or a CSF1R inhibitor (Csf1Ri, right). Scale bar, 1 µm.

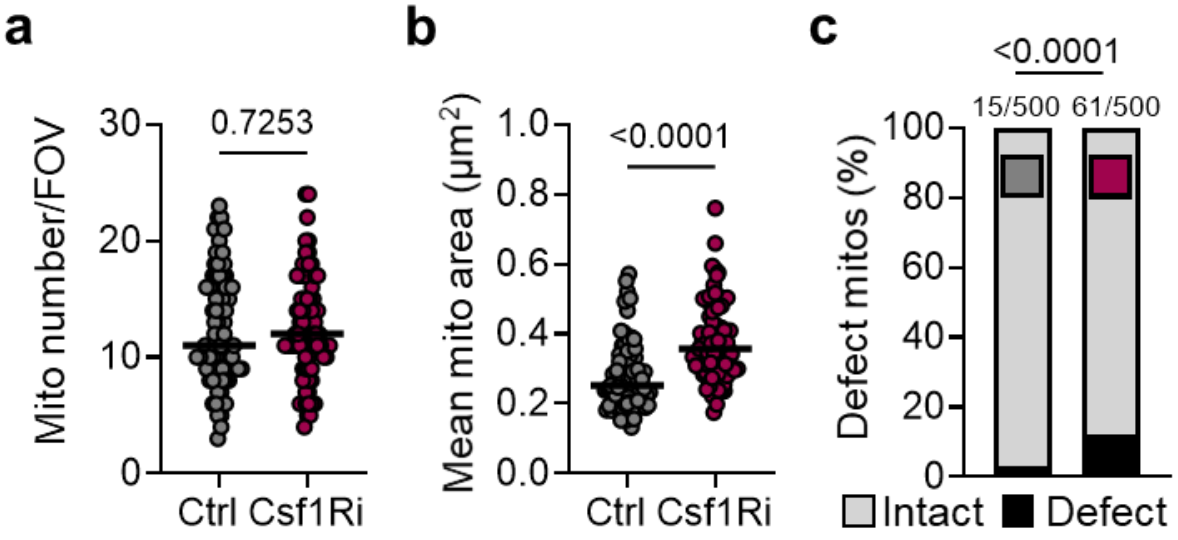

Figure 34. Mitochondrial count and morphology in human HFrEF tissue slices. (a) Mitochondrial count/FOV, (b) mean mitochondrial area (µm²) and (c) percent of defective mitochondria were assessed in Csf1Ri-treated human HFrEF tissue slices (n=83 FOV/3 hearts) versus vehicle control (n=83 FOV/3 hearts). Statistical significance was evaluated using two-sided unpaired t-tests (a,b) and Fisher´s exact test (c).

4.4.4 Macrophage depletion leads to reduced cristae density and matrix electron density

Mitochondrial integrity and functional capacity are largely defined by cristae structure and matrix electron density of individual mitochondria. High cristae density and a dense mitochondrial matrix are thereby morphological hallmarks of well-preserved mitochondrial integrity and functional capacity [157, 158]. Morphometric analysis via TEM revealed a significant reduction of 34.6 ± 4.4% in cristae density in macrophage-depleted tissue slices (n= 82 mitochondria/3hearts, 10 FOVs per slice) compared to vehicle control (n= 74 mitochondria/3 hearts, 10 FOVs per slice) (Figure 36a), along with a significant decrease of 12.1 ± 2.3% in mitochondrial matrix electron density, (Csf1Ri: n= 45 mitochondria; Ctrl: n= 45 mitochondria; Figure 36b) reflecting compromised mitochondrial integrity.

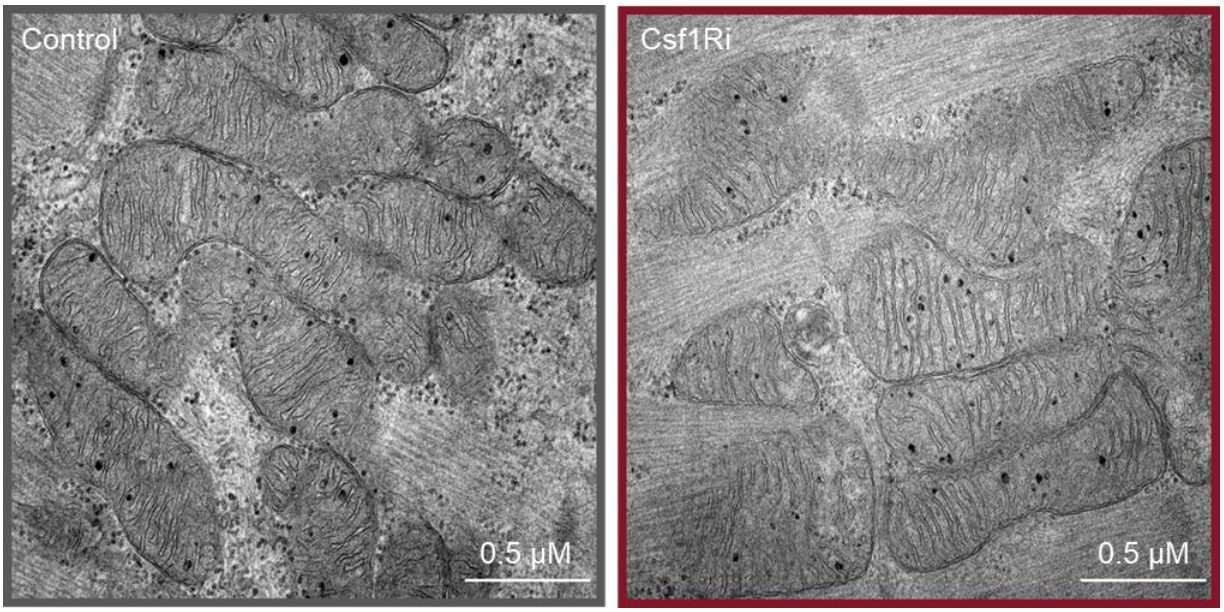

Figure 35. Ultrastructural analysis of cristae density in human HFrEF tissue slices via TEM. Representative TEM image of human HFrEF tissue slices on day 10 of Csf1Ri treatment. Tissue slices were treated with vehicle (Control, left) or a CSF1R inhibitor (Csf1Ri, right). Scale bar, 0.5 µm.

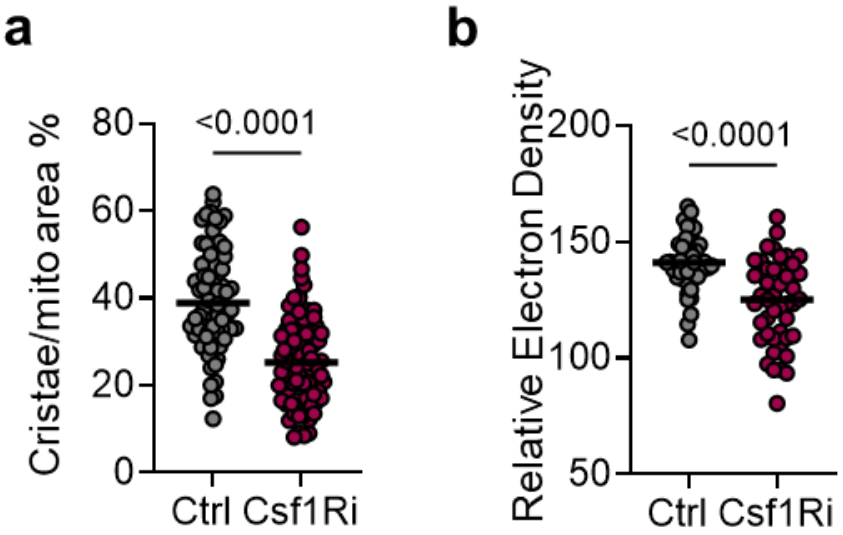

Figure 36. Mitochondrial cristae density and electron density in human HFrEF tissue slices. (a) Percentage of cristae area per mitochondrial area (%) was quantified in human HFrEF tissue slices treated with (n= 82 mitochondria/3hearts, 10 FOVs per slice) and without (n= 74 mitochondria/3 hearts, 10 FOVs per slice) Csf1Ri on day 10. (b) Relative electron density in human HFrEF tissue slices treated with Csf1Ri (n= 45 mitochondria) compared to vehicle control (n= 45 mitochondria) was calculated as the inverted grey value (255- mean grey value) and normalized to a reference greyscale to correct for differences in image brightness. Each data point represents a single mitochondrion. Statistical significance was evaluated using two-sided unpaired t-tests.

4.5 Csf1Ri treatment in human iPSC-CM does not show differences in OXPHOS capacity

To assess potential off-target effects of the Csf1Ri PLX-5662 on cardiomyocytes, induced pluripotent stem cell derived cardiomyocytes (iPSC-CM) were used. This approach served to verify that the effects of Csf1Ri on cardiomyocyte apoptosis and mitochondrial dysfunction were not caused by direct effects of the compound on cardiomyocytes. Since iPSC-CM cultures do not contain macrophages, they represent a suitable model in which no effects would be expected if the compound acts solely via macrophage inhibition. Moreover, iPSC-CM are a human model and are suitable for the long treatment period with Csf1Ri according to the treatment of the human myocardial slices.

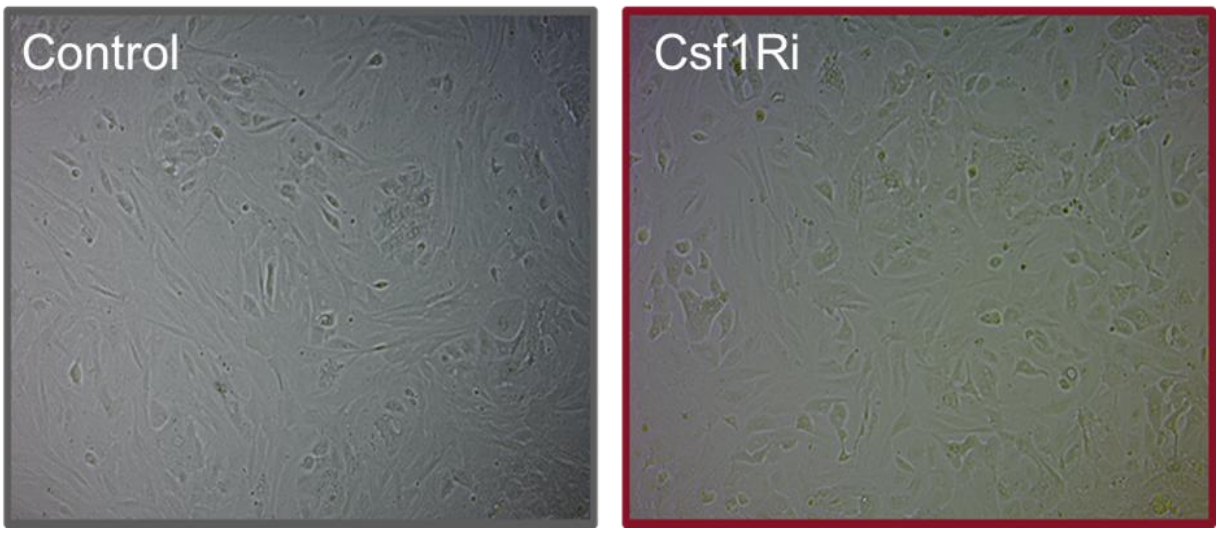

Figure 37. Morphological analysis of the effect of Csf1Ri PLX-5622 on human iPSC-CM. Human iPSC-CM were cultured and treated with a Csf1Ri for 10 days. After treatment, a morphological analysis was conducted via light microscope. Vehicle control is displayed on the left, while Csf1Ri-treated iPSC-CM are displayed on the right.

Morphological analysis of iPSC-CM cultured with or without Csf1Ri for 10 days showed comparable structural characteristics with no apparent morphological differences between both groups (Figure 37). Furthermore, mitochondrial metabolic analysis with high-resolution respirometry (Oroboros-2k) showed no significant differences in the bioenergetic capacity of Csf1Ri-treated iPSC-CM compared to controls, as complex I related oxidative phosphorylation (CI OXPHOS), maximum oxidative phosphorylation capacity (CI+II OXPHOS), electron transfer system (ETS) and Maximum complex II-driven capacity (CII unc.) remained unchanged (Figure 38a-d). These findings support that the Csf1Ri PLX-5622 has no unwanted off-target effects on cardiomyocytes.

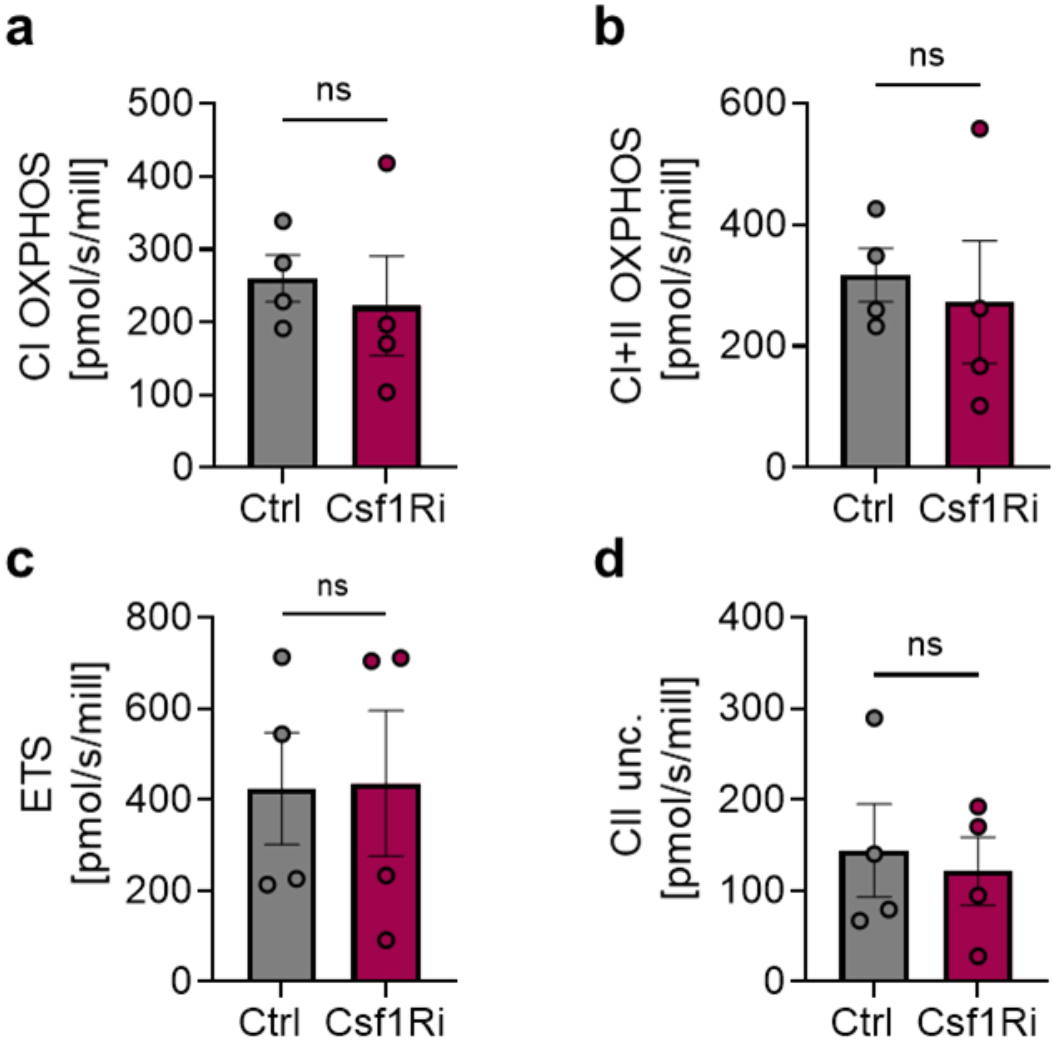

Figure 38. OXPHOS measurements in human iPSC-CM treated with Csf1Ri. Mitochondrial respiration of cultured human iPSC-CM treated with Csf1Ri compared to vehicle control (4 differentiations each) assessed with high-resolution respirometry on day 10. (a) Complex I-driven oxidative phosphorylation, (b) maximum oxidative phosphorylation capacity (c) electron transport system and (d) maximum complex II-driven capacity were evaluated by using a substrate-inhibitor titration protocol. Respiration rates were normalized to cell number. Data are represented as mean ± SEM with each data point representing one iPSC-CM differentiation (approximately 300 000 cells/group). Statistical analysis was performed using the Mann-Whitney U test.

5 Discussion

HFrEF is a severe disorder defined by impaired contractility and reduced stroke volume, ultimately compromising cardiac output [40, 159]. Despite current treatment strategies, many patients still experience disease progression, resulting in HFrEF being a major global health burden [43, 160]. In recent years, it became clear that inflammation and immune cells contribute to HFrEF pathophysiology. This realization has gained increasing attention and raised the prospect of immunomodulatory strategies as novel therapeutic approaches [44-46, 161]. However, animal studies have demonstrated essential homeostatic roles for cardiac macrophages, whereas their functions in the human heart have remained far less well defined [86, 101, 120].

This thesis for the first time evaluated the causal role of cardiac macrophages in living human HFrEF myocardium. Depletion of cardiac macrophages in cultivated human HFrEF tissue slices led to contractile dysfunction and increased apoptosis, which was associated with structural and functional mitochondrial dysfunction.

5.1 Experimental set-up and its implication

Despite the increasing interest in immunomodulatory strategies, direct experimental manipulation of immune cells in living human tissue has not been possible yet. In this context, the system of long-term culturing of human heart tissue used in this thesis introduces a novel approach that, for the first time, enables the investigation of long-term interventions targeting cardiac macrophages in living, beating human myocardial tissue. This set-up facilitates translational research investigating the role of immune cells in HFrEF.

Cardiac macrophages comprise distinct subsets that differ in both function and developmental origin. While resident macrophages contribute to cardiac homeostasis, including roles in electrical conduction and tissue repair, non-resident, recruited macrophages are mainly linked to inflammatory responses, fibrosis and maladaptive remodeling processes that exacerbate conditions like HF [94-96]. Although macrophage functions vary substantially between subsets, a depletion strategy was used in cultured human HFrEF tissue slices that targets resident and recruited

macrophage subsets [162]. Importantly, macrophage populations in chronic HF become increasingly dynamic and exhibit substantial phenotypic convergence, thereby limiting the feasibility of selective pharmacological targeting of resident versus recruited macrophages [121]. Additionally, recent transcriptomic data indicates an even greater variety of cardiac macrophage subsets than previously assumed [163]. Further research should aim to define the subset-specific functions of cardiac macrophages in human HFrEF, given that preclinical studies in animals have demonstrated divergent and even opposing effects on disease progression [79, 113, 121].

While the employed model of macrophage depletion in long-term cultured human HFrEF tissue slices represents a major step toward improved translational relevance, certain limitations must be considered. Although cultured tissue slices are maintained under electrical stimulation, the absence of perfusion precludes immune cell recruitment in this model. Nevertheless, human tissue culturing offers an exceptional platform for translational studies to investigate cellular and molecular mechanisms in living, beating human heart tissue under near-physiological conditions, making it superior to animal studies that have been used so far.

5.2 Cardiac macrophages as regulators of myocardial function

5.2.1 Contractile impairment due to macrophage depletion

Contractile impairment represents a hallmark of heart failure pathophysiology [40, 41]. Consequently, maintaining contractile function is a key therapeutic objective to ensure adequate cardiac output to meet the metabolic demands of the body.

In this work, a substantial impairment of systolic force after Csf1Ri treatment could be observed, demonstrating that macrophage depletion reduces contractile performance in human HFrEF tissue. This underlines the active role of cardiac macrophages in the regulation of myocardial function, also highlighting their protective and homeostatic capacity. These findings thereby contribute to a better understanding of the physiological functions of cardiac macrophages in human hearts, especially in the context of HFrEF. The beneficial role of cardiac macrophages is further supported by

various animal studies, which reported compromised LV function, reduced cardiac output and increased arrhythmic events both after selective depletion of cardiac resident macrophages and after broad macrophage depletion in mice [95, 99, 101, 120].

Force-frequency relationship was examined as an intrinsic regulatory mechanism of myocardial contractility. While results showed no significant differences between both experimental groups, a negative force-frequency relationship could be observed in human HFrEF tissue slices. This altered force-frequency behavior has been previously described in failing hearts and is evident both under in vitro conditions as well as in clinical settings [28].

Intracellular Ca^{2+} dynamics play a central role in determining cardiac contractility. Alterations in post-rest isometric force provide an indirect measure of SR Ca^{2+} handling, reflecting potential impairments in Ca^{2+} reuptake and subsequent release [36]. In macrophage depleted human HFrEF tissue slices, PRP measurements suggested a reduction in SR Ca^{2+} content, which may contribute to the observed impairment in contractility. Altogether, these results indicate that cardiac macrophages are important for the preservation of proper contractile function in the failing human heart.

5.2.2 Ca^{2+} handling defects after cardiac macrophage depletion

Cardiac contractility directly correlates with the amount of cytoplasmic Ca^{2+} concentration during EC coupling. Disturbances of the Ca^{2+} homeostasis thereby reduce cytosolic Ca^{2+} transients and consequently impair contractile force [8, 10, 164, 165].

As PRP measurements conducted in this thesis hinted at altered Ca^{2+} handling as a potential underlying cause of impaired contractile performance, further experiments to examine intracellular Ca^{2+} were conducted. Epifluorescence measurements in isolated human HFrEF tissue slices thereby revealed a significant reduction in Ca^{2+} transient amplitudes in Csf1Ri treated tissue, highlighting a potential link between Ca^{2+} homeostasis and cardiac macrophages that has not yet been investigated in human heart tissue. Moreover, existing animal studies have predominantly focused on the

adverse effect of recruited macrophages on cardiomyocyte Ca^{2+} homeostasis through cytokine secretion (e.g. TNF α), including inhibition of LTCCs and Ca^{2+}-ATPase and downregulation of Ca^{2+} channel expressions, collectively impairing intracellular Ca^{2+} handling [166-168]. Notably, one study utilizing co-cultivation of different macrophages and cardiomyocyte cell lines demonstrated that anti-inflammatory macrophages significantly enhanced cardiomyocyte Ca^{2+} fractional release, whereas pro-inflammatory macrophages also induced detrimental changes in SR Ca^{2+} stores [169]. While this finding along with the observed reduction in Ca^{2+} transient amplitudes in macrophage-depleted tissue in this thesis point toward a role for macrophages in modulating Ca^{2+} homeostasis, the underlying molecular mechanisms remain unclear.

One potential factor underlying changes in Ca^{2+} homeostasis after macrophage depletion refers to oxidative stress. Independent mechanisms, such as oxidation of CaMKII at the regulatory domain residues Met281/282, can result in enhanced kinase activation. This oxidative modification is often mediated by ROS, which are commonly elevated under conditions of cellular stress [170]. In this work, increased ROS could also be observed in Csf1Ri treated human HFrEF tissue slices, suggesting a macrophage-dependent modulation of redox homeostasis that may contribute to impaired Ca^{2+} handling.

As Ca^{2+} release from the SR via RyR2 during EC coupling largely determines the Ca^{2+} transient amplitude, alterations in SR Ca^{2+} content, also observed in macrophage-depleted human HFrEF tissue slices in this study, can strongly affect Ca^{2+} homeostasis and hence contractility [171]. A reduced SR Ca^{2+} content hereby may be attributed to stress kinases such as CaMKII [172].

Increased CaMKII activation driven by elevated ROS levels as well as elevated cytokine secretion due to enhanced macrophage-recruitment, both leading to impaired Ca^{2+} homeostasis and contractility, is a well-described feature of HF [170, 172]. However, macrophage-depleted human HFrEF tissue slices exhibited a more pronounced impairment of contractility and SR function compared to vehicle HFrEF tissue slices, suggesting that macrophage loss might even exacerbate these processes. Importantly, these findings represent the first indication that cardiac macrophages may play a direct role in regulating Ca^{2+} handling, highlighting a novel mechanism potentially relevant for human HFrEF pathophysiology.

5.2.3 Apoptosis and ROS after cardiac macrophage depletion

Given the close association between oxidative stress, Ca^{2+} dysregulation and cell death, apoptotic pathways and ROS production were analyzed to further clarify mechanisms underlying the observed contractile impairment in macrophage-depleted human HFrEF tissue slices [173, 174]. Accordingly, increased apoptosis of overall cells as well as specifically in cardiomyocytes could be observed in the macrophage-depleted group. Apoptosis is a key feature of HF pathophysiology, and thus apoptotic cells were anticipated in examined human HFrEF tissue slices [175, 176]. Nevertheless, the pronounced increase in apoptosis following Csf1Ri treatment suggests a protective role of cardiac macrophages and their absence may aggravate cell death, consequently leading to HF progression. This is supported by several animal studies demonstrating that depletion of cardiac macrophages led to accelerated cardiomyocyte death along with higher expression of *Bcl*-family genes associated with apoptosis which consequently led to higher mortality [113, 120, 177].

Alongside increased apoptosis, elevated levels of hydrogen peroxide, a strong reactive ROS molecule, could be observed in Csf1Ri treated human HFrEF tissue slices. These findings are consistent with previous mouse studies showing that depletion of cardiac macrophages leads to heightened ROS production and increased cardiomyocyte death [101, 120]. ROS-induced apoptosis could therefore represent another contributing factor to the contractile loss observed in macrophage-depleted human HFrEF tissue slices.

The parallel increase in ROS and apoptosis shows the strong interdependence between both processes. While under physiological conditions, ROS act as signaling molecules that regulate important processes such as cell growth, proliferation and differentiation, an excessive ROS production leads to death in cardiac cells [178, 179]. This happens primarily due to their direct oxidizing effects on macromolecules like lipids, proteins and DNA, leading to changes in molecular pathways that promote apoptotic pathways [180]. Several lines of evidence hereby indicate a close relationship between *p53* and oxidative stress, whereas ROS activate *p53*, which in turn promotes apoptosis through transcriptional upregulation of the pro-apoptotic gene

Bax [181, 182]. While elevated ROS levels drive apoptosis, apoptotic processes themselves can further enhance ROS production, creating a vicious self-reinforcing cycle.

5.3 Mitochondrial dysfunction and energetic failure in macrophage-depleted HFrEF myocardium

The heart's function largely relies on proper performance of cardiomyocytes, cells with limited regenerative potential and extraordinary energetic demands [47]. Mitochondria play a central role in this context, as they are the primary source of ATP and key regulators of metabolic signaling and cell survival [51]. Therefore, their integrity is critical for maintaining cardiomyocyte health and function.

Based on the observed increase in ROS, mitochondrial function was investigated as mitochondria are a main source of ROS in cardiomyocytes [69, 183]. Mitochondrial dysfunction could be observed in macrophage-depleted human HFrEF tissue slices, evident through compromised oxidative phosphorylation capacity and pronounced structural abnormalities. Given that TEM analysis revealed unchanged mitochondrial abundance but increased structural defects, the observed reduction in OXPHOS and ETS capacity likely reflects a qualitative rather than a quantitative mitochondrial impairment, with all respiratory chain complexes similarly affected [184]. Accordingly, the overall decline in respiratory activity likely results from the increased prevalence of structurally and functionally impaired mitochondria. Similar results were observed in an animal study where depletion of cardiac resident macrophages in adult mice via the diphtheria toxin receptor ($CD169^{DTR}$) induced mitochondrial abnormalities, including enlarged mitochondria with reduced cristae density. Proteomic analyses further revealed pronounced alterations in mitochondrial proteins, particularly those involved in bioenergetic pathways [101]. A similar phenotype was reported in a study investigating the consequences of depleting either recruited macrophages ($Ccr2^{-/-}$ mice) or all macrophage subsets via Csf1R inhibition in a hypokalemic mouse model following myocardial infarction. In both conditions, macrophage loss resulted in dysmorphic mitochondria with reduced cristae density, while functional measurements revealed diminished activity of mitochondrial respiratory chain enzymes CII and CIV,

along with a reduced mitochondrial membrane potential, indicating impaired energy production [120].

Dysfunctional mitochondria are known to generate elevated levels of ROS, which can compromise cellular integrity and directly trigger apoptotic signaling [117, 185]. In line with this notion, macrophage-depleted human HFrEF tissue slices showed increased hydrogen peroxide levels and elevated apoptosis, suggesting that mitochondrial disturbances not only impair cardiomyocyte energetics but also aggravate dysfunction due to ROS-induced apoptosis. Although mitochondrial dysfunction is often a consequence of cardiomyocyte apoptosis, TEM analysis identified non-apoptotic cardiomyocytes containing dysfunctional mitochondria, indicating that mitochondrial impairment can precede and potentially contribute to the initiation of cell death.

While dysfunctional mitochondria may be an underlying factor to the observed contractile dysfunction due to elevated ROS levels and increased apoptosis, they further play an important part in Ca^{2+} homeostasis. Several studies demonstrate that mitochondria in cardiomyocytes are tightly integrated into cellular Ca^{2+} signaling, as live-cell and in vivo imaging with optical probes have shown that they can take up cytosolic Ca^{2+} and are capable of buffering substantial amounts. They thereby not only shape cytosolic Ca^{2+} transients but also adjust metabolic output to meet contractile demands, modulating contractile activity [186-188]. Disruptions of mitochondrial integrity and function may thereby also alter Ca^{2+} homeostasis in cardiomyocytes, further worsening the contractile output.

Mitochondrial dysfunction is a hallmark of HF and accumulating evidence underscores the critical role of cardiac macrophages in preserving mitochondrial homeostasis, a function critically dependent on proper mitochondrial quality control [99, 100, 111, 189]. Cardiac macrophages were just recently recognized as key players in mitochondrial quality control in the heart, with dysfunctional mitochondria in cardiomyocytes being expelled into the extracellular space via subcellular vesicles (namely exophers) and consequently degraded by surrounding cardiac macrophages through phagocytosis mediated by the receptor *Mertk* [101, 117]. In chimeric mice generated by bone marrow transplantation, fluorescently labeled material was shown to transfer from cardiomyocytes into macrophages, while in vitro imaging confirmed the uptake of

exopher-like particles by purified cardiac macrophages. This process was found to account for more than half of degraded mitochondria in cardiomyocytes [101]. A depletion of cardiac macrophages in mice either via the diphtheria toxin receptor ($CD169^{DTR}$) or a Csf1R inhibitor resulted in accumulation of dysfunctional mitochondria within the extracellular space, which triggered inflammasome activation and autophagy blockade, ultimately compromising mitochondrial integrity, tissue homeostasis and cardiac function [101, 120].

Consistent with the observed effects of Csf1R inhibition in cultured human heart tissue, it could be demonstrated for the first time that cardiac macrophages are essential for maintaining cardiac homeostasis in HFrEF. Beyond their traditional role in immune surveillance, they also act as critical regulators of myocardial homeostasis. Given that mitochondrial function is already impaired in HF, the quality control mechanism described may be particularly critical for preserving mitochondrial function in HFrEF.

5.4 Implications for cardiac immunomodulation and clinical relevance

Despite available therapies, HF progression remains common, underscoring its substantial global health burden while highlighting the need for novel treatment strategies [160]. Recently, cardio-immunotherapies are gaining increasing attention as the critical roles of immune cells, especially cardiac macrophages, in heart disease become better understood. Particularly in HF, modulating immune-cardiomyocyte interactions could represent a promising new therapeutic approach to enhance myocardial function, as cardiac macrophages maintain cardiomyocyte homeostasis, whereas dysregulated immune activity contributes to chronic inflammation, impaired contractility and cardiomyocyte death [94, 101]. However, translational progress is limited by the current inability of testing macrophage interventions in living human heart tissue.

With the established system in this thesis, long-term culture of human heart tissue was feasible, enabling macrophage-targeting intervention. Under homeostatic conditions, the heart contains a heterogeneous population of cardiac macrophages, with resident $CCR2^{-}$ supporting tissue homeostasis while $CCR2^{+}$ macrophages exhibit

predominantly pro-inflammatory features [94-96]. During chronic HF, macrophage populations become even more dynamic and phenotypically convergent, as resident macrophages are gradually replaced by recruited $CCR2^+$ macrophages [96, 121]. The abundance of $CCR2^+$ macrophages thereby directly correlates with adverse remodeling in HF patients [94]. In the HFrEF tissue examined in this thesis, overall macrophage numbers are expected to be increased due to enhanced recruitment, as reported in HF models [121, 190]. Consequently, recruited $CCR2^+$ macrophages are likely to be predominant, while resident macrophages may be present at lower numbers [79, 191]. However, depletion of $CD68^+$ macrophages without targeting specific subsets, despite their dichotomous contributions to disease pathogenesis and progression, showed worsening cardiac contractility in HFrEF tissue.

Interestingly, single-cell transcriptomic studies in mice with HF showed that resident macrophages are, despite enhanced recruitment of monocyte-derived macrophages, not completely replaced but a small fraction of 2-5% persists [94-96]. Notably, depletion of this fraction exacerbated cardiac remodeling and led to impaired heart function, indicating that even small populations of resident macrophages play an essential role in cardiac repair [95, 192].

In recent years, several efforts have been made to find therapeutic approaches targeting macrophage modulation, mainly by focusing on enhancing the presence of anti-inflammatory macrophages while suppressing pro-inflammatory signaling to mitigate adverse remodeling [193-195]. Thereby, a new and promising strategy is ex vivo cell therapy, which offers an alternative to in vivo interventions by overcoming common delivery obstacles. Through ex vivo reprogramming, macrophages can be generated in large numbers and tailored toward specific phenotypes, such as reparative or anti-inflammatory states. These re-educated macrophages have been shown to reduce fibrosis and prevent adverse remodeling in mice [196]. However, these approaches have been limited to animal models and have not yet been translated successfully into clinical application. The heterogeneity and plasticity of cardiac macrophages further complicate therapeutic targeting, as their phenotype can shift in response to the (inflammatory) milieu. Consequently, the timing, context and subset specificity of macrophage-target interventions will be crucial determinants of therapeutic success.

Selective pharmacological targeting of subset-specific cardiac macrophages remains challenging and is currently not feasible in the clinical setting. However, macrophage depletion leads to detrimental effects, worsening cardiac function. The results of this thesis highlight both the therapeutic potential as well as the risks of macrophage modulation. Defining specific roles of macrophage subsets in human HFrEF will be essential to enable precise and safe immunomodulatory therapies, as animal models demonstrated divergent effects [79, 113, 121]. Subset-specific targeting strategies for macrophage modulation should therefore be examined in future studies.

6 Conclusion

Heart failure with reduced ejection fraction (HFrEF) remains a major global health burden, with patients often experiencing disease progression despite current treatment options. Growing evidence highlights the role of inflammation in cardiac diseases, thereby shifting focus toward immunoregulatory interventions. Given the lack of experimental models capable of assessing the functional impact of cardiac macrophages in the human heart, a novel system was established in this thesis, allowing long-term culturing of human cardiac tissue and targeted macrophage intervention. This approach enabled direct investigation of macrophage-mediated mechanisms in human HFrEF.

The depletion of cardiac macrophages in human HFrEF tissue slices resulted in impaired contractile performance, reflected by reduced systolic force amplitudes, impaired Ca^{2+} transients and defective SR Ca^{2+} handling. These results provide the first indication that cardiac macrophages may also have a direct role in the Ca^{2+} homeostasis of cardiomyocytes. Along with that, increased oxidative stress and cardiomyocyte apoptosis could be observed in macrophage-depleted HFrEF tissue slices. Furthermore, mitochondria showed reduced respiratory chain activity across all complexes and higher proportion of structurally damaged mitochondria at the cellular level, indicating a pronounced mitochondrial dysfunction.

Collectively, these findings provide the first functional evidence that cardiac macrophages are essential for maintaining myocardial function in human HFrEF tissue, most likely due to their homeostatic roles in regulating mitochondrial quality control and facilitating the clearance of dysfunctional mitochondria to preserve cellular integrity. By revealing a direct link between immune cell presence and contractile performance, this work underscores the important role of cardiac macrophages in sustaining myocardial function, highlighting them as potential therapeutic targets in HF. However, future therapeutic efforts should focus on strategies that selectively support or enhance the reparative functions of specific subtypes of cardiac macrophages, rather than broadly targeting all macrophage populations.

7 References

1. Langer, G.A., *The myocardium*. 1997: Academic Press.
2. Severs, N.J., *The cardiac gap junction and intercalated disc.* Int J Cardiol, 1990. **26**(2): p. 137–73.
3. Borrmann, C.M., et al., *The area composita of adhering junctions connecting heart muscle cells of vertebrates. II. Colocalizations of desmosomal and fascia adhaerens molecules in the intercalated disk.* Eur J Cell Biol, 2006. **85**(6): p. 469–85.
4. Sengupta, P.P., et al., *Left ventricular structure and function: basic science for cardiac imaging.* J Am Coll Cardiol, 2006. **48**(10): p. 1988–2001.
5. Hong, T. and R.M. Shaw, *Cardiac T-Tubule Microanatomy and Function.* Physiol Rev, 2017. **97**(1): p. 227–252.
6. Brette, F. and C. Orchard, *T-tubule function in mammalian cardiac myocytes.* Circ Res, 2003. **92**(11): p. 1182–92.
7. Beard, N.A., D.R. Laver, and A.F. Dulhunty, *Calsequestrin and the calcium release channel of skeletal and cardiac muscle.* Prog Biophys Mol Biol, 2004. **85**(1): p. 33–69.
8. Bers, D.M., *Cardiac excitation-contraction coupling.* Nature, 2002. **415**(6868): p. 198–205.
9. Pfeiffer, E.R., et al., *Biomechanics of cardiac electromechanical coupling and mechanoelectric feedback.* J Biomech Eng, 2014. **136**(2): p. 021007.
10. Ebashi, S., *Excitation-contraction coupling.* Annu Rev Physiol, 1976. **38**: p. 293–313.
11. Fabiato, A. and F. Fabiato, *Calcium and cardiac excitation-contraction coupling.* Annu Rev Physiol, 1979. **41**: p. 473–84.
12. Periasamy, M. and A. Kalyanasundaram, *SERCA pump isoforms: their role in calcium transport and disease.* Muscle Nerve, 2007. **35**(4): p. 430–42.
13. Ottolia, M., et al., *Na/Ca exchange and contraction of the heart.* J Mol Cell Cardiol, 2013. **61**: p. 28–33.
14. Maier, L.S. and D.M. Bers, *Role of Ca2+/calmodulin-dependent protein kinase (CaMK) in excitation-contraction coupling in the heart.* Cardiovasc Res, 2007. **73**(4): p. 631–40.
15. Braun, A.P. and H. Schulman, *The multifunctional calcium/calmodulin-dependent protein kinase: from form to function.* Annu Rev Physiol, 1995. **57**: p. 417–45.
16. Rosenberg, O.S., et al., *Structure of the autoinhibited kinase domain of CaMKII and SAXS analysis of the holoenzyme.* Cell, 2005. **123**(5): p. 849–60.
17. Hudmon, A. and H. Schulman, *Structure-function of the multifunctional Ca2+/calmodulin-dependent protein kinase II.* Biochem J, 2002. **364**(Pt 3): p. 593–611.
18. Erickson, J.R., et al., *A dynamic pathway for calcium-independent activation of CaMKII by methionine oxidation.* Cell, 2008. **133**(3): p. 462–74.
19. Howe, C.J., et al., *Redox regulation of the calcium/calmodulin-dependent protein kinases.* J Biol Chem, 2004. **279**(43): p. 44573–81.
20. Zhu, W., et al., *Activation of CaMKIIdeltaC is a common intermediate of diverse death stimuli-induced heart muscle cell apoptosis.* J Biol Chem, 2007. **282**(14): p. 10833–9.

21. Khoo, M.S., et al., *Death, cardiac dysfunction, and arrhythmias are increased by calmodulin kinase II in calcineurin cardiomyopathy.* Circulation, 2006. **114**(13): p. 1352–9.
22. Williams, A.J., N.L. Thomas, and C.H. George, *The ryanodine receptor: advances in structure and organization.* Current Opinion in Physiology, 2018. **1**: p. 1–6.
23. Lehnart, S. and A.R. Marks, *Regulation of ryanodine receptors in the heart.* Circ Res, 2007. **101**(8): p. 746–9.
24. Wehrens, X.H., et al., *Ca2+/calmodulin-dependent protein kinase II phosphorylation regulates the cardiac ryanodine receptor.* Circ Res, 2004. **94**(6): p. e61–70.
25. Bers, D.M., S.M. Pogwizd, and K. Schlotthauer, *Upregulated Na/Ca exchange is involved in both contractile dysfunction and arrhythmogenesis in heart failure.* Basic Res Cardiol, 2002. **97 Suppl 1**: p. I36–42.
26. Marks, A.R., *Ryanodine receptors/calcium release channels in heart failure and sudden cardiac death.* J Mol Cell Cardiol, 2001. **33**(4): p. 615–24.
27. Benitah, J.P., et al., *RyR2 and Calcium Release in Heart Failure.* Front Physiol, 2021. **12**: p. 734210.
28. Hasenfuss, G., et al., *Relation between myocardial function and expression of sarcoplasmic reticulum Ca(2+)-ATPase in failing and nonfailing human myocardium.* Circ Res, 1994. **75**(3): p. 434–42.
29. Antoons, G., et al., *Mechanisms underlying the frequency dependence of contraction and [Ca(2+)](i) transients in mouse ventricular myocytes.* J Physiol, 2002. **543**(Pt 3): p. 889–98.
30. Endoh, M., *Force-frequency relationship in intact mammalian ventricular myocardium: physiological and pathophysiological relevance.* Eur J Pharmacol, 2004. **500**(1-3): p. 73–86.
31. Paterek, A., et al., *The effect of pacing frequency on the amplitude and time-course of cardiomyocyte shortening in isolated rat cardiomyocytes.* Post. N. Med., 2016. **29**(12B): p. 9–14.
32. Mulieri, L.A., et al., *Altered myocardial force-frequency relation in human heart failure.* Circulation, 1992. **85**(5): p. 1743–50.
33. Mercadier, J.J., et al., *Altered sarcoplasmic reticulum Ca2(+)-ATPase gene expression in the human ventricle during end-stage heart failure.* J Clin Invest, 1990. **85**(1): p. 305–9.
34. Zarain-Herzberg, A., R. Estrada-Avilés, and J. Fragoso-Medina, *Regulation of sarco(endo)plasmic reticulum Ca2+-ATPase and calsequestrin gene expression in the heart.* Can J Physiol Pharmacol, 2012. **90**(8): p. 1017–28.
35. Studer, R., et al., *Gene expression of the cardiac Na(+)-Ca2+ exchanger in end-stage human heart failure.* Circ Res, 1994. **75**(3): p. 443–53.
36. Wrigley, D., *The effects of stimulation frequency on intracellular calcium handling within the sheep atrial myocyte*. 2015, University of Manchester.
37. Abreu, G.R., D.V. Vassallo, and J.G. Mill, *The Na+-Ca2+ exchange mechanism as a regulator of post rest contractions in cardiac muscle.* Braz J Med Biol Res, 1987. **20**(6): p. 817–20.
38. Pieske, B., et al., *Diminished post-rest potentiation of contractile force in human dilated cardiomyopathy. Functional evidence for alterations in intracellular Ca2+ handling.* J Clin Invest, 1996. **98**(3): p. 764–76.
39. Limas, C.J., et al., *Calcium uptake by cardiac sarcoplasmic reticulum in human dilated cardiomyopathy.* Cardiovasc Res, 1987. **21**(8): p. 601–5.

40. Bozkurt, B., et al., *Universal definition and classification of heart failure: a report of the Heart Failure Society of America, Heart Failure Association of the European Society of Cardiology, Japanese Heart Failure Society and Writing Committee of the Universal Definition of Heart Failure: Endorsed by the Canadian Heart Failure Society, Heart Failure Association of India, Cardiac Society of Australia and New Zealand, and Chinese Heart Failure Association.* Eur J Heart Fail, 2021. **23**(3): p. 352–380.
41. McDonagh, T.A., et al., *2023 Focused Update of the 2021 ESC Guidelines for the diagnosis and treatment of acute and chronic heart failure.* Eur Heart J, 2023. **44**(37): p. 3627–3639.
42. Malgie, J., et al., *Guideline-directed medical therapy for HFrEF: sequencing strategies and barriers for life-saving drug therapy.* Heart Fail Rev, 2023. **28**(5): p. 1221–1234.
43. Zhang, Y., J. Bauersachs, and H.F. Langer, *Immune mechanisms in heart failure.* Eur J Heart Fail, 2017. **19**(11): p. 1379–1389.
44. Adamo, L., et al., *Reappraising the role of inflammation in heart failure.* Nat Rev Cardiol, 2020. **17**(5): p. 269–285.
45. Mann, D.L., *The emerging role of innate immunity in the heart and vascular system: for whom the cell tolls.* Circ Res, 2011. **108**(9): p. 1133–45.
46. Van Linthout, S. and C. Tschöpe, *The Quest for Antiinflammatory and Immunomodulatory Strategies in Heart Failure.* Clin Pharmacol Ther, 2019. **106**(6): p. 1198–1208.
47. Bergmann, O., et al., *Evidence for cardiomyocyte renewal in humans.* Science, 2009. **324**(5923): p. 98–102.
48. Becker, C. and M. Hesse, *Role of Mononuclear Cardiomyocytes in Cardiac Turnover and Regeneration.* Curr Cardiol Rep, 2020. **22**(6): p. 39.
49. Hall, A.R., et al., *Mitochondrial fusion and fission proteins: novel therapeutic targets for combating cardiovascular disease.* Br J Pharmacol, 2014. **171**(8): p. 1890–906.
50. Ali Pour, P., S. Hosseinian, and A. Kheradvar, *Mitochondrial transplantation in cardiomyocytes: foundation, methods, and outcomes.* Am J Physiol Cell Physiol, 2021. **321**(3): p. C489–c503.
51. Osellame, L.D., T.S. Blacker, and M.R. Duchen, *Cellular and molecular mechanisms of mitochondrial function.* Best Pract Res Clin Endocrinol Metab, 2012. **26**(6): p. 711–23.
52. Li, P., et al., *Cytochrome c and dATP-dependent formation of Apaf-1/caspase-9 complex initiates an apoptotic protease cascade.* Cell, 1997. **91**(4): p. 479–89.
53. Taanman, J.W., *The mitochondrial genome: structure, transcription, translation and replication.* Biochim Biophys Acta, 1999. **1410**(2): p. 103–23.
54. Gray, M.W., *The endosymbiont hypothesis revisited.* Int Rev Cytol, 1992. **141**: p. 233–357.
55. Kühlbrandt, W., *Structure and function of mitochondrial membrane protein complexes.* BMC Biol, 2015. **13**: p. 89.
56. Frey, T.G. and C.A. Mannella, *The internal structure of mitochondria.* Trends Biochem Sci, 2000. **25**(7): p. 319–24.
57. Hatefi, Y., *The mitochondrial electron transport and oxidative phosphorylation system.* Annu Rev Biochem, 1985. **54**: p. 1015–69.

58. Kobayashi, A., et al., *Mechanisms Underlying the Regulation of Mitochondrial Respiratory Chain Complexes by Nuclear Steroid Receptors.* Int J Mol Sci, 2020. **21**(18).
59. Turrens, J.F., *Mitochondrial formation of reactive oxygen species.* J Physiol, 2003. **552**(Pt 2): p. 335–44.
60. Kowaltowski, A.J. and A.E. Vercesi, *Mitochondrial damage induced by conditions of oxidative stress.* Free Radic Biol Med, 1999. **26**(3-4): p. 463–71.
61. Wang, S., et al., *The mitophagy pathway and its implications in human diseases.* Signal Transduct Target Ther, 2023. **8**(1): p. 304.
62. Ashrafi, G. and T.L. Schwarz, *The pathways of mitophagy for quality control and clearance of mitochondria.* Cell Death Differ, 2013. **20**(1): p. 31–42.
63. Hoshino, A., et al., *Cytosolic p53 inhibits Parkin-mediated mitophagy and promotes mitochondrial dysfunction in the mouse heart.* Nat Commun, 2013. **4**: p. 2308.
64. Ploumi, C., I. Daskalaki, and N. Tavernarakis, *Mitochondrial biogenesis and clearance: a balancing act.* Febs j, 2017. **284**(2): p. 183–195.
65. Shires, S.E. and B. Gustafsson Å, *Mitophagy and heart failure.* J Mol Med (Berl), 2015. **93**(3): p. 253–62.
66. Billia, F., et al., *PTEN-inducible kinase 1 (PINK1)/Park6 is indispensable for normal heart function.* Proc Natl Acad Sci U S A, 2011. **108**(23): p. 9572–7.
67. Kubli, D.A., et al., *Parkin protein deficiency exacerbates cardiac injury and reduces survival following myocardial infarction.* J Biol Chem, 2013. **288**(2): p. 915–26.
68. Rosca, M.G. and C.L. Hoppel, *Mitochondrial dysfunction in heart failure.* Heart Fail Rev, 2013. **18**(5): p. 607–22.
69. Peoples, J.N., et al., *Mitochondrial dysfunction and oxidative stress in heart disease.* Exp Mol Med, 2019. **51**(12): p. 1–13.
70. Zhang, M., et al., *Contractile Function During Angiotensin-II Activation: Increased Nox2 Activity Modulates Cardiac Calcium Handling via Phospholamban Phosphorylation.* J Am Coll Cardiol, 2015. **66**(3): p. 261–272.
71. Zhang, M., et al., *NADPH oxidase-4 mediates protection against chronic load-induced stress in mouse hearts by enhancing angiogenesis.* Proc Natl Acad Sci U S A, 2010. **107**(42): p. 18121–6.
72. Choudhary, G. and S.C. Dudley, Jr., *Heart failure, oxidative stress, and ion channel modulation.* Congest Heart Fail, 2002. **8**(3): p. 148–55.
73. Ramos, G.C., et al., *Myocardial aging as a T-cell-mediated phenomenon.* Proc Natl Acad Sci U S A, 2017. **114**(12): p. E2420–e2429.
74. Banerjee, D., R. Tian, and S. Cai, *The Role of Innate Immune Cells in Cardiac Injury and Repair: A Metabolic Perspective.* Curr Cardiol Rep, 2023. **25**(7): p. 631–640.
75. Epelman, S., P.P. Liu, and D.L. Mann, *Role of innate and adaptive immune mechanisms in cardiac injury and repair.* Nat Rev Immunol, 2015. **15**(2): p. 117–29.
76. Lafuse, W.P., D.J. Wozniak, and M.V.S. Rajaram, *Role of Cardiac Macrophages on Cardiac Inflammation, Fibrosis and Tissue Repair.* Cells, 2020. **10**(1): p. 51.
77. Litviňuková, M., et al., *Cells of the adult human heart.* Nature, 2020. **588**(7838): p. 466–472.
78. Aurora, A.B., et al., *Macrophages are required for neonatal heart regeneration.* J Clin Invest, 2014. **124**(3): p. 1382–92.

79. Lavine, K.J., et al., *Distinct macrophage lineages contribute to disparate patterns of cardiac recovery and remodeling in the neonatal and adult heart.* Proc Natl Acad Sci U S A, 2014. **111**(45): p. 16029–34.
80. Koc, A. and E. Cagavi, *Cardiac Immunology: A New Era for Immune Cells in the Heart.* Adv Exp Med Biol, 2021. **1312**: p. 75–95.
81. O'Neill, L.A., R.J. Kishton, and J. Rathmell, *A guide to immunometabolism for immunologists.* Nat Rev Immunol, 2016. **16**(9): p. 553–65.
82. Fragasso, G., et al., *The crosstalk between immune activation and metabolism in heart failure. A scientific statement of the Heart Failure Association of the ESC.* Eur J Heart Fail, 2025.
83. Mouton, A.J., O.J. Rivera, and M.L. Lindsey, *Myocardial infarction remodeling that progresses to heart failure: a signaling misunderstanding.* Am J Physiol Heart Circ Physiol, 2018. **315**(1): p. H71–h79.
84. Steffens, S., M. Nahrendorf, and R. Madonna, *Immune cells in cardiac homeostasis and disease: emerging insights from novel technologies.* Eur Heart J, 2022. **43**(16): p. 1533–1541.
85. Mann, D.L., *Innate immunity and the failing heart: the cytokine hypothesis revisited.* Circ Res, 2015. **116**(7): p. 1254–68.
86. Nahrendorf, M., et al., *The healing myocardium sequentially mobilizes two monocyte subsets with divergent and complementary functions.* J Exp Med, 2007. **204**(12): p. 3037–47.
87. Shahid, F., G.Y.H. Lip, and E. Shantsila, *Role of Monocytes in Heart Failure and Atrial Fibrillation.* J Am Heart Assoc, 2018. **7**(3).
88. Peng, M., et al., *Macrophages: Subtypes, Distribution, Polarization, Immunomodulatory Functions, and Therapeutics.* MedComm (2020), 2025. **6**(8): p. e70304.
89. DeBerge, M., et al., *Immunometabolism at the Heart of Cardiovascular Disease.* JACC Basic Transl Sci, 2023. **8**(7): p. 884–904.
90. Caiati, C. and E. Jirillo, *The Immune System, An Arrow into the Heart. Principles of Cardioimmunology, An Emerging Branch in Medicine.* Curr Vasc Pharmacol, 2025. **23**(3): p. 162–171.
91. Liu, Y., et al., *The effector cells and cellular mediators of immune system involved in cardiac inflammation and fibrosis after myocardial infarction.* J Cell Physiol, 2020. **235**(12): p. 8996–9004.
92. Cohen, C.D., et al., *Myocardial Immune Cells: The Basis of Cardiac Immunology.* J Immunol, 2023. **210**(9): p. 1198–1207.
93. Ding, S., et al., *Non-cardiomyocytes in the heart in embryo development, health, and disease, a single-cell perspective.* Front Cell Dev Biol, 2022. **10**: p. 873264.
94. Bajpai, G., et al., *The human heart contains distinct macrophage subsets with divergent origins and functions.* Nat Med, 2018. **24**(8): p. 1234–1245.
95. Dick, S.A., et al., *Self-renewing resident cardiac macrophages limit adverse remodeling following myocardial infarction.* Nat Immunol, 2019. **20**(1): p. 29–39.
96. Dick, S.A., et al., *Three tissue resident macrophage subsets coexist across organs with conserved origins and life cycles.* Sci Immunol, 2022. **7**(67): p. eabf7777.
97. Pinto, A.R., et al., *Revisiting cardiac cellular composition.* Circulation research, 2016. **118**(3): p. 400–409.

98. Swirski, F.K. and M. Nahrendorf, *Cardioimmunology: the immune system in cardiac homeostasis and disease.* Nat Rev Immunol, 2018. **18**(12): p. 733–744.
99. Hulsmans, M., et al., *Macrophages facilitate electrical conduction in the heart.* Cell, 2017. **169**(3): p. 510–522. e20.
100. Nahrendorf, M. and F.K. Swirski, *Monocyte and macrophage heterogeneity in the heart.* Circ Res, 2013. **112**(12): p. 1624–33.
101. Nicolas-Avila, J.A., et al., *A network of macrophages supports mitochondrial homeostasis in the heart.* Cell, 2020. **183**(1): p. 94–109. e23.
102. Gomez Perdiguero, E., et al., *Tissue-resident macrophages originate from yolk-sac-derived erythro-myeloid progenitors.* Nature, 2015. **518**(7540): p. 547–51.
103. Epelman, S., et al., *Embryonic and adult-derived resident cardiac macrophages are maintained through distinct mechanisms at steady state and during inflammation.* Immunity, 2014. **40**(1): p. 91–104.
104. Lavine, K.J., et al., *Distinct macrophage lineages contribute to disparate patterns of cardiac recovery and remodeling in the neonatal and adult heart.* Proceedings of the National Academy of Sciences, 2014. **111**(45): p. 16029–16034.
105. Spurthi, K.M., et al., *Toll-like receptor 2 deficiency hyperactivates the FoxO1 transcription factor and induces aging-associated cardiac dysfunction in mice.* J Biol Chem, 2018. **293**(34): p. 13073–13089.
106. Li, J., et al., *The role of cardiac resident macrophage in cardiac aging.* Aging Cell, 2023. **22**(12): p. e14008.
107. Wang, M. and A.M. Shah, *Age-associated pro-inflammatory remodeling and functional phenotype in the heart and large arteries.* J Mol Cell Cardiol, 2015. **83**: p. 101–11.
108. Molawi, K., et al., *Progressive replacement of embryo-derived cardiac macrophages with age.* J Exp Med, 2014. **211**(11): p. 2151–8.
109. Ma, Y., A.J. Mouton, and M.L. Lindsey, *Cardiac macrophage biology in the steady-state heart, the aging heart, and following myocardial infarction.* Transl Res, 2018. **191**: p. 15–28.
110. Chakarov, S., et al., *Two distinct interstitial macrophage populations coexist across tissues in specific subtissular niches.* Science, 2019. **363**(6432): p. eaau0964.
111. Sugita, J., et al., *Cardiac macrophages prevent sudden death during heart stress.* Nat Commun, 2021. **12**(1): p. 1910.
112. Haubner, B.J., et al., *Complete cardiac regeneration in a mouse model of myocardial infarction.* Aging (Albany NY), 2012. **4**(12): p. 966–77.
113. Wong, N.R., et al., *Resident cardiac macrophages mediate adaptive myocardial remodeling.* Immunity, 2021. **54**(9): p. 2072–2088.e7.
114. Haider, N., et al., *Transition of Macrophages to Fibroblast-Like Cells in Healing Myocardial Infarction.* J Am Coll Cardiol, 2019. **74**(25): p. 3124–3135.
115. Schmidt, A.A., et al., *Polarized macrophages modulate cardiac structure and contractility under hypoxia in novel immuno-heart on a chip.* APL Bioeng, 2025. **9**(2): p. 026114.
116. Lock, R.I., et al., *Macrophages enhance contractile force in iPSC-derived human engineered cardiac tissue.* Cell Rep, 2024. **43**(6): p. 114302.
117. Liang, W., et al., *Mitochondria are secreted in extracellular vesicles when lysosomal function is impaired.* Nat Commun, 2023. **14**(1): p. 5031.

118. Killackey, S.A., D.J. Philpott, and S.E. Girardin, *Mitophagy pathways in health and disease.* J Cell Biol, 2020. **219**(11).
119. Davis, C.H., et al., *Transcellular degradation of axonal mitochondria.* Proc Natl Acad Sci U S A, 2014. **111**(26): p. 9633–8.
120. Grune, J., et al., *Neutrophils incite and macrophages avert electrical storm after myocardial infarction.* Nat Cardiovasc Res, 2022. **1**(7): p. 649–664.
121. Sager, H.B., et al., *Proliferation and Recruitment Contribute to Myocardial Macrophage Expansion in Chronic Heart Failure.* Circ Res, 2016. **119**(7): p. 853–64.
122. Frangogiannis, N.G., *Cardiac fibrosis: Cell biological mechanisms, molecular pathways and therapeutic opportunities.* Mol Aspects Med, 2019. **65**: p. 70–99.
123. Kong, P., P. Christia, and N.G. Frangogiannis, *The pathogenesis of cardiac fibrosis.* Cell Mol Life Sci, 2014. **71**(4): p. 549–74.
124. Jian, Y., et al., *Crosstalk between macrophages and cardiac cells after myocardial infarction.* Cell Commun Signal, 2023. **21**(1): p. 109.
125. Hoyer, F.F., et al., *Tissue-Specific Macrophage Responses to Remote Injury Impact the Outcome of Subsequent Local Immune Challenge.* Immunity, 2019. **51**(5): p. 899–914.e7.
126. Hume, D.A. and K.P. MacDonald, *Therapeutic applications of macrophage colony-stimulating factor-1 (CSF-1) and antagonists of CSF-1 receptor (CSF-1R) signaling.* Blood, 2012. **119**(8): p. 1810–20.
127. Peyraud, F., S. Cousin, and A. Italiano, *CSF-1R Inhibitor Development: Current Clinical Status.* Curr Oncol Rep, 2017. **19**(11): p. 70.
128. Wang, Z., et al., *An immune cell atlas reveals the dynamics of human macrophage specification during prenatal development.* Cell, 2023. **186**(20): p. 4454–4471.e19.
129. Kedia, S., et al., *T cell-mediated microglial activation triggers myelin pathology in a mouse model of amyloidosis.* Nat Neurosci, 2024. **27**(8): p. 1468–1474.
130. Babaeijandaghi, F., et al., *DPPIV(+) fibro-adipogenic progenitors form the niche of adult skeletal muscle self-renewing resident macrophages.* Nat Commun, 2023. **14**(1): p. 8273.
131. Wu, Z., et al., *Peripheral nervous system microglia-like cells regulate neuronal soma size throughout evolution.* Cell, 2025. **188**(8): p. 2159–2174.e15.
132. Peng, T., et al., *Individualized patient tumor organoids faithfully preserve human brain tumor ecosystems and predict patient response to therapy.* Cell Stem Cell, 2025. **32**(4): p. 652–669.e11.
133. Moysidou, C.M., C. Barberio, and R.M. Owens, *Advances in Engineering Human Tissue Models.* Front Bioeng Biotechnol, 2020. **8**: p. 620962.
134. Jackman, C.P., et al., *Human Cardiac Tissue Engineering: From Pluripotent Stem Cells to Heart Repair.* Curr Opin Chem Eng, 2015. **7**: p. 57–64.
135. Fischer, C., et al., *Long-term functional and structural preservation of precision-cut human myocardium under continuous electromechanical stimulation in vitro.* Nat Commun, 2019. **10**(1): p. 117.
136. Lakowicz, J.R., *Introduction to Fluorescence*, in *Principles of Fluorescence Spectroscopy*, J.R. Lakowicz, Editor. 1999, Springer US: Boston, MA. p. 1–23.
137. Lakowicz, J., *Principles of Fluorescence Spectroscopy*. Vol. 1. 2006.
138. Grynkiewicz, G., M. Poenie, and R.Y. Tsien, *A new generation of Ca2+ indicators with greatly improved fluorescence properties.* J Biol Chem, 1985. **260**(6): p. 3440–50.

139. Paredes, R.M., et al., *Chemical calcium indicators.* Methods, 2008. **46**(3): p. 143–51.
140. Pessah, I.N., R.A. Stambuk, and J.E. Casida, *Ca2+-activated ryanodine binding: mechanisms of sensitivity and intensity modulation by Mg2+, caffeine, and adenine nucleotides.* Mol Pharmacol, 1987. **31**(3): p. 232–8.
141. Bassani, J.W., R.A. Bassani, and D.M. Bers, *Twitch-dependent SR Ca accumulation and release in rabbit ventricular myocytes.* Am J Physiol, 1993. **265**(2 Pt 1): p. C533–40.
142. Pabel, S., et al., *Effects of Atrial Fibrillation on the Human Ventricle.* Circ Res, 2022. **130**(7): p. 994–1010.
143. Hütter, E., et al., *High-resolution respirometry--a modern tool in aging research.* Exp Gerontol, 2006. **41**(1): p. 103–9.
144. Gnaiger, E., *Mitochondrial pathways and respiratory control.* Innsbruck: OROBOROS MiPNet Publications, 2007.
145. Pesta, D. and E. Gnaiger, *High-resolution respirometry: OXPHOS protocols for human cells and permeabilized fibers from small biopsies of human muscle*, in *Mitochondrial bioenergetics: methods and protocols*. 2011, Springer. p. 25–58.
146. Siska, P.J., et al., *Metabolic imbalance of T cells in COVID-19 is hallmarked by basigin and mitigated by dexamethasone.* J Clin Invest, 2021. **131**(22).
147. Samancioglu, Y., *Fundamental Differences Between Scanning Electron Microscopy (SEM) and Transmission Electron Microscopy (TEM).* Current Studies in Basic Sciences, Engineering and Technology 2023, 2023: p. 159.
148. Williams, D.B. and C.B. Carter, *Transmission electron microscopy.* Systematic Materials Analysis, 1978. **4**: p. 407–432.
149. Ma, H., K.-J. Shieh, and T.X. Qiao, *Study of transmission electron microscopy (TEM) and scanning electron microscopy (SEM).* Nat. Sci, 2006. **4**(3): p. 14–22.
150. Ghadially, F.N., *Ultrastructural pathology of the cell and matrix: a text and atlas of physiological and pathological alterations in the fine structure of cellular and extracellular components*. 2013: Butterworth-Heinemann.
151. Venediktova, N.I., et al., *Formation of lamellar bodies in rat liver mitochondria in hyperthyroidism.* J Bioenerg Biomembr, 2018. **50**(4): p. 289–295.
152. Porter, A.G. and R.U. Jänicke, *Emerging roles of caspase-3 in apoptosis.* Cell Death Differ, 1999. **6**(2): p. 99–104.
153. Gurtu, V., S.R. Kain, and G. Zhang, *Fluorometric and colorimetric detection of caspase activity associated with apoptosis.* Anal Biochem, 1997. **251**(1): p. 98–102.
154. Pohjoismäki, J.L. and S. Goffart, *The role of mitochondria in cardiac development and protection.* Free Radic Biol Med, 2017. **106**: p. 345–354.
155. Borchert, T., et al., *Catecholamine-Dependent β-Adrenergic Signaling in a Pluripotent Stem Cell Model of Takotsubo Cardiomyopathy.* J Am Coll Cardiol, 2017. **70**(8): p. 975–991.
156. Salabei, J.K., A.A. Gibb, and B.G. Hill, *Comprehensive measurement of respiratory activity in permeabilized cells using extracellular flux analysis.* Nat Protoc, 2014. **9**(2): p. 421–38.
157. Cogliati, S., et al., *Mitochondrial cristae shape determines respiratory chain supercomplexes assembly and respiratory efficiency.* Cell, 2013. **155**(1): p. 160–71.

158. Nielsen, J., et al., *Plasticity in mitochondrial cristae density allows metabolic capacity modulation in human skeletal muscle.* J Physiol, 2017. **595**(9): p. 2839–2847.
159. Dorn, G.W. and J.D. Molkentin, *Manipulating cardiac contractility in heart failure: data from mice and men.* Circulation, 2004. **109**(2): p. 150–158.
160. Rywik, T.M., et al., *Heart failure with reduced, mildly reduced, and preserved ejection fraction: outcomes and predictors of prognosis.* Pol Arch Intern Med, 2023. **133**(12).
161. Frantz, S., et al., *The innate immune system in chronic cardiomyopathy: a European Society of Cardiology (ESC) scientific statement from the Working Group on Myocardial Function of the ESC.* Eur J Heart Fail, 2018. **20**(3): p. 445–459.
162. Lei, F., et al., *CSF1R inhibition by a small-molecule inhibitor is not microglia specific; affecting hematopoiesis and the function of macrophages.* Proc Natl Acad Sci U S A, 2020. **117**(38): p. 23336–23338.
163. Kadyrov, F.F., et al., *Hypoxia sensing in resident cardiac macrophages regulates monocyte fate specification following ischemic heart injury.* Nat Cardiovasc Res, 2024. **3**(11): p. 1337–1355.
164. Landstrom, A.P., D. Dobrev, and X.H.T. Wehrens, *Calcium Signaling and Cardiac Arrhythmias.* Circ Res, 2017. **120**(12): p. 1969–1993.
165. Gilbert, G., et al., *Calcium Signaling in Cardiomyocyte Function.* Cold Spring Harb Perspect Biol, 2020. **12**(3).
166. Rao, F., et al., *Role of tumour necrosis factor-a in the regulation of T-type calcium channel current in HL-1 cells.* Clin Exp Pharmacol Physiol, 2016. **43**(7): p. 706–11.
167. Sun, Z., et al., *Cross-talk between macrophages and atrial myocytes in atrial fibrillation.* Basic Res Cardiol, 2016. **111**(6): p. 63.
168. Kang, M., et al., *Cardiac macrophages in maintaining heart homeostasis and regulating ventricular remodeling of heart diseases.* Front Immunol, 2024. **15**: p. 1467089.
169. Hitscherich, P.G., et al., *The effects of macrophages on cardiomyocyte calcium-handling function using in vitro culture models.* Physiol Rep, 2019. **7**(13): p. e14137.
170. Luczak, E.D. and M.E. Anderson, *CaMKII oxidative activation and the pathogenesis of cardiac disease.* J Mol Cell Cardiol, 2014. **73**: p. 112–6.
171. Fischer, T.H., et al., *Ca2+/calmodulin-dependent protein kinase II and protein kinase A differentially regulate sarcoplasmic reticulum Ca2+ leak in human cardiac pathology.* Circulation, 2013. **128**(9): p. 970–81.
172. Currie, S., et al., *Calcium/calmodulin-dependent protein kinase IIdelta associates with the ryanodine receptor complex and regulates channel function in rabbit heart.* Biochem J, 2004. **377**(Pt 2): p. 357–66.
173. Feno, S., et al., *Crosstalk between Calcium and ROS in Pathophysiological Conditions.* Oxid Med Cell Longev, 2019. **2019**: p. 9324018.
174. Bertero, E. and C. Maack, *Calcium Signaling and Reactive Oxygen Species in Mitochondria.* Circ Res, 2018. **122**(10): p. 1460–1478.
175. Wu, D., D. Deng, and B. Tang, *Programmed Cell Death in Heart Failure: Mechanisms, Impacts, and Therapeutic Prospects.* Rev Cardiovasc Med, 2025. **26**(7): p. 38407.
176. Abbate, A., et al., *Acute myocardial infarction and heart failure: role of apoptosis.* Int J Biochem Cell Biol, 2006. **38**(11): p. 1834–40.

177. Weinberger, T., et al., *Resident and recruited macrophages differentially contribute to cardiac healing after myocardial ischemia.* Elife, 2024. **12**.
178. von Harsdorf, R., P.F. Li, and R. Dietz, *Signaling pathways in reactive oxygen species-induced cardiomyocyte apoptosis.* Circulation, 1999. **99**(22): p. 2934–41.
179. Sinenko, S.A., et al., *Physiological Signaling Functions of Reactive Oxygen Species in Stem Cells: From Flies to Man.* Front Cell Dev Biol, 2021. **9**: p. 714370.
180. Ray, P.D., B.W. Huang, and Y. Tsuji, *Reactive oxygen species (ROS) homeostasis and redox regulation in cellular signaling.* Cell Signal, 2012. **24**(5): p. 981–90.
181. Polyak, K., et al., *A model for p53-induced apoptosis.* Nature, 1997. **389**(6648): p. 300–5.
182. Brown, D.I. and K.K. Griendling, *Regulation of signal transduction by reactive oxygen species in the cardiovascular system.* Circ Res, 2015. **116**(3): p. 531–49.
183. De Giusti, V.C., et al., *Mitochondrial reactive oxygen species (ROS) as signaling molecules of intracellular pathways triggered by the cardiac renin-angiotensin II-aldosterone system (RAAS).* Front Physiol, 2013. **4**: p. 126.
184. Rosca, M.G., et al., *Cardiac mitochondria in heart failure: decrease in respirasomes and oxidative phosphorylation.* Cardiovasc Res, 2008. **80**(1): p. 30–9.
185. Bock, F.J. and S.W.G. Tait, *Mitochondria as multifaceted regulators of cell death.* Nat Rev Mol Cell Biol, 2020. **21**(2): p. 85–100.
186. Balaban, R.S., et al., *Role of calcium in metabolic signaling between cardiac sarcoplasmic reticulum and mitochondria in vitro.* Am J Physiol Cell Physiol, 2003. **284**(2): p. C285–93.
187. Glancy, B. and R.S. Balaban, *Role of mitochondrial Ca2+ in the regulation of cellular energetics.* Biochemistry, 2012. **51**(14): p. 2959–73.
188. Dedkova, E.N. and L.A. Blatter, *Calcium signaling in cardiac mitochondria.* J Mol Cell Cardiol, 2013. **58**: p. 125–33.
189. Aksentijevic, D., et al., *Mechano-energetic uncoupling in heart failure.* Nat Rev Cardiol, 2025.
190. Chen, B. and N.G. Frangogiannis, *Macrophages in the Remodeling Failing Heart.* Circ Res, 2016. **119**(7): p. 776–8.
191. Bajpai, G., et al., *Tissue resident CCR2− and CCR2+ cardiac macrophages differentially orchestrate monocyte recruitment and fate specification following myocardial injury.* Circulation research, 2019. **124**(2): p. 263–278.
192. van Amerongen, M.J., et al., *Macrophage depletion impairs wound healing and increases left ventricular remodeling after myocardial injury in mice.* Am J Pathol, 2007. **170**(3): p. 818–29.
193. Harel-Adar, T., et al., *Modulation of cardiac macrophages by phosphatidylserine-presenting liposomes improves infarct repair.* Proc Natl Acad Sci U S A, 2011. **108**(5): p. 1827–32.
194. Ben-Mordechai, T., et al., *Macrophage subpopulations are essential for infarct repair with and without stem cell therapy.* J Am Coll Cardiol, 2013. **62**(20): p. 1890–901.
195. Molinaro, C., et al., *Polarizing Macrophage Functional Phenotype to Foster Cardiac Regeneration.* Int J Mol Sci, 2023. **24**(13).

196. Poltavets, A.S., et al., *Macrophage Modification Strategies for Efficient Cell Therapy.* Cells, 2020. **9**(6).

Acknowledgements

The contractility and histology data presented in this thesis contributed together with different data collected by Lara Schattenfroh to a larger dataset which is currently in preparation for publication.

The images in Figure 3 and Figure 8a were created with Biorender.com. Portions of the text in this thesis were formulated with the assistance of ChatGPT (OpenAI) for language refinement and phrasing purposes only. All scientific content, data analysis, and interpretations are solely the work of the author.

Publications

The following co-authorships have been published so far:

Resistin-like molecule γ attacks cardiomyocyte membranes and promotes ventricular tachycardia; Nina Kumowski, Steffen Pabel, Jana Grune, Noor Momin, Van K. Ninh, **Laura Stengel**, Kyle I. Mentkowski, Yoshiko Iwamoto, Yi Zheng, I-Hsiu Lee, Jessica Matthias, Jan O. Wirth, Fadi E. Pulous, Hana Seung, Alexandre Paccalet, Charlotte G. Muse, Kenneth K. Y. Ting, Paul Delgado, Andrew J. M. Lewis, Vaishali Kaushal, Antonia Kreso, Dennis Brown, Sikander Hayat, Rafael Kramann, Filip K. Swirski, Kamila Naxerova, Daniel C. Propheter, Lora V. Hooper, Michael A. Moskowitz, Kevin R. King, Nadia Rosenthal, Maarten Hulsmans, and Matthias Nahrendorf; *Science*, 2025, doi: 10.1126/science.adp7361.

In Vitro Simulation of Hemodialysis Reveals Hemodialysis-Associated Pro-Arrhythmic Effects in a Human Cardiomyocyte Model; Thomas Körtl, Niklas Hankowitz, **Laura Stengel**, Oliver Pfeuffer, Dominic Riedl, Frank Schweda, Katrin Streckfuß-Bömeke, Samuel Sossalla; *Journal of the American Society of Nephrology,* 2025, doi: 10.1681/ASN.0000000563.

Simulation of cardiac arrhythmias in human induced pluripotent stem cell-derived cardiomyocytes, Thea Bommer, Maria Knierim, Julia Unsöld, Dominic Riedl, **Laura Stengel**, Michael Paulus, Thomas Körtl, Norman Liaw, Lars S Maier, Katrin Streckfuss-Bömeke, Samuel Sossalla, Steffen Pabel; PLOS One, 2024, doi:10.1371/journal.pone.0310463. eCollection 2024.

Therapeutic Spp1 silencing in TREM2+ cardiac macrophages suppresses atrial fibrillation; Noor Momin, Steffen Pabel, Arnab Rudra, Nina Kumowski, I-Hsiu Lee, Kyle Mentkowski, Masahiro Yamazoe, **Laura Stengel**, Charlotte G. Muse, Hana Seung, Alexandre Paccalet, Cristina Gonzalez-Correa, Emily B. Jacobs, Jana Grune, Maximilian J. Schloss, Samuel Sossalla, Gregory Wojtkiewicz, Yoshiko Iwamoto, Patrick McMullen, Richard N. Mitchell, View ORCID ProfilePatrick T. Ellinor, Daniel G. Anderson, Kamila Naxerova, Matthias Nahrendorf; *BioRxiv,* 2024, doi: https://doi.org/10.1101/2024.08.10.607461.

The inotropic and arrhythmogenic effects of acutely increased late INa are associated with elevated ROS but not oxidation of PKARIα; Theresa Gissibl, **Laura Stengel**, Daniel Tarnowski, Lars S. Maier Stefan, Anna-Lena Feder, Can Martin Sag; *Frontiers in Cardiovascular Medicine*, 2024, doi: 10.3389/fcvm.2024.1379930.

Potency and durability of T and B cell immune responses after homologous and heterologous vector delivery of a trimer-stabilized, membrane-displayed HIV-1 clade ConC Env protein; Beatriz Perdiguero, Alexandra Hauser, Carmen Elena Gomez, David Peterhoff, Elefthria Sideris, Carlos Óscar S. Sorzano, Sarah Wilmschen, Marion Schaber, **Laura Stengel**, Benedikt Asbach, Song Ding, Dorothee Von Laer, Yves Levy, Giuseppe Pantaleo, Janine Kimpel, Mariano Esteban, Ralf Wagner; *Frontiers in Immunology*, 2023, doi: 10.3389/fimmu.2023.1270908.

Ibrutinib impairs IGF-1-dependent activation of intracellular Ca handling in isolated mouse ventricular myocytes; Daniel Tarnowski, Anna-Lena Feder, Maximilian Trum, Klaus-Georg Kreitmeier, **Laura Stengel**, Lars S. Maier, Can Martin Sag; *Frontiers in Cardiovascular Medicine*, 2023, doi: 10.3389/fcvm.2023.1190099.

Danksagung

Mein besonderer Dank gilt zunächst Prof. Dr. Lars Maier für seine kontinuierliche Unterstützung und verlässliche Betreuung während der gesamten Promotionszeit. Ich habe mich fachlich wie persönlich stets gut beraten und begleitet gefühlt.

Des Weiteren gilt mein Dank auch vor allem Prof. Dr. Samuel Sossalla, in dessen Arbeitsgruppe ich die Große Freude hatte zu arbeiten. Seine Forschung hat mein Interesse an kardiologischen Fragestellungen ursprünglich geweckt, und seine Unterstützung sowohl vor Beginn als auch während meiner Promotion war außergewöhnlich. Für die zahlreichen Erfahrungen, die ich in den vergangenen Jahren sammeln durfte, insbesondere die Kongressbesuche und Vorträge im In- und Ausland, sowohl für die persönliche Förderung, bin ich sehr dankbar.

Ein weiterer großer Dank gilt Dr. Steffen Pabel, der meine direkte Betreuung übernommen hat. Trotz räumlicher Distanz war die Zusammenarbeit eng, konstruktiv und entscheidend für die Entwicklung dieses Dissertationsprojekts. Seine Begeisterung und sein Engagement haben meine eigene Leidenschaft für Forschung maßgeblich geprägt. Ohne seine Unterstützung, sein fachliches Feedback und die stetige Ermutigung in herausfordernden Phasen wäre meine Promotionszeit nicht dieselbe gewesen.

Auch die Unterstützung außerhalb des Labors war ein wesentlicher Bestandteil dieses Weges. Besonderer Dank geht hierbei vor allem an meine Mama, die mich immer bedingungslos in Allem unterstützt hat und ohne die ich diesen Weg mit Zweitstudium inklusive Promotion nicht hätte antreten können. Ebenso danke ich meinem Partner Daniel, der mir immer in allen Lebenslagen sowohl emotional als auch praktisch unterstützend zur Seite stand, sowie meinen Freunden, die immer ein offenes Ohr hatten und mir den nötigen Rückhalt gegeben haben.

Eidesstattliche Erklärung

Hiermit erkläre ich, Laura Stengel, an Eides statt, dass ich die vorliegende Arbeit selbstständig verfasst und keine anderen als die angegebenen Quellen und Hilfsmittel benutzt habe.

Die aus fremden Quellen direkt oder indirekt übernommenen Gedanken sind als solche gekennzeichnet.

Die Arbeit wurde bisher in gleicher oder ähnlicher Form keiner anderen Prüfungsbehörde weder im In- noch im Ausland vorgelegt.

Regensburg, den 04.12.2025

_____

Laura Stengel